Sapienza Università di Roma

Dottorato di Ricerca in Scienze della Terra, XXXII ciclo

Structure and mechanics of carbonate-hosted fault zones: insights from lab, field, and virtual outcrop models

Ph.D. thesis in Structural Geology

Marco Mercuri

February 2020

Ph.D. Supervisors:

Prof. Cristiano Collettini
Dipartimento di Scienze della Terra,
Sapienza Università di Roma,
P.le Aldo Moro 5, 00185 Roma (Italy)

Prof. Eugenio Carminati
Dipartimento di Scienze della Terra,
Sapienza Università di Roma,
P.le Aldo Moro 5, 00185 Roma (Italy)

Revised by:

Dr. Michele Fondriest
Dipartimento di Geoscienze,
Università degli Studi di Padova,
Padova (Italy)

Dr. Telemaco Tesei
Dipartimento di Geoscienze,
Università degli Studi di Padova,
Padova (Italy)

Preface

The main chapters of this thesis (Chapters 2-4) have to be considered as separate manuscripts. I collected, analysed and interpreted the data and wrote each manuscript under the supervision of Prof. Cristiano Collettini and Prof. Eugenio Carminati (Sapienza Università di Roma, Italy). For the third and fourth chapters of the thesis I was supervised also by Dr. Paolo Mazzanti (Sapienza Università di Roma, Italy) and by Prof. Ken J. W. McCaffrey (Durham University, UK).

Chapter 2 has been published with the following citation:

> **Mercuri, M.**, Scuderi, M. M., Tesei, T., Carminati, E., and Collettini, C. (2018). Strength evolution of simulated carbonate-bearing faults: The role of normal stress and slip velocity. *Journal of Structural Geology*, 109, 1-9.

Chapter 3 has been published with the following citation:

> **Mercuri, M.**, McCaffrey, K. J. W., Smeraglia, L., Mazzanti, P., Collettini, C., and Carminati, E. (2020). Complex geometry and kinematics of subsidiary faults within a carbonate-hosted relay ramp. *Journal of Structural Geology*, 130, 103915.

Chapter 4 is currently under review for *Journal of Stuctural Geology* with the following list of authors and title:

> **Mercuri, M.**, Carminati, E., Tartarello, M. C., Brandano, M., Mazzanti, P., Brunetti, A., McCaffrey, K. J. W., and Collettini, C. Lithological and structural control on fracture distribution within a carbonate-hosted relay ramp

Table of contents

Abstract

Carbonate-hosted fault zones have been extensively studied in the recent past, due to their high socio-economic importance. In fact, they often host seismic sequences characterized by destructive earthquakes with shallow hypocentres (< 10 km) and high magnitude (M_W > 5). Studies dealing with carbonate-hosted faults can therefore help a better assessment of the seismic risk of regions where seismicity occurs within thick carbonate successions. Moreover, since more than the half of the current hydrocarbon reserves are held within carbonate reservoirs, carbonate-hosted faults play a key role in hydrocarbon migration and storage.
Being intimately related to fault mechanics and fluid flow, fault zone structure has been studied at different scales and using different techniques. Segmentation and/or bending of faults at sub-regional scales (1-10 km) can have important consequences on seismic rupture propagation and arrest. The outcrop-scale (10 m – 1 km) structure has fundamental implications for the fluid flow and fault mechanics. On one hand, the fault core vs. damage zone arrangement, and particularly fracture distribution within the latter, define the fault permeability structure. On the other hand, the deformation style (i.e., localized or/and distributed) can offer insights on the frictional properties of the fault zone (i.e., strong or/and weak fault). Microstructures collected on the principal slip zones (mm-thick zones that accommodates most of the displacement in faults) can shed light on the deformation mechanisms accommodating slip on faults. Finally, natural microstructures in principal slip zones can be associated with a specific mechanical behaviour and physical-chemical conditions (e.g., normal stress, slip velocity, saturating fluid, temperature) leveraging on their comparison with structures observed in principal slip zones retrieved from friction experiments.

Although many studies focused on carbonate-hosted faults structure during the last two decades, there is still a lot of work to do in order to accomplish the complete characterization of their structure and mechanics. One of the most challenging goal is to understand factors controlling fault zone structure.

In this thesis I investigate the factors controlling the geometry, kinematics, mechanics, and distribution of various components of fault zones: principal slip zones (chapter 2), subsidiary faults (chapter 3), and fractures (chapter 4).

In chapter 2, "Strength evolution of simulated carbonate-bearing faults: The role of normal stress and slip velocity", I present the results obtained from a series of rock mechanics experiments, conducted to evaluate the friction of simulated carbonate-bearing faults in water-saturated conditions and for a wide range of normal stresses (from 5 to 120 MPa) and slip velocities (from 0.3 to 100 μm/s). Since the coexistence of structures related to pressure dependent (i.e., cataclastic) and pressure independent deformation processes (i.e., pressure-solution and granular plasticity) is common within natural carbonate-hosted faults exhumed from shallow seismogenic depths (< 6 km), I simulated the slip nucleation on simulated carbonate-bearing faults in order to constrain the boundary conditions (normal stress and slip velocity) that are necessary to activate pressure independent processes. The comparison between the mechanical results and the obtained microstructures allowed me to evaluate the effect of the activation of pressure independent deformation processes on friction. At low normal stresses ($\sigma_N \leq 20$ MPa) the deformation is accommodated by localized cataclastic grain size reduction, and friction is high (μ = 0.64). Pressure independent processes, especially pressure-solution, increase their contribution in accommodating slip with increasing normal stress and decreasing slip velocity. The activation of such processes produces an anastomosed foliation, accompanied by cementation, grain indentations, grain folding, and the formation of striated surfaces coated with nanograins. Friction decreases with an increasing contribution of pressure independent processes, reaching very low values (μ = 0.47) at the highest normal stress (σ_N = 120 MPa) and lowest slip velocity (v = 0.3 μm/s) tested conditions. The results suggest that the activation of fluid assisted diffusion mass transfer (i.e., pressure-solution) and grain plasticity can significantly reduce the frictional strength of carbonate-bearing faults, facilitating the onset of fault slip.

In chapters 3, "Complex geometry and kinematics of subsidiary faults within a carbonate-hosted relay ramp", and 4, "Lithological and structural control on fracture distribution within a carbonate-hosted relay ramp", I investigate an exceptional exposure of a portion of a carbonate-hosted relay ramp damage zone, pertaining to the Tre Monti normal fault in the Central Apennines (Italy). The studied outcrop is located immediately at the footwall of the front fault segment. The relay ramps are zones of slip transfer between overlapping normal faults and represent a very challenging and interesting case-study. In fact, the mechanical interaction between the two faults promotes an increase in damage, representing a potential preferential pathway for fluids. Moreover, relay ramps can represent zones of stress field rotation.

For both the chapters I leveraged on the integration of traditional field techniques and interpretation of virtual outcrops. Three-dimensional digital reconstructions of outcrops (VOM: Virtual Outcrop Models, or DOM: Digital Outcrop Models) can be obtained from terrestrial laser scanner and/or photogrammetric surveys. Virtual outcrops are increasingly used in structural geology because they enhance our ability to collect data, allowing the exploration of inaccessible portions of the outcrop and the collection high-precision georeferenced dataset.

In chapter 3, the geometry and the kinematics of the subsidiary faults have been investigated. Minor faults show complex geometry and kinematics, having multiple attitudes each one characterized by highly variable kinematics. The fault slip analysis highlights that minor faults geometry and kinematics are not compatible neither with the overall dip-slip kinematics of the Tre Monti fault nor with the active regional extension occurring in the central Apennines. Conversely, a local stress field, retrieved from the kinematic inversion of the locally occurring right lateral slickenlines on the front fault segment, is able to explain most of the minor faults geometry and kinematics. Such a stress field is likely caused by the mechanical interaction between the fault segments bordering the relay ramp. The results obtained in this chapter highlight that the local stress field plays a key-role in the complex minor faults geometry and kinematics. Further complexity can be provided by the local scale temporal interaction with other stress.

Finally, in chapter 4, the fracture distribution within the relay-ramp damage zone is imaged through the integration of classical field techniques (i.e., scanlines), fracture counting on oriented rock samples, and interpretation of a virtual outcrop derived from an aero-photogrammetric survey. Fracture density increases with distance from the front segment of the relay ramp. The results also highlight a control of carbonate facies on fracturing, with supratidal and intertidal facies showing higher fracture density than subtidal limestones. This apparent anomalous pattern of fracture density, that increases moving away from a main fault segment, is related to two main factors. (1) Since moving away from the front segment (i.e., toward the centre of the relay ramp), also the number of subsidiary faults increases, the damage is likely related to the activity of subsidiary faults accompanying the development of the relay ramp. (2) The supratidal/intertidal facies content increases toward the centre of the relay ramp leading to an increase in fracture density.

This thesis furtherly emphasizes the importance of friction experiments and virtual outcrops in structural geology studies dealing with fault zone structure and mechanics. Friction experiments allowed to establish the effect of pressure insensitive deformation processes on the carbonate-faults mechanics through a direct comparison between microstructures and the mechanical behaviour. The employment of virtual outcrops enabled a very detailed mapping of subsidiary faults and fracture density within a carbonate-hosted damage zone, allowing the investigation of the factors that controls subsidiary faults geometry and kinematics, and fracture distribution.

Riassunto

Le faglie in carbonati sono state ampiamente studiate nel recente passato poiché estremamente interessanti dal punto di vista socioeconomico. Infatti, molte sequenze sismiche vengono comunemente localizzate all'interno di successioni carbonatiche. Tali sequenze sismiche sono spesso distruttive perché caratterizzate da *mainshock* con magnitudo elevate (M_w >5) e ipocentri poco profondi (< 10 km). Pertanto, gli studi sulle faglie in carbonati possono essere molto utili per meglio definire la stima del rischio sismico delle zone in cui le sequenze sismiche avvengono all'interno delle successioni carbonatiche, come la regione appenninica. Inoltre, poiché attualmente più della metà delle riserve di idrocarburi è situata all'interno di *reservoir* carbonatici, le faglie in carbonati possono giocare un ruolo molto importante nella migrazione e nell'accumulo degli idrocarburi.

Poiché la struttura in una zona di faglia è fortemente connessa alla sua meccanica e alla circolazione dei fluidi, questa è stata studiata a diverse scale di osservazione e utilizzando varie tecniche. Le faglie si presentano comunemente segmentate e/o ondulate a scala chilometrica. Questo può avere forti ripercussioni sulla propagazione e l'arresto di rotture sismiche. La struttura a scala dell'affioramento (10 m – 1 km) è strettamente connessa alla circolazione dei fluidi e alla meccanica delle faglie. Infatti, l'organizzazione in *fault core* e *damage zone* (zona di danneggiamento) e, in particolare, la distribuzione delle fratture all'interno di quest'ultima determina la struttura di permeabilità di una zona di faglia. Inoltre, lo stile di deformazione (ad esempio localizzato o distribuito) può fornire informazioni sulle proprietà di attrito della zona di faglia (faglia *strong* o *weak*). Le microstrutture raccolte dalle zone principali di scivolamento (zone di spessore millimetrico che accomodano la maggior parte del rigetto nelle faglie) possono mettere in luce i meccanismi deformativi che accomodano lo scivolamento. Infine, è possibile associare le microstrutture delle zone principali di scivolamento di faglie naturali a specifici comportamenti meccanici e condizioni fisico-chimiche al contorno (es. sforzo normale, velocità di scivolamento, fluidi, temperatura) facendo leva sul loro confronto con le microstrutture ricavate da esperimenti di attrito su faglie sperimentali.

Nonostante negli ultimi due decenni siano stati effettuati numerosi studi sulle faglie in carbonati, si è ancora ben lontani da una completa comprensione della loro struttura e meccanica. Uno degli obiettivi più stimolanti è quello di comprendere le variabili che controllano la struttura di queste faglie. In questa tesi sono stati studiati i fattori che controllano la geometria, la cinematica, la meccanica con particolare attenzione ai seguenti elementi delle zone di faglia: zone principali di scivolamento (capitolo 2), faglie secondarie (capitolo 3) e fratture (capitolo 4).

Nel capitolo 2, "*Strength evolution of simulated carbonate-bearing faults: The role of normal stress and slip velocity*", vengono presentati i risultati ottenuti da una serie di esperimenti di meccanica delle rocce, effettuati per valutare l'attrito di faglie sperimentali in carbonati sature in acqua a varie condizioni di sforzo normale (da 5 a 120 MPa) e velocità di scivolamento (da 0.3 a 100 μm/s). Dal momento che sulle faglie in carbonati naturali esumate da basse profondità sismogenetiche (< 6 km) è comune osservare la coesistenza di strutture legate a meccanismi deformativi *pressure sensitive* (cataclastici) e *pressure insensitive* (es. pressione-soluzione e plasticità granulare), è stata simulata la nucleazione dello scivolamento su faglie sperimentali in carbonati in modo tale da vincolare le condizioni al contorno (sforzo normale e velocità di scivolamento) necessarie per l'attivazione dei meccanismi deformativi *pressure insensitive*. Il confronto tra il dato meccanico e le microstrutture ottenute dagli esperimenti ha permesso di valutare l'effetto dei meccanismi deformativi *pressure insensitive* sull'attrito. A bassi sforzi normali ($\sigma_N \leq 20$ MPa) la deformazione è cataclastica e localizzata, con riduzione della taglia granulometrica, e l'attrito è alto (μ = 0.64). I processi deformativi *pressure insensitive*, in particolar modo la pressione-soluzione, aumentano il loro contributo nell'accomodare lo scivolamento all'aumentare dello sforzo normale e al diminuire della velocità di scivolamento. L'attivazione di tali processi provoca lo sviluppo di una foliazione anastomizzata, accompagnata da cementazione, indentatura e piegamento dei granuli, e dallo sviluppo di superfici striate pavimentate da nano-granuli. L'attrito diminuisce all'aumentare del contributo dei processi *pressure insensitive*, e raggiunge valori molto bassi (μ = 0.47) alle condizioni di sforzo normale più alte (σ_N = 120 MPa) e di velocità di scivolamento più basse (v = 0.3 μm/s) testate negli esperimenti. I risultati ottenuti suggeriscono che l'attivazione di processi di pressione-soluzione e di plasticità granulare possono ridurre in maniera significativa la resistenza delle faglie in carbonati, facilitando l'inizio dello scivolamento.

Nei capitoli 3, "*Complex geometry and kinematics of subsidiary faults within a carbonate-hosted relay ramp*", e 4, "*Lithological and structural control on fracture distribution within a carbonate-hosted relay ramp*", viene studiato un affioramento eccezionale della zona di danneggiamento di una faglia in carbonati: la faglia diretta di Tre Monti nell'Appennino centrale. Tale affioramento si

colloca immediatamente al letto del segmento frontale di una *relay ramp*. Le *relay ramp* sono zone in cui viene trasferito il rigetto tra due faglie normali che si sovrappongono lungo la loro direzione, e rappresentano un caso di studio molto stimolante. Infatti, l'interazione meccanica tra i due segmenti di faglia che delimitano la *relay ramp* causa un aumento del danneggiamento favorendo potenzialmente la circolazione dei fluidi. Inoltre, le *relay ramp* rappresentano zone in cui si possono manifestare ingenti rotazioni del campo di sforzi.
Per entrambi i capitoli si sono integrate tecniche classiche di terreno con l'interpretazione di affioramenti virtuali. La ricostruzione digitale tridimensionale degli affioramenti (*VOM: Virtual Outcrop Model*, o *DOM: Digital Outcrop Model*) può essere effettuata tramite *laser scanner* terrestre e/o tramite fotogrammetria. Gli affioramenti virtuali vengono sempre più utilizzati in geologia strutturale perché migliorano l'abilità nel raccogliere dati, permettendoci di esplorare porzioni altrimenti inaccessibili degli affioramenti e di raccogliere dati geo-referenziati ad alta precisione.

Nel capitolo 3 viene studiata la geometria e cinematica delle faglie minori. Queste presentano una geometria e una cinematica complesse, poiché caratterizzate da svariate orientazioni, ciascuna delle quali associata a molte cinematiche. L'analisi cinematico-dinamica condotta sulle faglie minori evidenzia che la loro geometria e cinematica non è compatibile né con la cinematica estensionale della faglia di Tre Monti, né con il campo di sforzi estensionale attualmente attivo nell'Appennino centrale. La maggior parte delle geometrie e delle cinematiche delle faglie minori è invece in accordo con un campo di sforzi locale, ricavato dall'inversione cinematica delle strie trascorrenti destre che affiorano localmente sul segmento di faglia frontale della *relay ramp*. Tale campo di sforzi è, con ogni probabilità, legato all'interazione meccanica tra i segmenti di faglia che delimitano la *relay ramp*. I risultati ottenuti evidenziano che il campo di sforzi locale gioca un ruolo chiave nella complessa geometria e cinematica delle faglie minori. Ulteriore complessità può essere apportata dall'interazione temporale a scala locale con altri campi di sforzo.

Infine, nel capitolo 4 viene studiata la distribuzione della fratturazione all'interno della zona di danneggiamento attraverso l'integrazione di tecniche classiche di terreno (*scanline*), il conteggio di fratture su campioni di roccia orientati e l'interpretazione di un affioramento virtuale derivato da fotogrammetria via drone. I risultati mostrano che la densità di fratturazione aumenta all'allontanarsi dal segmento frontale della *relay ramp*. Viene inoltre evidenziato un controllo della *facies* carbonatica sulla fratturazione, con le facies sopratidale e intertidale che mostrano una densità di fratturazione maggiore rispetto alla facies subtidale. La distribuzione apparentemente anomala della densità di fratturazione, che aumenta all'allontanarsi da un segmento principale di faglia, è dovuta a due fattori. (1) Dal momento che all'allontanarsi dalla faglia principale (ovvero muovendosi verso il centro della *relay ramp*) aumenta anche il numero di faglie minori, il danneggiamento è plausibilmente dovuto all'attività delle faglie minori che accompagnano lo sviluppo della *relay ramp*. (2) Il contenuto in facies sopratidale ed intertidale aumenta con la distanza dalla faglia principale provocando un aumento della densità di fratturazione.

Questa tesi enfatizza ulteriormente l'importanza degli esperimenti sull'attrito e degli affioramenti virtuali negli studi di geologia strutturale riguardanti la struttura e la meccanica di zone di faglia. Gli esperimenti sull'attrito hanno permesso di stabilire l'effetto dei processi deformativi *pressure insensitive* sulla meccanica delle faglie in carbonati attraverso il confronto diretto tra il comportamento meccanico e le microstrutture. L'utilizzo degli affioramenti virtuali ha consentito di mappare dettagliatamente le faglie minori e la densità di fratturazione all'interno di una zona di danneggiamento in carbonati, permettendo di investigare i fattori che controllano la geometria e la cinematica delle faglie secondarie e la distribuzione della fratturazione.

1. Introduction

During the last two decades, many studies focused on carbonate-hosted faults. Their structural and mechanical characterization represents a very important target for two main socio-economic reasons. Firstly, many seismic sequences with moderate to large earthquakes occur worldwide within thick (4-10 km) carbonate successions. Some of the most investigated examples are represented by the Aigion event in 1995 in Greece (M_S = 6.2; Bernard et al., 1997), the Wenchuan earthquake in 2008 in China (M_W = 7.9; Burchfiel et al., 2008), and many seismic sequences that occurred in Italy: Umbria-Marche in 1997-98 ($M_W \leq 6$; Miller et al., 2004; Mirabella et al., 2008), L'Aquila in 2009 ($M_W \leq 6.1$; Valoroso et al., 2014), Emilia in 2012 ($M_W \leq 5.7$; Ventura & Di Giovambattista, 2012; Govoni et al., 2014), and the 2016-17 Central Italy seismic sequence ($M_W \leq 6.5$; Porreca et al., 2018). Since these events are often characterized by a shallow depth (< 10 km) of the hypocenters and by a moderate to high magnitude ($M_W > 5$), they often cause fatalities and heavy damages to buildings and infrastructures. Studies dealing with the structure and mechanics of carbonate-hosted faults can therefore offer insights on the earthquakes mechanics and help a better assessment of the seismic risk of these regions. Secondly, more than the half of the current hydrocarbon reserves are held within carbonates, where faults can play a fundamental role in the fluid circulation (Caine et al., 1996; Bense et al., 2013), and can potentially host induced earthquakes. Therefore, the characterization of carbonate-hosted fault structure is fundamental for the assessment of hydrocarbon migration and storage within reservoirs.

Fault structure, fault mechanics and fluid flow.

Being intimately related, the characterization of fault zone structure leads to a better understanding of fault mechanics and fluid circulation within fault zones (Ben-Zion & Sammis, 2003; Biegel & Sammis, 2004; Wibberley et al., 2008; Faulkner et al., 2010). The relationship between fault structure, fault mechanics, and fluid flow holds at various scales, from sub-regional (tens of km) down to nanoscale. The sub-regional scale is commonly investigated through field mapping (Faulkner et al., 2003; Bonson et al., 2007; Smith et al., 2013; Collettini et al., 2014; Demurtas et al., 2016; Smeraglia et al., 2016a, 2016b), seismic reflection profiles (Collettini and Barchi, 2002; Hsiao et al., 2004; Long and Imber, 2012), and high-resolution aftershocks relocation (Rubin et al., 1999; Waldhauser & Ellsworth, 2000; Schaff et al., 2002; Valoroso et al., 2014). All these studies highlight that faults are commonly segmented and/or show corrugations both in map and in section view (e.g., Jackson & White, 1989; Walsh et al., 2003; Sagy & Brodsky, 2009). Both corrugations and segmentation of faults can limit the extent of rupture propagation during earthquakes, (e.g., King & Nabelek, 1985; Barka & Kadinsky-Cade, 1988; Wesnousky, 2006), with evident consequences for earthquake magnitude. Moreover, zones where fault segments interact (e.g., the relay ramps within normal fault systems) may represent important pathways for fluids (Fossen & Rotevatn, 2016 and references therein) with direct consequences on hydrogeology and hydrocarbon exploration.

The outcrop-scale (10 m – 1 km) fault zone structure can be investigated through observations conducted in the field. At this scale two main elements can be identified in fault zones: a fault core (or multiple fault cores; e.g., Faulkner et al., 2003) and a damage zone (e.g., Chester & Logan, 1986; Chester et al., 1993; Peacock et al., 2017). In low porosity lithologies, such as most of the carbonates, a single fine-grained fault core is surrounded by a fracture-dominated damage zone (e.g., Agosta & Aydin, 2006; Fondriest et al., 2012; Smeraglia et al., 2016a, 2016b). Such a fault zone structure strongly influences fluid circulation (Caine et al., 1996; Bense et al., 2013). In fact, the fault core, accommodating most of the displacement, is characterized by strong comminution of rocks by frictional wear and it is therefore relatively impermeable to fluid flow (Caine et al., 1996). Fractures in the damage zone hence constitute the main pathway for fluid circulation within faults hosted in low-porosity rocks (Caine et al., 1996; Aydin, 2000; Bense et al., 2013;). Consequently, the orientation, distribution, aperture, and connectivity of fractures in the damage zone and the relative abundance of fault core(s) and damage zone define fault zone permeability (Caine et al., 1996; Bense et al., 2013). The permeability within fault zones may, in turn, promotes or prevents fluid overpressures, and hence influences stress field and slip on faults (Sibson, 1994). Furthermore, fault mechanics can be affected by the fracture distribution within the fault zone. In fact, fracturing modifies the elastic properties of the host rock, leading to stress field rotation and to the reactivation of unfavourably oriented faults (Faulkner et al., 2006). The outcrop scale fault zone structure can also offer insights on its frictional properties. Although the concept of strong vs. weak faults is getting outdated in favor of heterogeneous faults composed of weak and strong patches (Collettini et al., 2019), it is possible to derive considerations about frictional properties of the faults from their structure. Strong faults, having sliding friction values following the Byerlee's rule ($0.6<\mu<0.85$; Byerlee, 1978), are commonly characterized by narrow zone of extremely high strain localization, with cataclastic deformation increasing toward a single fault core, where most of the slip is accommodated by mm-thick principal slip zones (Sibson, 2003; Smith et al., 2011; Siman-Tov et al., 2013). Conversely, weak faults are characterized by low friction values ($\mu<0.3$). Generally, a weak fault zone structure shows distributed deformation along interconnected and anastomosing shear zones rich in phyllosilicates (e.g., Faulkner et al., 2003; Bullock et al., 2014; Tesei et al., 2018).

Finally, microstructures in samples collected from principal slip zones offer important insights on fault mechanics and, in particular, on deformation mechanisms accommodating slip on faults. Principal slip zones are mm-thick, located within the fault core, and accommodate most of the slip in mature faults (Sibson, 2003; Smith et al., 2011; Siman-Tov et al., 2013). Microstructures observed on natural faults can be compared with those retrieved from friction experiments. In this way it is possible to link natural microstructures with the mechanical behaviour and physical-chemical conditions reproduced in experiments (e.g., normal stress, slip velocity, temperature, and fluid condition). For example, in carbonate-rocks the recognition of microstructures, such as calcite crystals exhibiting localized disaggregation together with a high concentration of vesicles, that are typically observed in high-velocity (~ 1 m/s) shear experiments, allow to infer past seismic slip in natural principal slip zones (e.g., Smith et al., 2011; Collettini et al., 2014; Smeraglia et al., 2017).

Virtual outcrops: an emerging tool in structural geology

Three-dimensional digital reconstructions of outcrops have been increasingly employed in geology during the last 15 years. They are known as virtual outcrop models (VOMs; e.g., McCaffrey et al., 2005a, 2005b), or as digital outcrop models (DOMs; e.g., Bellian et al., 2005). Virtual outcrops can be obtained using terrestrial laser scanner and/or structure-from-motion photogrammetry.

The terrestrial laser scanner (TLS) is a device that produces a series of laser beams that, once reflected by the outcrop surface, come back and are registered by the same device (Buckley et al., 2008; Telling et al., 2017). The TLS calculates the angular position and the distance between the sensor and the reflecting point knowing the velocity of the light. The integration of the laser scanner device with a high-resolution calibrated camera provides the actual colours of the scene. In this way a point cloud, that is generally composed of more than 1 million points, is generated in a relative coordinate system. The point cloud can be georeferenced by knowing the coordinates of at least three highly reflective objects in the scene (ground control points, GCPs).

The structure-from-motion photogrammetry consists in an algorithm that exploits a series of overlapping (usually > 70% overlap) photos to build a 3D model of the scene (Westoby et al., 2012; Bemis et al., 2014). Previous work showed that structure-from-motion photogrammetry constitutes a higher efficiency vs. costs ratio technique than terrestrial laser scanner (Wilkinson et al., 2016; Cawood et al., 2017).

The photos can be taken by a person, or an unmanned aerial vehicle (commonly a quadcopter drone). In the latter case the technique is called UAV structure-from-motion. Analogously to the TLS, the model can be sized and georeferenced exploiting the knowledge of the coordinates of some ground control points. The ground control points should be easily recognizable in the photos. Once the photos have been collected, the structure from motion algorithm can be applied using commercial software's (e.g., Agisoft Metashape®, 3DFlow Zephyr®). Independently of the software, the structure-from-motion algorithm is characterized by the following steps. First, photos are aligned through a semi-automatic identification of common points in adjacent pictures in order to create a point cloud (sparse point cloud). Photos are hence processed to obtain a dense fully coloured point cloud. Such a point cloud is subsequently used to build a mesh and, finally, the textured mesh representing the virtual outcrop. Further details on the structure from motion algorithm can be found in Westoby et al. (2012) and Bemis et al. (2014).

Once the virtual outcrop has been created, structural data can be collected from it using specific software or plugins such as OpenPlot (Tavani et al., 2011), VRGS (Hodgetts, 2013), Compass (Thiele et al., 2017), and LIME (Buckley et al., 2018).

Virtual outcrops have been applied in many structural geology studies (Bemis et al., 2014; Telling et al., 2017 for a review) dealing with folds (e.g., Vollgger and Cruden, 2016; Cawood et al., 2017), faults (e.g., Sagy et al., 2007; Candela et al., 2009; Bistacchi et al., 2011), and fractures (Vasuki et al., 2014; Pless et al., 2015; Seers and Hodgetts, 2016; Corradetti et al., 2018). The most common application of virtual outcrops on studies dealing with faults is the analysis of the main slip surface topography and roughness (Sagy et al., 2007; Candela et al., 2009; Brodsky et al., 2011; Corradetti et al., 2017). Another interesting application is the mapping and the collection of attitudes of planar and linear elements, such as bedding, faults and slip directions on fault surfaces (e.g., Rotevatn et al., 2009; Gold et al., 2012; Bistacchi et al., 2015). Other studies employed virtual outcrops to map recent displacements on fault scarps (e.g., Wilkinson et al., 2015), to analyse fracture distribution within the damage zones (e.g., Pless et al., 2015), and to calculate coseismic and postseismic deformation on superficial active fault scarps (e.g., Wedmore et al., 2019).

Virtual outcrops enhance our ability to collect data, allowing the exploration of inaccessible portions of the outcrop and the collection high-precision georeferenced dataset, and are therefore an increasingly used technique for structural geology studies.

This work

Although carbonate-hosted fault zones have been extensively studied in the recent past, there is still a lot of work to do in order to accomplish the complete understanding of their structure and mechanics. One of the most challenging goal is to understand factors controlling fault zone structure. This thesis aims to contribute to this topic by answering to the following questions:

1) What is the role of normal stress and slip velocity on the structure and mechanics of principal slip zones?

2) What controls the geometry and the kinematics of subsidiary faults along segmented faults, and in particular within relay ramps?

3) What controls fracture distribution within a carbonate-hosted relay ramp?

Each question deals with a different component of fault zones (principal slip zones, subsidiary faults, and fractures), and will be therefore separately answered in the following chapters.

In chapter 2, "*Strength evolution of simulated carbonate-bearing faults: The role of normal stress and slip velocity*", the structure and the mechanics of principal slip zones of simulated carbonate-bearing faults is investigated. In detail, I present the results obtained from a series of rock mechanics experiments, conducted to evaluate the friction of simulated carbonate-bearing faults in water-saturated conditions and for a wide range of normal stresses (from 5 to 120 MPa) and slip velocities (from 0.3 to 100 μm/s).

In chapters 3, "*Complex geometry and kinematics of subsidiary faults within a carbonate-hosted relay ramp damage zone*", and 4, "*Lithological and structural control on fracture distribution within a carbonate-hosted relay ramp*", I deal with the two principal components of the fault damage zones: subsidiary faults (chapter 3), and fractures (chapter 4). Both chapters share the same case-study: an exceptional exposure of a carbonate-hosted relay ramp damage zone, pertaining to the Tre Monti normal fault in the Central Apennines.

In chapter 3, I integrate classical field mapping and analysis of a virtual outcrop to show the complex geometry and the kinematics of subsidiary faults in the damage zone. The fault slip analysis suggests that a key-role for such a complexity is played by the development of a local stress field due to the interaction between the front and rear fault segments of the relay ramp.

Finally, in chapter 4, the fracture distribution within the relay-ramp damage zone is imaged through the integration of a classical field technique (i.e., scanlines; Priest & Hudson, 1981), fracture counting on oriented samples, and the interpretation of a virtual outcrop. I show that the relay ramp environment and carbonate facies are able to control the fracture distribution in the damage zone.

References

Agosta, F., & **Aydin, A.** (2006). Architecture and deformation mechanism of a basin-bounding normal fault in Mesozoic platform carbonates, central Italy. *Journal of Structural Geology*, *28*(8), 1445–1467.

Aydin, A. (2000). Fractures, faults, and hydrocarbon entrapment, migration and flow. *Marine and Petroleum Geology*, *17*(7), 797–814.

Barka, A., & **Kadinsky-Cade, K.** (1988). Strike-slip fault geometry in Turkey and its influence on earthquake activity. *Tectonics*, *7*(3), 663–684.

Bastesen, E., & **Rotevatn, A.** (2012). Evolution and structural style of relay zones in layered limestone–shale sequences: insights from the Hammam Faraun Fault Block, Suez rift, Egypt. *Journal of the Geological Society*, *169*(4), 477–488.

Bellian, J. A., **Kerans, C.**, & **Jennette, D. C.** (2005). Digital Outcrop Models: Applications of Terrestrial Scanning Lidar Technology in Stratigraphic Modeling. *Journal of Sedimentary Research*, *75*(2), 166–176.

Bemis, S. P., **Micklethwaite, S.**, **Turner, D.**, **James, M. R.**, **Akciz, S.**, **Thiele, S. T.**, & **Bangash, H.** (2014). Ground-based and UAV-Based photogrammetry: A multi-scale, high-resolution mapping tool for structural geology and paleoseismology. *Journal of Structural Geology*, *69*, 163–178.

Bense, V. F., **Gleeson, T.**, **Loveless, S. E.**, **Bour, O.**, & **Scibek, J.** (2013). Fault zone hydrogeology. *Earth-Science Reviews*, *127*, 171–192.

Ben-Zion, Y., & **Sammis, C.** (2003). Characterization of Fault Zones. *Pure and applied Geophysics, 160*, 677–715.

Bernard, P., **Briole, P.**, **Meyer, B.**, **Lyon-Caen, H.**, **Gomez, J.**, **Tiberi, C.**, et al. (1997). The Ms=6.2, June 15, 1995 Aigion earthquake (Greece): evidence for low angle normal faulting in the Corinth rift. *Journal of Seismology, 1*, 131–150.

Biegel, R. L., & **Sammis, C. G.** (2004). Relating Fault Mechanics to Fault Zone Structure. *Advances in Geophysics*, *47*, 65–111.

Bistacchi, A., Balsamo, F., Storti, F., Mozafari, M., Swennen, R., Solum, J., ... & **Taberner, C.** (2015). Photogrammetric digital outcrop reconstruction, visualization with textured surfaces, and three-dimensional structural analysis and modeling: Innovative methodologies applied to fault-related dolomitization (Vajont Limestone, Southern Alps, Italy). *Geosphere*, *11*(6), 2031-2048.

Bistacchi, A., Griffith, A. W., Smith, S. A., Di Toro, G., Jones, R., & **Nielsen, S.** (2011). Fault Roughness at Seismogenic Depths from LIDAR and Photogrammetric Analysis. *Pure and Applied Geophysics*, *168*(12), 2345–2363.

Bonson, C. G., Childs, C., Walsh, J. J., Schöpfer, M. P. J., & **Carboni, V.** (2007). Geometric and kinematic controls on the internal structure of a large normal fault in massive limestones: The Maghlaq Fault, Malta. *Journal of Structural Geology*, *29*(2), 336–354.

Brock, W. G., & **Engelder, T.** (1977). Deformation associated with the movement of the Muddy Mountain overthrust in the Buffington window, southeastern Nevada. *GSA Bulletin*, *88*(11), 1667–1677.

Brodsky, E., J. Gilchrist, A. Sagy, & **Collettini, C.** (2011), Faults smooth gradually as a function of slip. *Earth Planet Sc Lett*, *302(1-2)*, 185–193.

Buckley, S. J., Howell, J. A., Enge, H. D., & **Kurz, T. H.** (2008). Terrestrial laser scanning in geology: data acquisition, processing and accuracy considerations. *Journal of the Geological Society*, *165*(3), 625-638.

Buckley, S. J., Ringdal, K., Naumann, N., Dolva, B., Kurz, T. H., Howell, J. A., & **Dewez, T.** (2018). LIME: Software for 3-D visualization, interpretation, and communication of virtual geoscience models. *Geosphere,* 15(1), 222-235.

Bullock, R. J., De Paola, N., Holdsworth, R. E., & **Trabucho-Alexandre, J.** (2014). Lithological controls on the deformation mechanisms operating within carbonate-hosted faults during the seismic cycle, *Journal of Structural Geology, 58*, 22–42.

Burchfiel, B., Royden, L., van der Hilst, R., Hager, B., Chen, Z., King, R., *et al.* (2008). A geological and geophysical context for the Wenchuan earthquake of 12 May 2008, Sichuan, People's Republic of China. *GSA Today, 18*(7), 4-11.

Byerlee, J. (1978). Friction of rocks. *Pure and Applied Geophysics*, *116*(4–5), 615–626.

Caine, J. S., Evans, J. P., & **Forster, C. B.** (1996). Fault zone architecture and permeability structure. *Geology*, *24*(11), 1025–1028.

Candela, T., Renard, F., Bouchon, M., Brouste, A., Marsan, D., Schmittbuhl, J., & **Voisin, C.** (2009). Characterization of Fault Roughness at Various Scales: Implications of Three-Dimensional High Resolution Topography Measurements. *Pure and Applied Geophysics*, 1817–1851.

Cawood, A. J., Bond, C. E., Howell, J. A., Butler, R. W., & **Totake, Y.** (2017). LiDAR, UAV or compass-clinometer? Accuracy, coverage and the effects on structural models. *Journal of Structural Geology*, *98*, 67–82.

Chester, F., & **Logan, J.** (1986). Implications for mechanical properties of brittle faults from observations of the Punchbowl fault zone, California. *Pure and Applied Geophysics*, *124*(1–2), 79–106.

Chester, F. M., & **Chester, J. S.** (1998). Ultracataclasite structure and friction processes of the Punchbowl fault, San Andreas system, California, *Tectonophysics, 295*(1–2), 1–23.

Chester, F. M., Evans, J. P., & **Biegel, R. L.** (1993). Internal structure and weakening mechanisms of the San Andreas fault. *Journal of Geophysical Research*, *98*(B1), 771–786.

Collettini, C, Carpenter, B. M., Viti, C., Cruciani, F., Mollo, S., Tesei, T., et al. (2014). Fault structure and slip localization in carbonate-bearing normal faults: An example from the Northern Apennines of Italy. *Journal of Structural Geology*, *67*, 154–166.

Collettini, C, Tesei, T., Scuderi, M. M., Carpenter, B. M., & **Viti, C.** (2019). Beyond Byerlee friction, weak faults and implications for slip behavior. *Earth and Planetary Science Letters*, *519*, 245–263.

Collettini, C, & **Barchi, M. R.** (2002). A low-angle normal fault in the Umbria region (Central Italy): a mechanical model for the related microseismicity. *Tectonophysics*, *359*(1–2), 97–115.

Corradetti, A., McCaffrey, K., De Paola, N., & Tavani, S. (2017). Evaluating roughness scaling properties of natural active fault surfaces by means of multi-view photogrammetry. *Tectonophysics, 717*, 599–606.

Corradetti, A., Tavani, S., Parente, M., Iannace, A., Vinci, F., Pirmez, C., et al. (2018). Distribution and arrest of vertical through-going joints in a seismic-scale carbonate platform exposure (Sorrento peninsula, Italy): insights from integrating field survey and digital outcrop model. *Journal of Structural Geology, 108, 121-136*.

Demurtas, M., Fondriest, M., Balsamo, F., Clemenzi, L., Storti, F., Bistacchi, A., & Di Toro, G. (2016). Structure of a normal seismogenic fault zone in carbonates: The Vado di Corno Fault, Campo Imperatore, Central Apennines (Italy). *Journal of Structural Geology*, *90*, 185–206.

Faulkner, D., Lewis, A., & Rutter, E. (2003). On the internal structure and mechanics of large strike-slip fault zones: field observations of the Carboneras fault in southeastern Spain. *Tectonophysics*, *367*(3–4), 235–251.

Faulkner, D., Mitchell, T., Healy, D., & Heap, M. (2006). Slip on "weak" faults by the rotation of regional stress in the fracture damage zone. *Nature*, *444*(7121).

Faulkner, D. R., Jackson, C. A. L., Lunn, R. J., Schlische, R. W., Shipton, Z. K., Wibberley, C. A. J., & Withjack, M. O. (2010). A review of recent developments concerning the structure, mechanics and fluid flow properties of fault zones. *Journal of Structural Geology*, *32*(11), 1557–1575.

Fondriest, M., Smith, S. A., Di Toro, G., Zampieri, D., & Mittempergher, S. (2012). Fault zone structure and seismic slip localization in dolostones, an example from the Southern Alps, Italy. *Journal of structural Geology*, *45*, 52-67.

Fossen, H., & Rotevatn, A. (2016). Fault linkage and relay structures in extensional settings—A review. *Earth-Science Reviews*, *154*, 14–28.

Gold, P. O., Cowgill, E., Kreylos, O., & Gold, R. D. (2012). A terrestrial lidar-based workflow for determining three–dimensional slip vectors and associated uncertainties. *Geosphere*, *8*(2), 431-442.

Govoni, A., Marchetti, A., Gori, P., Bona, M., Lucente, F., Improta, L., et al. (2014). The 2012 Emilia seismic sequence (Northern Italy): Imaging the thrust fault system by accurate aftershock location. *Tectonophysics*, *622*, 44–55.

Hodgetts, D. (2013). Laser scanning and digital outcrop geology in the petroleum industry: A review. *Marine and Petroleum Geology*, *46*, 335–354.

Hsiao, L.-Y., Graham, S. A., & Tilander, N. (2004). Seismic reflection imaging of a major strike-slip fault zone in a rift system: Paleogene structure and evolution of the Tan-Lu fault system, Liaodong Bay, Bohai, offshore China. *AAPG Bulletin*, 71–97.

Jackson, J., & White, N. (1989). Normal faulting in the upper continental crust: observations from regions of active extension. *Journal of Structural Geology*, *11*(1–2), 15–36.

King, G., & Nabelek, J. (1985). Role of Fault Bends in the Initiation and Termination of Earthquake Rupture. *Science*, *228*(4702), 984–987.

Long, J. J., & Imber, J. (2012). Strain compatibility and fault linkage in relay zones on normal faults. *Journal of Structural Geology*, *36*, 16–26.

McCaffrey, K., Holdsworth, R., Imber, J., Clegg, P., De Paola, N., Jones, R., et al. (2005a). Putting the geology back into Earth models. *Eos, Transactions American Geophysical Union*, *86*(46), 461–466.

McCaffrey, K. J. W., Jones, R. R., Holdsworth, R. E., Wilson, R. W., Clegg, P., Imber, J., et al. (2005b). Unlocking the spatial dimension: digital technologies and the future of geoscience fieldwork. *Journal of the Geological Society*, *162*(6), 927–938.

Miller, S. A., Collettini, C., Chiaraluce, L., Cocco, M., Barchi, M. R., & Kaus, B. J. (2004). Aftershocks driven by a high-pressure CO2 source at depth, *Nature, 427*(6976), 724–727.

Mirabella, F., Barchi, M. R., Lupattelli, A., Stucchi, E., & Ciaccio, M. (2008). Insights on the seismogenic layer thickness from the upper crust structure of the Umbria-Marche Apennines (central Italy), *Tectonics, 27*(1).

Peacock, D. C. P., Dimmen, V., Rotevatn, A., & Sanderson, D. J. (2017). A broader classification of damage zones. *Journal of Structural Geology*, *102*, 179–192.

Pless, J., McCaffrey, K., Jones, R., Holdsworth, R., Conway, A., & Krabbendam, M. (2015). 3D characterization of fracture systems using Terrestrial Laser Scanning: an example from the

Lewisian basement of NW Scotland. *Geological Society, London, Special Publications*, *421*(1), 125–141.

Porreca, M., Minelli, G., Ercoli, M., Brobia, A., Mancinelli, P., Cruciani, F., et al. (2018). Seismic Reflection Profiles and Subsurface Geology of the Area Interested by the 2016–2017 Earthquake Sequence (Central Italy). *Tectonics*, *37*(4), 1116–1137.

Priest, S. D., & **Hudson, J. A.** (1981). Estimation of discontinuity spacing and trace length using scanline surveys. *Int. J. Rock Mech. Min. Sci. & Geomech. Abstr*, *18*, 183–197.

Rotevatn, A., Buckley, S., Howell, J., & **Fossen, H.** (2009). Overlapping faults and their effect on fluid flow in different reservoir types: A LIDAR-based outcrop modeling and flow simulation study, *AAPG Bulletin*, *93*(3), 407–427.

Rubin, A. M., Gillard, D., & **Got, J.-L.** (1999). Streaks of microearthquakes along creeping faults. *Nature*, *400*(6745), 23196.

Sagy, A., Brodsky, E. E., & **Axen, G. J.** (2007). Evolution of fault-surface roughness with slip. *Geology*, *35*(3), 283–286.

Sagy, A., & **Brodsky E.** (2009), Geometric and rheological asperities in an exposed fault zone, *J Geophys Res Solid Earth 1978 2012*, *114*(B2)

Schaff, D. P., Bokelmann, G. H., Beroza, G. C., Waldhauser, F., & **Ellsworth, W. L.** (2002). High-resolution image of Calaveras Fault seismicity. *Journal of Geophysical Research: Solid Earth (1978–2012)*, *107*(B9)

Seers, T. D., & **Hodgetts, D.** (2016). Probabilistic constraints on structural lineament best fit plane precision obtained through numerical analysis. *Journal of Structural Geology*, *82*, 37–47.

Sibson, R. H. (1994). Crustal stress, faulting and fluid flow. *Geological Society, London, Special Publications*, *78*(1), 69–84.

Sibson, R. H. (2003), Thickness of the Seismic Slip Zone, *Bulletin of the Seismological Society of America*, *93*(3), 1–10,

Siman-Tov, S., Aharonov, E., Sagy, A., & **Emmanuel, S.** (2013), Nanograins form carbonate fault mirrors, *Geology*, *41*(6).

Smeraglia, L., Berra, F., Billi, A., Boschi, C., Carminati, E., & **Doglioni, C.** (2016a). Origin and role of fluids involved in the seismic cycle of extensional faults in carbonate rocks. *Earth and Planetary Science Letters*, *450*, 292–305.

Smeraglia, L., Billi, A., Carminati, E., Cavallo, A., Di Toro, G., Spagnuolo, E., & **Zorzi, F.** (2017), Ultra-thin clay layers facilitate seismic slip in carbonate faults, *Scientific Reports*, *7*(1), 974.

Smeraglia, L., Aldega, L., Billi, A., Carminati, E., & **Doglioni, C.** (2016b). Phyllosilicate injection along extensional carbonate-hosted faults and implications for co-seismic slip propagation: Case studies from the central Apennines, Italy. *Journal of Structural Geology*, *93*, 29–50.

Smith, S., Billi, A., Di Toro, G., & **Spiess, R.** (2011), Principal Slip Zones in Limestone: Microstructural Characterization and Implications for the Seismic Cycle (Tre Monti Fault, Central Apennines, Italy), *Pure and Applied Geophysics*, *168*(12), 2365–2393.

Smith, S., Bistacchi, A., Mitchell, T. M., Mittempergher, S., & **Di Toro, G.** (2013). The structure of an exhumed intraplate seismogenic fault in crystalline basement. *Tectonophysics*, *599*, 29–44.

Tavani, S., Arbues, P., Snidero, Carrera, N., & **Muñoz, J.** (2011). Open Plot Project: an open-source toolkit for 3-D structural data analysis. *Solid Earth*, *2*(1), 53–63.

Telling, J., Lyda, A., Hartzell, P., & **Glennie, C.** (2017). Review of earth science research using terrestrial laser scanning. *Earth-Science Reviews, 169, 35-68.*

Tesei, T, Harbord, C., De Paola, N., Collettini, C., & **Viti, C.** (2018). Friction of Mineralogically Controlled Serpentinites and Implications for Fault Weakness. *Journal of Geophysical Research: Solid Earth*, *123*(8), 6976–6991.

Thiele, S. T., Lachlan, G., Samsu, A., Micklethwaite, S., Voggler, S. A., & **Cruden, A. R.** (2017). Rapid, semi-automatic fracture and contact mapping for point clouds, images and geophysical data. *Solid Earth*, *8*, 1241–1253.

Valoroso, L., Chiaraluce, L., & **Collettini, C.** (2014). Earthquakes and fault zone structure. *Geology*, *42*(4), 343–346.

Vasuki, Y., Holden, E.-J., Kovesi, P., & **Micklethwaite, S.** (2014). Semi-automatic mapping of geological Structures using UAV-based photogrammetric data: An image analysis approach. *Computers & Geosciences*, *69*, 22–32.

Ventura, G., & **Di Giovambattista, R.** (2012). Fluid pressure, stress field and propagation style of coalescing thrusts from the analysis of the 20

May 2012 ML5.9 Emilia earthquake (Northern Apennines, Italy). *Terra Nova, 25*(1), 72–78.

Vollgger, S. A., & **Cruden, A. R.** (2016). Mapping folds and fractures in basement and cover rocks using UAV photogrammetry, Cape Liptrap and Cape Paterson, Victoria, Australia. *Journal of Structural Geology*, *85*, 168–187.

Waldhauser, F., & **Ellsworth, W. L.** (2000). A Double-Difference Earthquake Location Algorithm: Method and Application to the Northern Hayward Fault, California. *Bulletin of the Seismological Society of America*, *90*(6), 1353–1368.

Walsh, J., **Bailey, W..**, **Childs, C.**, **Nicol, A.**, & **Bonson, C.** (2003). Formation of segmented normal faults: a 3-D perspective. *Journal of Structural Geology*, *25*(8), 1251–1262.

Wedmore, L. N. J., **Gregory, L. C.**, **McCaffrey, K. J. W.**, **Goodall, H.**, & **Walters, R. J.** (2019). Partitioned off-fault deformation in the 2016 Norcia earthquake captured by differential terrestrial laser scanning. *Geophysical Research Letters*, *46*(6), 3199-3205.

Wesnousky, S. G. (2006). Predicting the endpoints of earthquake ruptures. *Nature*, *444*(7117), 358–360.

Westoby, M. J., **Brasington, J.**, **Glasser, N. F.**, **Hambrey, M. J.**, & **Reynolds, J. M.** (2012),

.

"Structure-from-Motion" photogrammetry: A low-cost, effective tool for geoscience applications. *Geomorphology*, 179, 300–314.

Wibberley, C. A., **Yielding, G.**, & **Di Toro, G.** (2008). Recent advances in the understanding of fault zone internal structure: a review. From: Wibberley, C. A. J., Kurz, W., Imber, J., Holdsworth, R. E., & Collettini, C. (eds) *The Internal Structure of Fault Zones: Implications for Mechanical and Fluid-Flow Properties, 299*(1), 5–33. The Geological Society of London 2008.

Wilkinson, M. W., **Jones, R. R.**, **Woods, C. E.**, **Gilment, S. R.**, **McCaffrey, K. J. W.**, **Kokkalas, S.**, & **Long, J. J.** (2016), A comparison of terrestrial laser scanning and structure-from-motion photogrammetry as methods for digital outcrop acquisition, *Geosphere*, 12(6), 1865–1880.

Wilkinson, M., **Roberts, G. P.**, **McCaffrey, K.**, **Cowie, P. A.**, **Walker, J. P. F.**, **Papanikolaou, I.**, ... & **Wedmore, L.** (2015). Slip distributions on active normal faults measured from LiDAR and field mapping of geomorphic offsets: an example from L'Aquila, Italy, and implications for modelling seismic moment release. *Geomorphology*, *237*, 130-141

2. Strength evolution of simulated carbonate-bearing faults: The role of normal stress and slip velocity

Marco Mercuri[1], Marco Maria Scuderi[1], Telemaco Tesei[2*], Eugenio Carminati[1], and Cristiano Collettini[1,2]

1: Dipartimento di Scienze della Terra, Sapienza Università di Roma, P.le Aldo Moro 5, 00185 Roma, Italy
2: Istituto Nazionale di Geofisica e Vulcanologia, Via di Vigna Murata 605, 00143 Roma, Italy

Published in *Journal of Structural Geology* 109 (2018), 1-9

ABSTRACT

A great number of earthquakes occur within thick carbonate sequences in the shallow crust. At the same time, carbonate fault rocks exhumed from a depth < 6 km (i.e., from seismogenic depths) exhibit the coexistence of structures related to brittle (i.e., cataclasis) and ductile deformation processes (i.e., pressure-solution and granular plasticity). We performed friction experiments on water-saturated simulated carbonate-bearing faults for a wide range of normal stresses (from 5 to 120 MPa) and slip velocities (from 0.3 to 100 μm/s). At high normal stresses (σ_n > 20 MPa) fault gouges undergo strain-weakening, that is more pronounced at slow slip velocities, and causes a significant reduction of frictional strength, from μ = 0.7 to μ = 0.47. Microstructural analysis show that fault gouge weakening is driven by deformation accommodated by cataclasis and pressure-insensitive deformation processes (pressure solution and granular plasticity) that become more efficient at slow slip velocity. The reduction in frictional strength caused by strain weakening behaviour promoted by the activation of pressure-insensitive deformation might play a significant role in carbonate-bearing faults mechanics.

2.1. INTRODUCTION

The characterization of the mechanical behaviour of carbonate-bearing faults is crucial to better understand the physical processes at the origin of earthquakes that nucleate or propagate through thick carbonate sequences. Notable examples are provided by the Aigion event in 1995 in Greece (Bernard et al., 1997), the Wenchuan earthquake in 2008 in China (Burchfiel et al., 2008) and by several events occurring in Italy such as: the Umbria-Marche in 1997-98 (Miller et al., 2004; Mirabella et al., 2008), the L'Aquila 2009 (e.g., Valoroso et al., 2014), the Emilia 2012 (Ventura and Di Giovanbattista 2013; Govoni et al., 2014) and the 2016-17 seismic sequence in the Amatrice and Norcia areas (Pizzi et al., 2017).

Deformation structures hosted in the outcrops of carbonate-bearing faults exhumed from < 6 km, i.e. from crustal depths where most of the seismic sequences in Italy nucleate or propagate, provide the opportunity to get insights into fault rocks and deformation mechanisms. Cataclastic processes that induce grain size reduction and slip localization along millimetric-to-micron thick principal shear zones are widespread (e.g., Storti et al., 2003; Agosta and Aydin, 2006; De Paola et al., 2008; Smith et al., 2011; Collettini et al., 2014a). Cataclastic processes are often intimately associated with fluid assisted dissolution-precipitation and low temperature plasticity (Koopman, 1983; Kennedy and Logan, 1998; Tesei et al., 2013; Bullock et al., 2014; Wells et al., 2014; Viti et al., 2014). Diagnostic structures of fluid assisted dissolution-precipitation typically consist in pressure-solution seams (Fig. 2.1a) forming anastomosing foliations and slip surfaces (Fig. 2.1b). On the other hand, the evidences of granular plasticity are represented by twinning and sub-grains development (Fig. 2.1c; e.g., Kennedy and Logan, 1998; Siman-Tov et al., 2013; Collettini et al., 2014a). These observations indicate that during fault activity different deformation mechanisms coexist and potentially control the resulting frictional strength at depth. These mechanisms can be grouped into pressure-sensitive, i.e., cataclasis, and pressure-insensitive, i.e., pressure solution flow and intracrystalline plasticity (Rutter, 1986).

Several experimental studies have investigated the effects of microscale deformation processes on the mechanics of carbonate-bearing fault zones. At sub-seismic slip velocities and room temperature (i.e., v < 1 mm/s and T ~ 25 C°), it has been shown that deformation is mainly accommodated by cataclasis through the localization of grain size reduction within

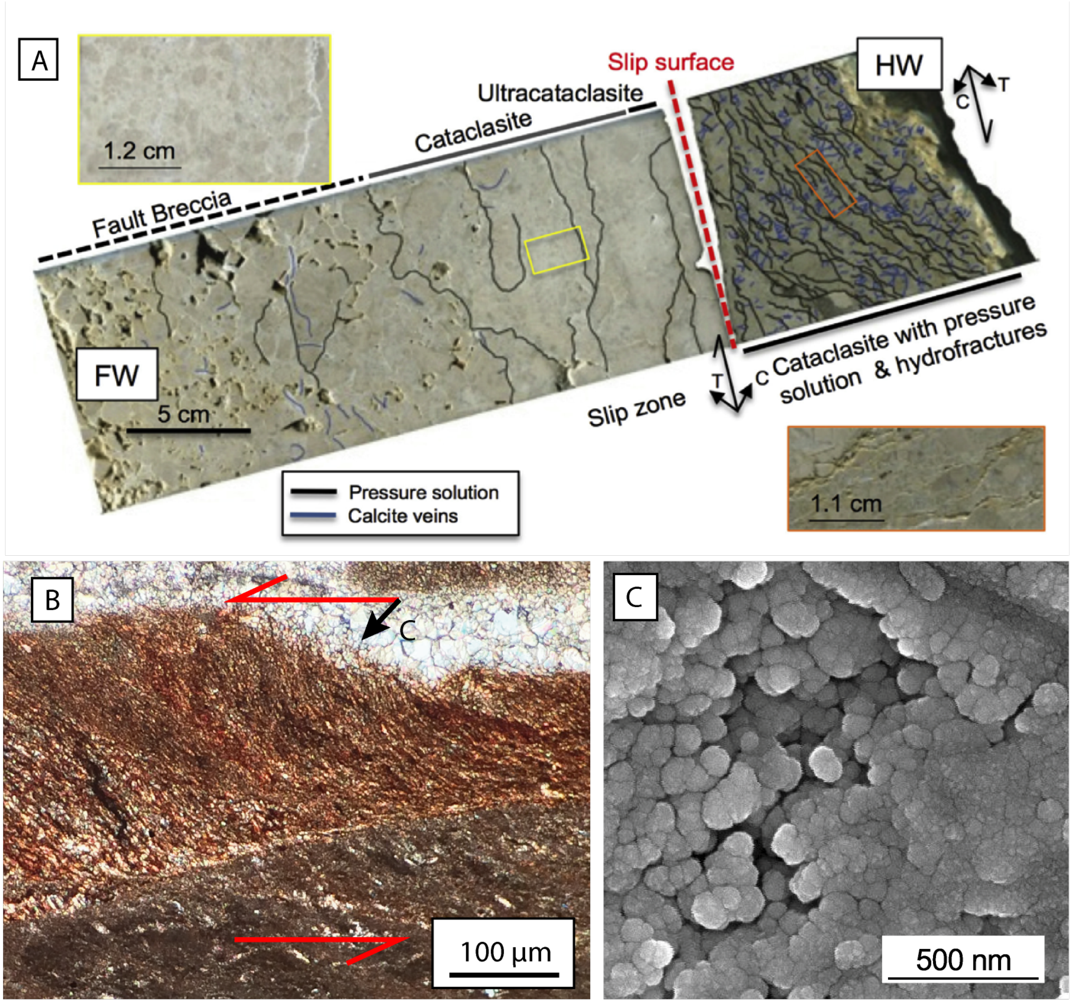

Figure 2.1 - Coexistence of pressure-sensitive (i.e., cataclasis) and pressure-insensitive deformation in carbonate fault rocks exhumed from seismogenic depths in the Northern Apennines. A) Typical cataclastic products (Fault Breccia, Cataclasite and Ultracataclasite; Sibson, 1977) are found together with pressure-solution seams in a transect through the core Monte Maggio fault, which display strong localization of slip also at the sample scale (Collettini et al., 2014a). B) Anastomosed foliation with S-geometry nearly orthogonal to the compression component (C) of the shear couple. This microstructure formed by pressure-solution and re-precipitation processes along a carbonate/clay fault (Tesei et al., 2013; Viti et al., 2014). C) Nanometer-scale subgrains in the Monte Maggio fault (De Paola et al., 2015).

the typical R-Y-B zones, in some cases associated with P-foliation (e.g. Logan et al., 1979, 1992). In addition, some studies have reported evidences for fluid-assisted dissolution and precipitation mechanisms (e.g. Carpenter et al., 2016), and granular plasticity represented by the formation of dense aggregates of nanograins (Tesei et al., 2017; Sagy et al., 2017). From these laboratory observations emerge the coexistence of pressure sensitive and insensitive processes governing the deformation style of carbonate-bearing simulated faults. This fault zone structure is commonly associated with high values of steady-state friction (μ_{ss}), that usually range between μ_{ss} ~ 0.7 (dry conditions) to μ_{ss} ~ 0.6 (saturated conditions) (Verberne et al., 2010, 2014; Carpenter et al., 2016). However, it has been shown that carbonate-bearing fault gouges can undergo significant frictional weakening under specific boundary conditions where pressure-insensitive deformation mechanisms are expected to be active, i.e., either high temperatures or slow deformation rates. For example, Verberne et al. (2015) showed a decrease in the coefficient of friction with increasing temperature from μ_{ss} ~ 0.55 at room temperature to μ_{ss} ~ 0.4 at 200 °C. Similarly, Carpenter et al. (2016) showed that the coefficient of friction at high normal stresses (i.e., σ_n = 100 MPa) decreases from μ_{ss} ~ 0.65 at 1 mm/s down to μ_{ss} ~ 0.51 at 0.1 μm/s. From these studies emerge that the activation of pressure insensitive micromechanical processes can decrease the frictional strength of carbonate-bearing fault zones with important implications for earthquake nucleation. However, these observations are sporadic and usually carried out from multiple stage experiments where the slip velocity is systematically varied to interrogate the velocity dependence of friction and/or frictional re-strengthening (e.g., Verberne et al., 2015; Carpenter et al., 2016). Each variation of slip velocity during the experiments can create a competition between micromechanical processes at the grain scale. In this context, the final microstructure is the sum of many processes that take place at different stages, making difficult to link the overall mechanical behaviour with the deformation mechanisms that accommodate shear.

In this work, we aim to better characterize the evolution of frictional strength along carbonate-bearing faults by performing shear experiments for a variety of normal stresses and slip velocities on simulated fault gouges of Carrara Marble. We inform the mechanical data with detailed microstructural analysis to shed light on the physical-chemical processes acting within carbonate-bearing fault zones varying the boundary conditions.

2.2. METHODS

We performed rock deformation experiments on powdered Carrara Marble (> 98% $CaCO_3$ content) to simulate a carbonate-bearing fault gouge and to investigate its frictional properties. Experiments were conducted using a biaxial apparatus, BRAVA (Brittle Rock deformAtion Versatile Apparatus; Collettini et al., 2014b), in the double-direct shear configuration (Fig. 2.2). In this configuration two servo-controlled rams apply a horizontal and vertical load to the sample (Fig. 2.2a). Load was measured with ± 0.03 kN accuracy load cells mounted at the extremity of both pistons and in contact with the sample assembly (Fig. 2.2a). Linear Variable Displacement

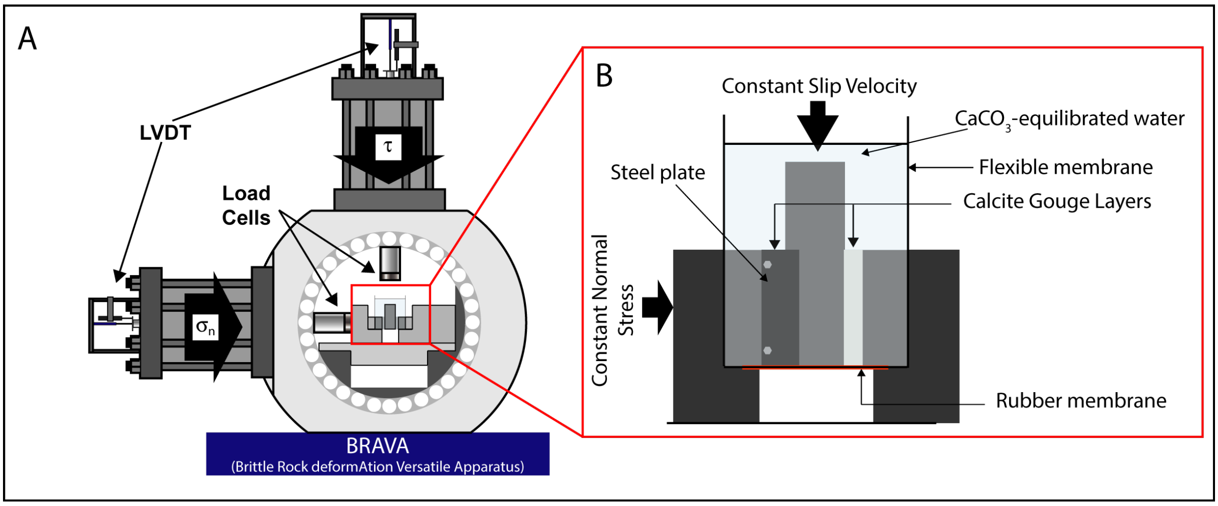

Figure 2.2 - (A) The biaxial servo-controlled apparatus used for this study (BRAVA in INGV, Rome; Collettini et al., 2014b). Horizontal and vertical load cells and LVDTs control and measure respectively loads and displacements. (B) The double direct shear configuration: two identical layers of gouge are comprised between three steel forcing blocks; a constant horizontal load is applied laterally and the central block is moved downward with constant velocity inducing symmetric shear within gouge layers.

Transformers (Fig. 2.2a) measured horizontal and vertical displacements with a precision of ± 0.1 μm. Both horizontal and vertical displacements were corrected taking in account for the elastic stiffness of the loading frame. For horizontal loads, smaller than 50 kN, on the grounds of calibration tests (e.g., Collettini et al., 2014b), elastic stiffness was 125.363 MPa/mm, while at higher loads we considered a stiffness value of 416.558 MPa/mm due to the non-linear elastic deformation of the apparatus at small loads. For the vertical piston, elastic stiffness was 116.801 MPa/mm for loads smaller than 50 kN, and 301.461 MPa/mm for higher loads. During experiments, we recorded loads and displacements, both in the horizontal and vertical direction, with a sampling rate ranging from 1 to 100 Hz depending on the target slip velocity (we registered at least one measurement every micron of slip).

Carrara Marble was preliminary grinded and passed through a 125 μm sieve. All the particles that passed through the sieve were included in the starting material. Two identical, ~ 5 mm thick gouge layers were constructed upon stainless steel forcing blocks with nominal frictional contact area of 5 cm × 5 cm and both were assembled with the central forcing block composing a symmetric assembly (Fig. 2.2b). To avoid slip at the interface between fault gouge and steel, and ensure that shear localizes within the gouge, the surfaces of the forcing blocks were machined with grooves 0.8 mm high and spaced 1 mm. To prevent excessive gouge extrusion during shear, a rubber membrane and steel plates were fixed below

Experiment name	Normal stress, σ_n (MPa)	Slip velocity (μm/s)	Total Displacement (mm)	Total shear strain, γ
b555	10	10	19.6	10.3
b556	20	10	19.9	8.5
b561	50	10	19.9	10.4
b562	5	10	20.3	5.8
b563	10	100	20.3	9.9
b564	100	10	20.3	12.3
b566	50	100	20.2	10.4
b567	5	100	20.2	7.9
b568	100	100	19.8	11.6
b600	100	1	21.3	14.6
b602	50	1	20.4	9.1
b603	10	1	21.2	10.1
b604	10	0.3	8.2	3.6
b605	50	0.3	7.2	3.8
b606	100	0.3	5.7	3.9
b631	20	1	19.2	8.5
b638	5	1	19.6	10.3
b639	100	0.3	16.9	9.6
b640	120	0.3	13.8	7.6
b641	120	10	18.5	12.0
b642	80	10	18.6	13.0
b643	80	0.3	18.4	11.9
b651	10	0.3	20.0	11.6
b675	100	10	13.6	9.7

Table 2.1 - Summary of experiments and boundary conditions. All tests were conducted under $CaCO_3$-equilibrated water saturated conditions.

and laterally of the sample assembly respectively (Fig. 2.2b).

We conducted 24 experiments (Table 2.1) at room temperature (i.e., ~25°C) and water saturated boundary conditions. As pore fluid, we used a $CaCO_3$-equilibrated water solution to simulate a realistic pore fluid chemistry along shallow-crustal carbonate fault zones. For each experiment, once the assembly was positioned within BRAVA, it was left saturating within a flexible membrane containing $CaCO_3$ equilibrated water for 45 minutes under a normal load of 1 kN (Fig. 2.2b). At this stage, we increased the normal stress to the desired target value that ranged between 5 and 120 MPa and left the sample to compact until a steady layer thickness was attained. The time for the compaction of the sample was ~15 minutes, depending on the target normal stress. The vertical ram was then advanced at constant displacement rate to apply shear stress and induce deformation within the sample. We conducted experiments for a range of shear velocities between 0.3 μm/s and 100 μm/s and a total shear displacement between 5 and 20 mm (Table 2.1). In addition, we performed unloading-loading cycles every 5 mm of displacement (Fig. 2.3) to characterize stiffness and shear modulus of the fault gouge but these data are not presented here.

At the end of each experiment, the deformed gouge layers were collected, impregnated with epoxy resin and standard thin section were cut parallel to the slip direction for microstructural analysis (optical microscope and Scanning Electron Microscope, SEM-backscattered electron mode). In addition, gouge layers deformed in experiment b675 (see Table 2.1) were left drying and observed at the SEM operated in secondary electron mode without the epoxy resin impregnation.

Normal stress (σ_n) was calculated dividing the applied normal load by the surface of the side block (0.0025 m^2). Similarly, shear stress (τ) was calculated dividing vertical load by 0.005 m^2 (two surfaces of application). We calculated the coefficient of friction dividing shear stress by normal stress, and assuming no-cohesion for a powdered material. The values of the steady state friction coefficients, μ_{ss} reported in the following, were measured as the average friction after the initial loading phase (shear strain > 3), without considering the unloading-loading cycles (Fig. 2.3). For experiments with a significant weakening after a shear strain of 3, this further evolution of friction with strain is included as standard deviation from the mean value (e.g., vertical bars in Fig 2.4). Layer thickness was calculated subtracting horizontal displacement values to the initial pre-shear value measured using a calliper. In addition, we corrected layer thickness for geometrical thinning and evaluated the shear strain accordingly (Scott et al., 1994).

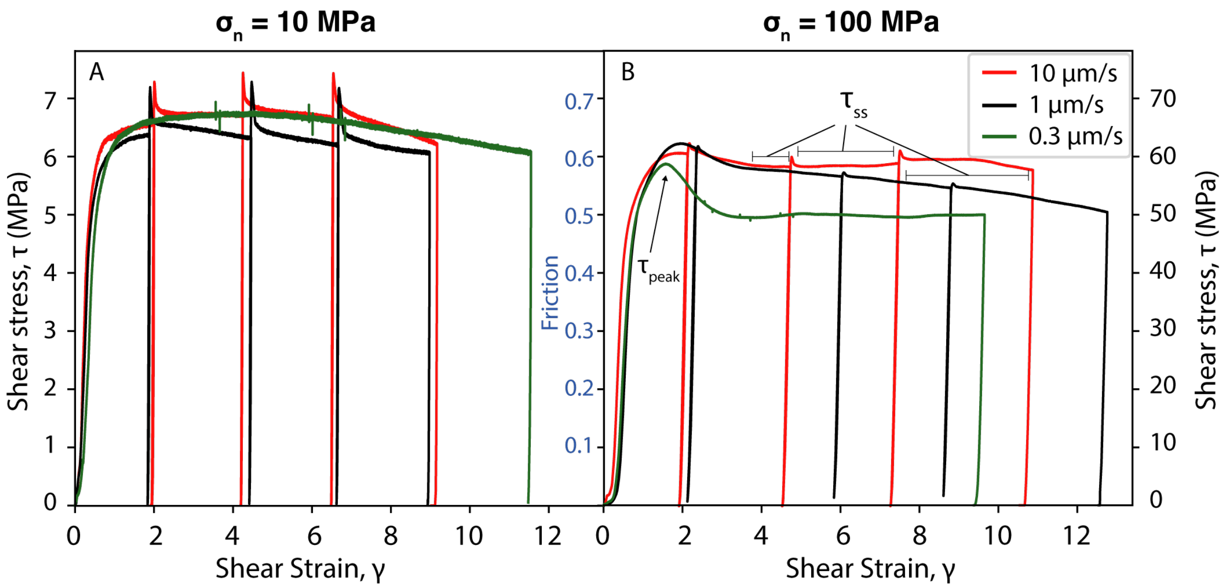

Figure 2.3 - Shear stress (τ) and friction (μ) evolution with shear strain (γ) for experiments performed at (A) 10 and (B) 100 MPa at different slip velocities. The portion of the curve where peak and steady-state shear stress were collected, see methods for details, is marked by τ_{peak} and τ_{ss} respectively.

2.3. RESULTS

2.3.1. Frictional behaviour

The mechanical behaviour of simulated calcite fault gouges is controlled by applied normal stress and imposed slip velocity. At low normal stress, e.g., σ_n = 10 MPa, the shear strength reaches a steady state value (τ_{ss}) after a few millimetres of slip and it remains nearly constant until the end of the experiment (Fig. 2.3a). This trend is independent on the applied slip velocity (Fig. 2.3a) and defines a steady state coefficient of friction (μ_{ss}) of about 0.65 (Figs. 2.3a and 2.4b). Differently from the experiments at low normal stress, at high normal stress, e.g., σ_n = 100 MPa, we document that shear strength evolves following three main stages. In stage one, after the initial nearly-elastic loading phase, the shear strength reaches a peak value (τ_{peak} in Fig. 2.3b) that corresponds to a friction of ~ 0.6 that is independent of the applied slip velocity (Fig. 2.3b). With increasing displacement, during stage two, we document a strain-weakening phase that depends on the imposed slip velocity. We observe that at slow slip velocities the strain weakening phase is more pronounced when compared with higher slip velocities (Fig. 2.3b). During stage three, fault gouge reaches a new steady state frictional sliding regime. As a consequence of stage two, the new values of frictional strength at steady state are lower for slower sliding velocities (Figs. 2.3b and 2.4b). For instance, at a slip velocity of 0.3 μm/s the corresponding steady state value of friction is ~ 0.5, which is lower when compared to that at a slip velocity of 10 μm/s where μ_{ss} ~ 0.6 (Figs. 2.3b and 2.4b).

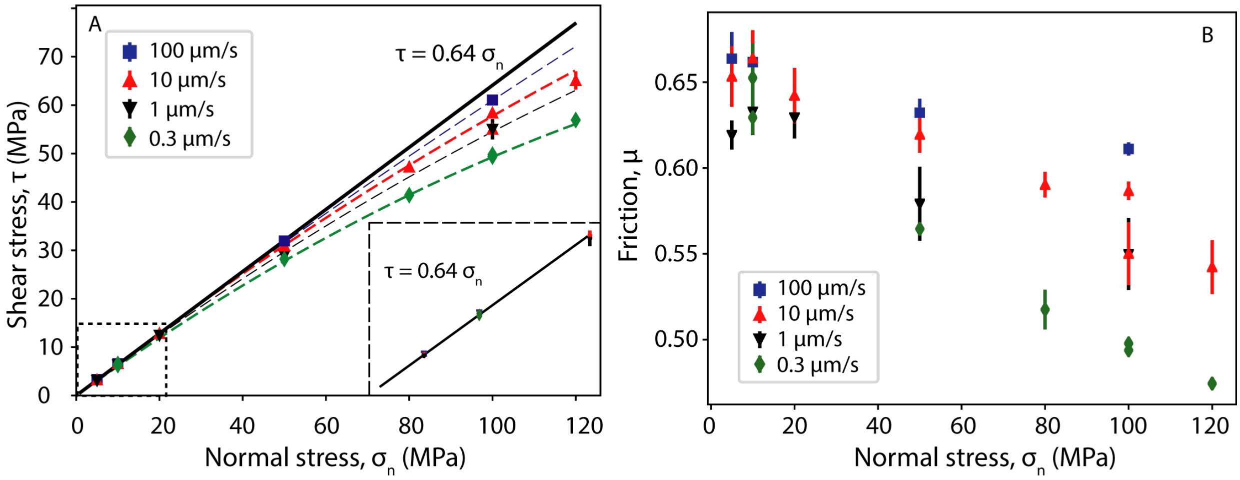

Figure 2.4 - A) Evolution of shear strength τ vs. normal stress σ_n, for different slip velocities. Black line represents Mohr-Coulomb failure envelope for experiments performed at $\sigma_n \leq 20$ MPa (inset). At high normal stresses and slow slip velocities, a second-order polynomial function provides a better fit than the classical linear Coulomb regression data. B) Mean steady-state friction coefficient, μ_{ss}, plotted against normal stress for different slip velocities. The variability of friction observed during each experiment is represented by the vertical bars (see methods for details).

The relationship between shear and normal stresses, when analysed in a Coulomb diagram, highlights two different regions (Fig. 2.4a). Below σ_n ~ 20 MPa, shear strength increases linearly with normal stress and is independent of the imposed slip velocity (Fig. 2.4a). The Coulomb failure envelope is described by a straight line with a slope μ = 0.64 (solid black line in Fig. 2.4a), representing the average coefficient of friction. Within this range of normal stresses, the coefficient of friction is independent on slip velocity and is comprised between 0.62 (σ_n = 5 MPa, v = 1 μm/s) and 0.66 (σ_n = 10 MPa, v = 10 μm/s) (Fig. 2.4b). For normal stress higher than 20 MPa, the relationship between shear strength and normal stress deviates from the linearity, in particular at slow slip velocity (Fig. 2.4a). Under the same imposed normal stress, slower slip velocities promote lower values of friction (Fig. 2.4b) and this is more pronounced at higher normal stresses (Fig. 2.4b). For example, at σ_n = 50 MPa, μ_{ss} decreases by ~11% (from 0.63 to 0.56) for slip velocity decreasing from 100 μm/s to 0.3 μm/s, whilst at σ_n = 100 MPa μ_{ss} decreases by ~19% (from 0.61 to 0.49) for the same range of slip velocities. For a fixed slip velocity, the steady-state friction decreases with increasing normal stress. This trend is more pronounced at slower slip velocities (Fig. 2.4b). For example, at slip velocity of 10 μm/s, friction decreases by ~ 5% (from 0.62 to 0.59) for normal stress increasing from 50 to 100 MPa, whilst at 0.3 μm/s, friction decreases by ~11% (from 0.56 to 0.49) for the same range of normal stresses (Fig 2.4b).

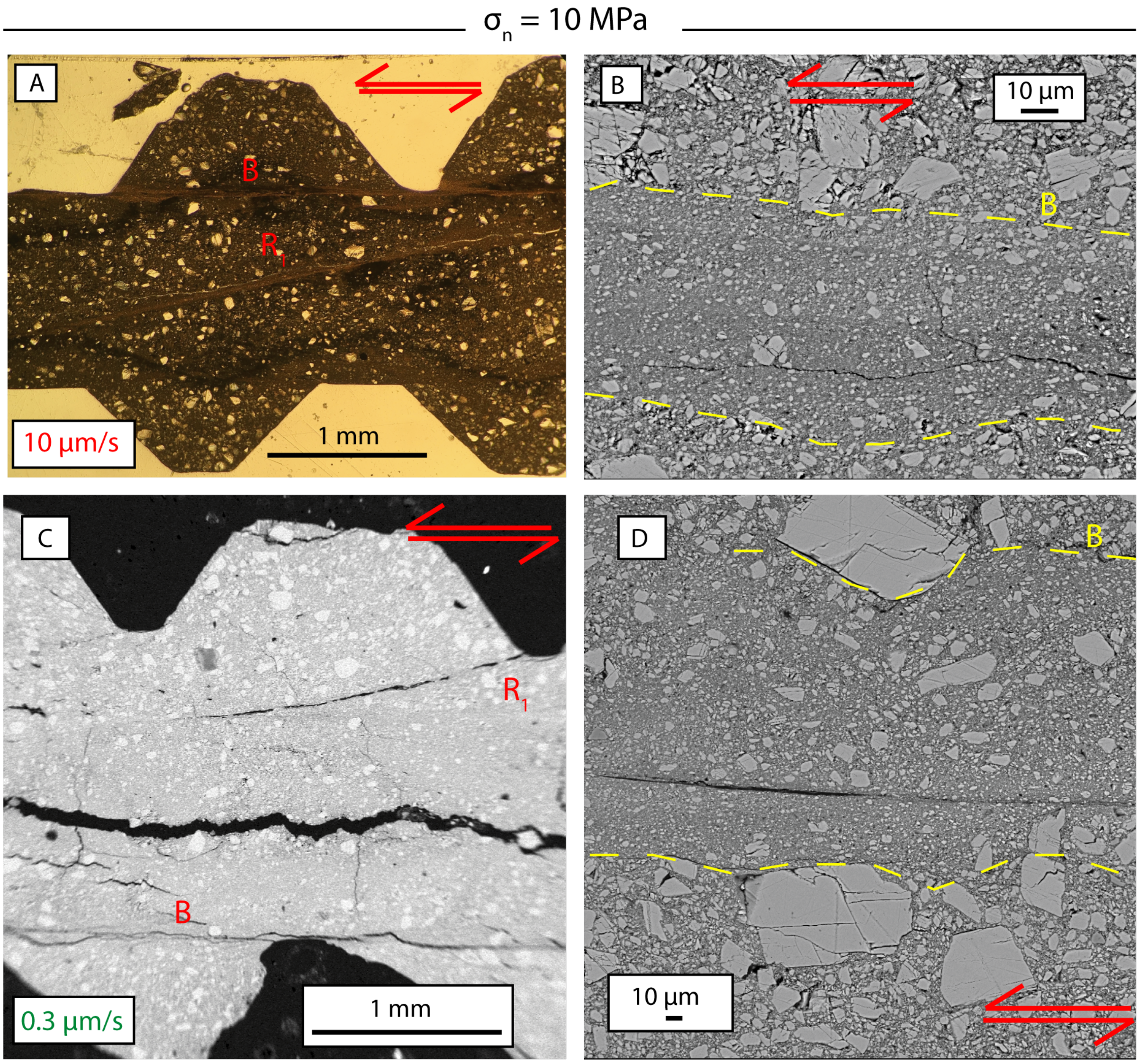

Figure 2.5 - Microstructures of simulated calcite fault gouges deformed at low normal stress (σ_n = 10 MPa) and at slip velocity of 10 µm/s (A, B) and 0.3 µm/s (C, D). Figures A and B are from experiment b555, whilst figures C and D are from the experiment b651 (see Table 2.1). Deformation localizes into B and R_1 zones (A, C) that are represented by 100 to 200 µm-thick shear zones characterized by higher grain comminution than the bulk gouge layer (B, D). Figure A is an optical micrograph (plane polarized light), whilst B, C, D are from SEM microscope in backscattered mode.

2.3.2. Microstructural observations

2.3.2.1. Low normal stress microstructures

At low normal stresses ($\sigma_n \leq$ 20 MPa), deformation is localized in B and R_1 shear zones (Logan, 1979) that are observed at both high, v = 10 µm/s (Fig. 2.5a), and slow, v = 0.3 µm/s, slip velocity (Fig. 2.5c). B and R_1 consist of 100 to 200 µm-thick shear zones characterized by higher grain comminution when compared to the bulk gouge layer (Fig. 2.5b,d). In detail, these zones are characterized by angular grains typically smaller than 10 µm (Fig. 2.5b,d), whilst in the surrounding the grain size is larger and characterized by angular clasts with heterogeneous grain size distribution (Fig. 2.5a,c) resembling the undeformed gouge. Comparing gouge layers sheared at

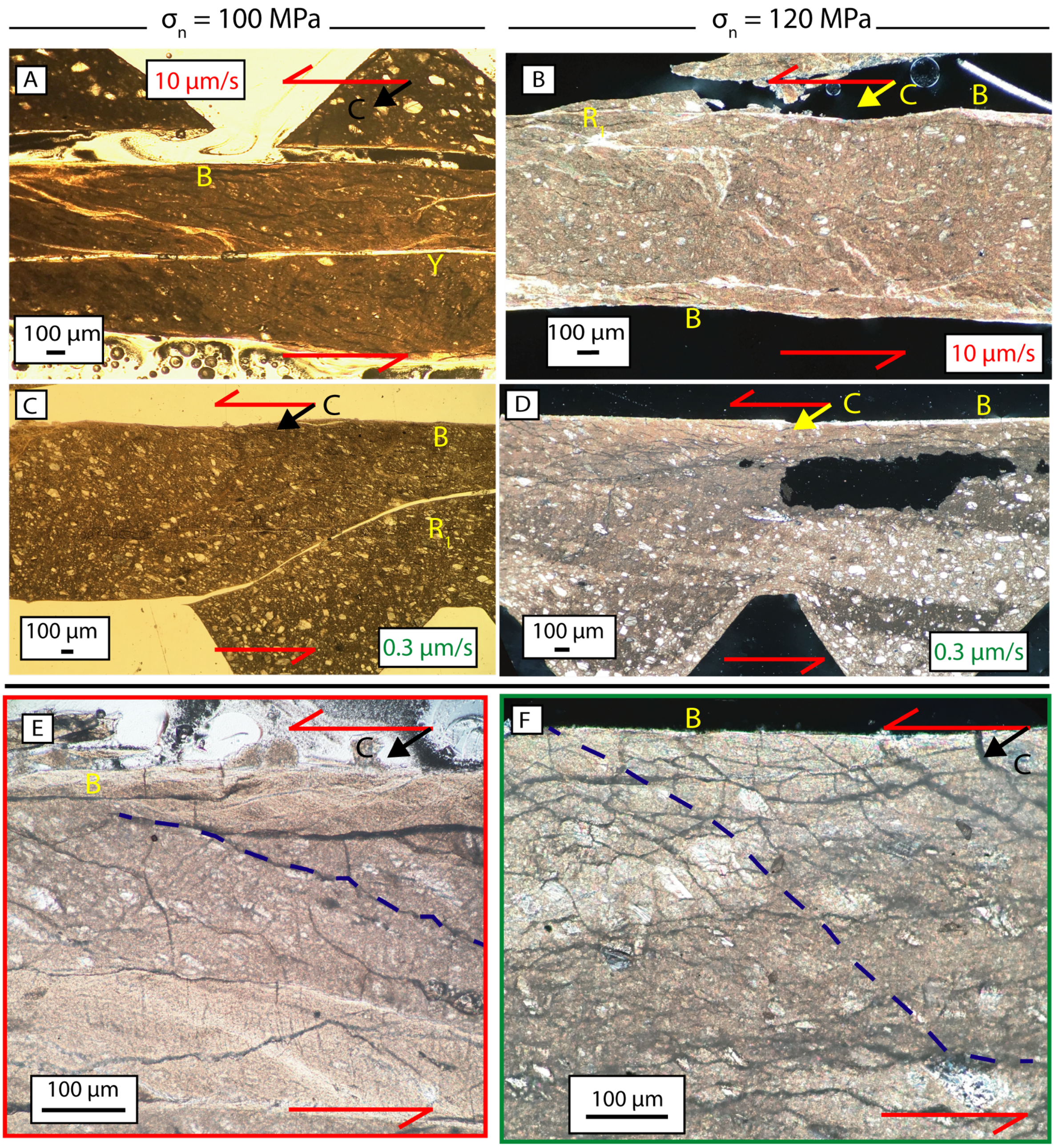

Figure 2.6 - Optical micrographs of simulated fault gouges deformed at a relatively high normal stress (σ_n = 100 MPa for the left column and σ_n = 120 MPa on the right one) and at slip velocity of 10 µm/s (A, B, E) and 0.3 µm/s (C, D, F). Figures A, C and E derive from observations at plane polarized light, whilst figures B, D and E are from observation at cross polarized light. The micrographs are derived from experiments b564 (A, E), b641 (B), b639 (C) and b640 (D, F); experiments are listed in Table 2.1. Deformation is distributed within the entire gouge layer (A, B, C. D) and is characterized by strong grain size reduction and the development of an anastomosed foliation, which is interpreted as oriented orthogonal to the normal stress component, C, of the shear couple. Grain comminution is more pronounced at higher slip velocities (Fig. A vs C and Fig. B vs. D). A detail of the anastomosed foliation at a slip velocity of 10 µm/s and 0.3 µm/s is presented in Fig. E and F respectively.

the same normal stress conditions but with different slip velocities, we do not observe substantial differences (Fig. 2.5).

2.3.2.2. High normal stress microstructures

The microstructures retrieved from experiments performed under high normal stresses (σ_n > 20 MPa) show dramatically

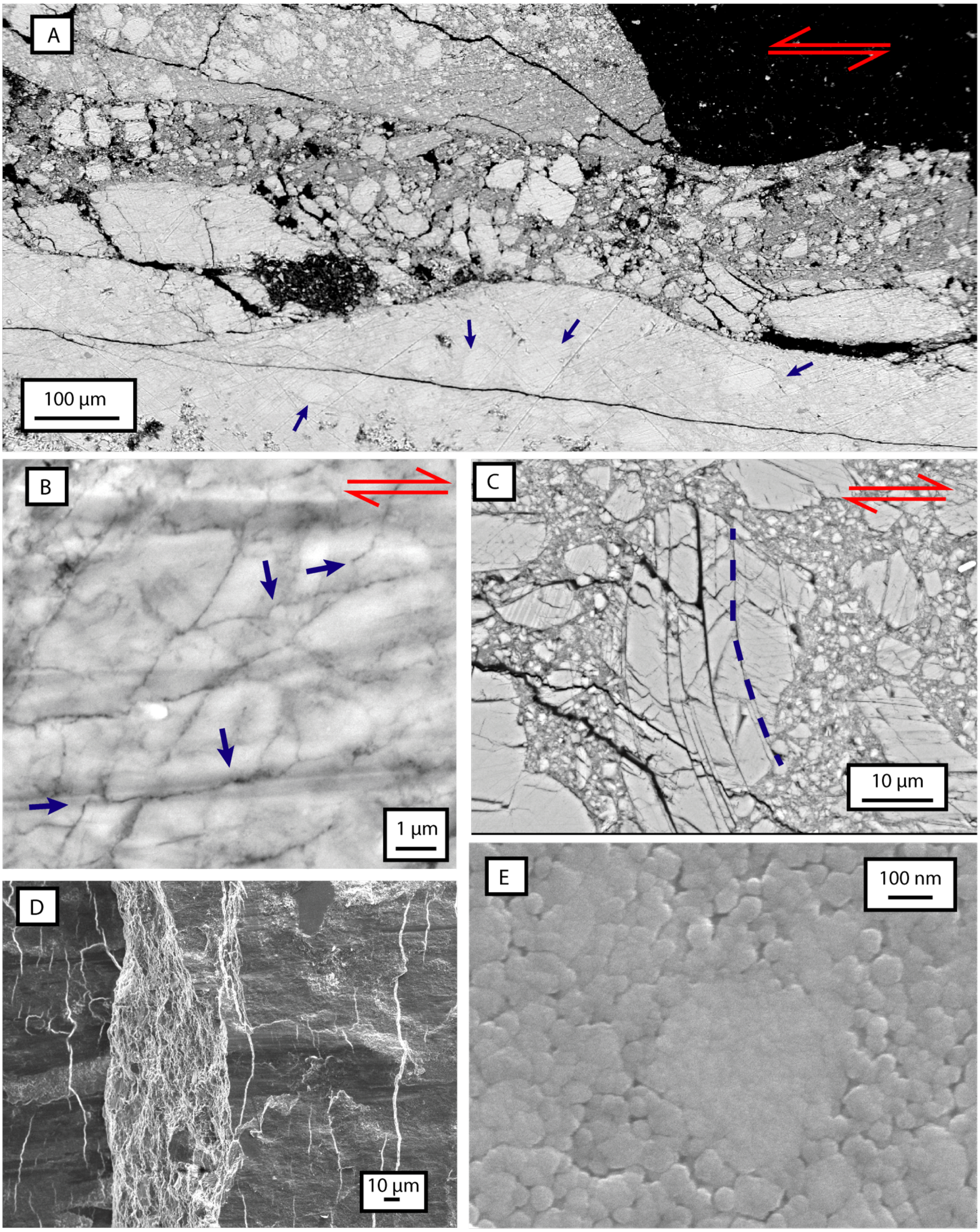

Figure 2.7 - SEM micrographs in simulated calcite fault gouges deformed under relatively high normal stresses, i.e., 120 (A, B) and 100 MPa (C, D, E). A) Large cemented portion of the gouge deformed during the experiment b640 (Table 2.1). Blue arrows indicate grains within the cemented portion. B) Sutured grain contacts with indentations (blue arrows) in the experiment b640 (Table 2.1). C) Folded calcite grain in the experiment b564 (Table 2.1). Shear zones are often striated (D) and constituted by dense aggregates of nanograins (E); the figures D and E are from the experiment b675.

different features when compared with low normal stresses experiments. In general, we observe: 1) that shear deformation is distributed within the entire gouge, 2) the development of a pervasive anastomosing foliation and, 3) the development of very sharp principal slip zones with B geometry (Logan, 1979; Fig. 2.6a-d), associated with R_1 and Y fabric (Fig. 2.6a,c; see also Fig. 2.7c). The pervasive foliation is oriented at high angles to the ideal normal stress component of the shear couple (e.g. Ramsay, 1967) for both fast (Fig. 2.6a,b,e) and slow (Fig. 2.6c,d,f) slip velocities, showing a characteristic S-shape (Berthé et al., 1979; see Fig. 2.6) Apart from the common features mentioned above, only for the experiments at 10 μm/s, we observe pervasive grain comminution throughout the entire sample, although a few relict grains with dimensions of hundreds of microns are still present (Fig. 2.6a,b). At slow slip velocity (0.3 μm/s) larger grains are contained within a finer matrix and grain size reduction tends to increase approaching the B shear surface (Fig. 2.6c, d).

Looking at the details of fault zone structure we document the following features. (1) Large portions of the experimental faults are cemented (Fig. 2.7a). The cemented regions contain grain aggregates that are reworked by cataclastic processes (Fig. 2.7a) and are particularly evident in the sample collected at slow slip velocity (i.e., 0.3 μm/s). (2) The foliated zones consist of grains with sutured boundaries and local indentations (Fig. 2.7b). (3) The presence of grains that are folded along the pre-existing twinning planes (Fig 2.7c). Finally, when the principal slip zone is observed in plain view, it reveals (4) the presence of smooth striations (Fig. 2.7d) and packages characterized by very densely-packed nanoparticles with a polygonal geometry (10-150 nm in diameter; Fig. 2.7e).

2.4. Discussion

Our results show that the mechanical behaviour of simulated carbonate-bearing faults strongly depends on the applied normal stress and is modulated by the imposed slip velocity (Figs. 2.3-2.4). A marked change of behaviour occurs at a normal stress of ~ 20 MPa (Fig. 2.4) in agreement with previous experiments carried out on intact (Paterson, 1958; Fredrich et al., 1989) and powdered (Carpenter et al., 2016) Carrara Marble. In particular, at relatively low values of normal stress ($\sigma_n \leq 20$ MPa) we observe a nearly constant steady-state shear strength that is not affected by accumulated shear displacement and imposed slip velocity (Fig. 2.3a). This behaviour favours a linear relationship between shear stress and normal stress described by a failure envelope with a slope of $\mu = 0.64$ (Fig. 2.4a), which is in general agreement with other studies on calcite-rich lithologies (e.g., Verberne et al., 2010, 2014; Carpenter et al., 2014; Tesei et al., 2014; Chen et al., 2015). Furthermore, we observe that deformation localizes within shear bands characterized by strong grain size reduction and with B and R_1 geometries (Fig. 2.5). The coupling of the mechanical behaviour and microstructural observations indicates that, at low normal stress, the mechanical behaviour is controlled by pressure-sensitive deformation (i.e., cataclasis) with localization along B and R shear planes.

For the experiments performed at higher normal stress (i.e., σ_n > 20 MPa), we observe that shear strength evolves in three stages with accumulated displacement, reaching a peak that is followed by a strain-weakening phase before attaining a steady state value (Fig. 2.3b). As a result of this behaviour, we document a non-linear relationship between shear and normal stress that is more pronounced at slow slip velocities (Fig. 2.4a). The observed weakening can be interpreted by considering the interplay of different processes: 1) cataclasis, 2) fluid-rock interaction, which favours fluid assisted dissolution and precipitation processes, and 3) intragranular plasticity. Coupling mechanical data with microstructural observations we note that shear is accommodated by a distributed deformation, accomplished through pervasive grain size reduction and the development of a pervasive foliation (Fig. 2.6). The anastomosing foliation (Fig. 2.6), the presence of densely-packed grains with sutured contacts and local grain indentations (Fig. 2.7b) suggest that fluid assisted dissolution and precipitation processes played an important role, inducing compaction and dissolution of smaller grains (e.g., Rutter 1983; Gratier and Gamond 1990). Large cemented portions of the experimental fault (Fig. 2.7a) represent a direct evidence of calcite precipitation and strengthens the hypothesis of the activity of fluid-assisted diffusion mass transfer (i.e., pressure-solution + transport + precipitation; Rutter 1983; Gratier et al., 2013). A further evidence of the role played by fluid assisted diffusion mass transfer in fault weakening can be inferred comparing mechanical data retrieved from an experiment conducted under nominally dry conditions (i.e., relative humidity <5%) and at high normal stress with the saturated experiments (Fig. 2.8). Under dry conditions the shear strength is high, μ = 0.7, and we do not observe the characteristic strain weakening reported under saturated conditions (Fig. 2.8). Furthermore, the presence of folded grains (Fig. 2.7c) and densely-packed nanoparticles (Fig. 2.7e) that form the principal slip surfaces (Fig. 2.7d) indicates

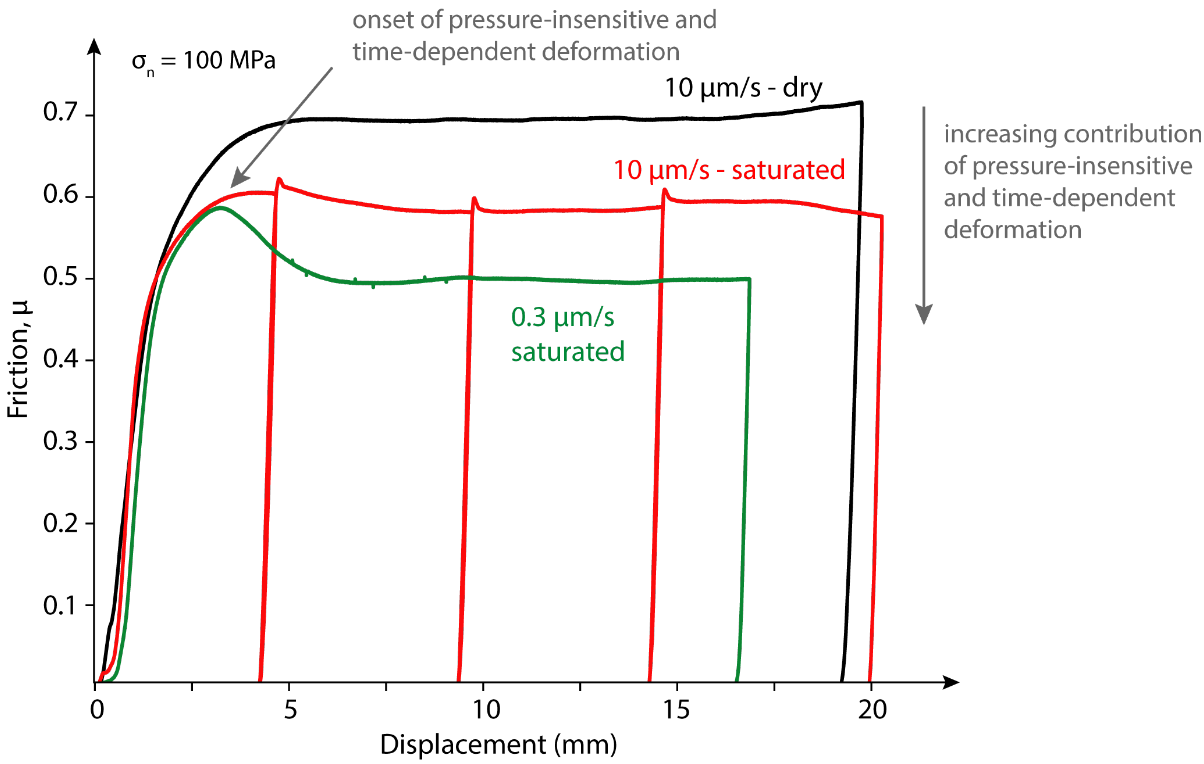

Figure 2.8 - Evolution of friction with displacement for experiments at normal stress of 100 MPa in saturated conditions at a slip velocity of 0.3 µm/s (green) and 10 µm/s (red) and for an experiment performed dry and at slip velocity of 10 µm/s.

that granular plasticity was also active during deformation (Kennedy and Logan, 1998; Tesei et al., 2017).

To summarize, our microstructural observations suggest that at high normal stress (i.e., σ_n > 20 MPa) pressure-insensitive deformation mechanisms (i.e., pressure-solution flow and intra-crystalline plasticity; Rutter, 1986) work together with pressure-sensitive mechanisms (i.e., cataclasis) in accommodating shear deformation. We suggest that with increasing normal stress, the activation of pressure-insensitive deformation mechanisms is responsible for the strain weakening phase (Fig. 2.3b) and for the transition from a linear relationship between shear strength and normal stress (i.e., purely pressure-sensitive) to a more non-linear relationship (i.e., less pressure-sensitive). Since both the strain weakening phase and the departure from the linear behaviour are more evident at slow slip velocities (Figs. 2.3b and 2.8), we posit that time-dependent mechanisms (i.e., pressure-solution flow and granular plasticity) increase their role in accommodating shear deformation with decreasing slip velocity because of the longer contact time between grains that favours their dissolution.

The range of normal stresses investigated in our experiments together with saturated fluid conditions allow us to get insights on the mechanics of carbonate-bearing faults at seismogenic depths (between 1 and ~ 10 km). Our results suggest that the activation of fluid assisted diffusion mass transfer and grain plasticity can significantly reduce the frictional strength of carbonate-bearing faults, from 0.7 to 0.47 in friction, facilitating fault slip. This observation has important implications for our understanding of frictional processes associated with the nucleation of unstable slip, when slip velocity is still slow. In this context, fluid rock interaction weakens the fault favouring the onset of slip. Then, as slip accelerates, the onset of dynamic slip will be controlled by the rate dependence of friction and the local generation of high pore fluid pressure, which can promote seismic slip even if the fault is characterized by rate strengthening behaviour (Scuderi et al., 2017). This mechanism is appealing in relation to the seismicity observed along the Apennines, where the coupling of high fluid pressure (e.g., Miller et al., 2004; Lucente et al., 2010) and fluid-rock interaction, can potentially promote earthquake.

2.5. CONCLUSION

We investigated the coupling between mechanical and microstructural features of carbonate-bearing faults by performing shear experiments on powdered Carrara Marble under saturated boundary conditions. We explored a range of normal stresses (5 MPa $\leq \sigma_n \leq$ 120 MPa) and slip velocities (0.3 μm/s $\leq v \leq$ 100 μm/s) to shed light on the time-dependent physico-chemical processes that control the evolution of fault zone strength. We observe that an increase in normal stress promote fault zone weakening through the activation of pressure-insensitive deformation mechanisms. Comparing microstructures from low to high normal stress we report a transition from localized to distributed deformation associated with the development of an anastomosed foliation. We suggest that the different micromechanical processes, such as pressure solution flow and granular plasticity, accommodating shear deformation are responsible for the evolution from a linear to a non-linear Coulomb envelope.

Since the coexistence of cataclastic and pressure-insensitive deformation is a typical feature of carbonate fault rocks exhumed from seismogenic depths, we suggest that the shear strength weakening documented in our experiments is relevant for the mechanics of faults hosted in carbonate sequences.

ACKNOWLEDGMENTS

We thank Dr. Steven Smith and an anonymous reviewer, whose comments greatly improved the manuscript. We also thank Brett Carpenter and Carolina Giorgetti for useful discussion, Domenico Mannetta (Mimmo) for high quality thin sections preparation, and Manuela Nazzari for her technical assistance with the SEM at the HP-HT laboratory at INGV, Rome. This research was supported by ERC Starting Grant nr. 259256 "GLASS" and Sapienza Progetti Ricerca Ateneo 2015 to CC, Horizon 2020 under the Marie Sklodowska-Curie action, No. 748400 STRAIN to TT, and Horizon 2020 under the Marie Sklodowska-Curie action, No. 656676 FEAT to MMS.

REFERENCES

Agosta, F. & **Aydin, A.** (2006). Architecture and deformation mechanism of a basin-bounding normal fault in Mesozoic platform carbonates, central Italy. *Journal of Structural Geology* 28, 1445–1467.

Bernard, P., Briole, P., Meyer, B., Lyon-Caen, H., Gomez, J.M., Tiberi, C., Berge, C., Cattin, R., Hatzfeld, D., Lachet, C., Lebrun, B., Deschamps, A., Courboulex, F., Larroque, C., Rigo, A., Massonnet, D., Papadimitriou, P., Kassaras, J., Diagourtas, D., Makropoulos, K., Veis, G., Papazisi, E., Mitsakaki, C., Karakostas, V., Papadimitriou, E., Papanastassiou, D., Chouliaras, & M., Stavrakakis, G. (1997). The Ms=6.2, June 15, 1995 Aigion earthquake (Greece): evidence for low angle normal faulting in the Corinth rift. *Journal of Seismology* 1, 131–150.

Berthé, Choukroune, & **Jegouzo**, 1979. Orthogneiss, mylonite and non coaxial deformation of granites: the example of the South Armorican Shear Zone. *Journal of Structural Geology* 1, 31–42.

Bullock, R.J., De Paola, N., Holdsworth, & **R.E., Trabucho-Alexandre, J.**, 2014. Lithological controls on the deformation mechanisms operating within carbonate-hosted faults during the seismic cycle. *Journal of Structural Geology* 58, 22–42.

Burchfiel, B.C., Royden, L.H., van der Hilst, R.D., Hager, B.H., Chen, Z., King, R.W., Li, C., Lü, J., Yao, H. & **Kirby, E.**, 2008. A geological and geophysical context for the Wenchuan earthquake of 12 May 2008, Sichuan, People's Republic of China. *GSA Today* 18, 4.

Carpenter, B.M., Collettini, C., Viti, C., & **Cavallo, A.** (2016). The influence of normal stress and sliding velocity on the frictional behaviour of calcite at room temperature: insights from laboratory experiments and microstructural observations. *Geophysical Journal International* 205, 548–561.

Carpenter, B.M., Scuderi, M.M., Collettini, C. & **Marone, C.** (2014). Frictional heterogeneities on carbonate-bearing normal faults: Insights from the Monte Maggio Fault, Italy. *Journal of Geophysical Research: Solid Earth* 119, 9062–9076.

Chen, J., Verberne, B.A. & **Spiers, C.J.** (2015). Interseismic re-strengthening and stabilization of carbonate faults by "non-Dieterich" healing under hydrothermal conditions. *Earth and Planetary Science Letters* 423, 1–12.

Collettini, C., Carpenter, B.M., Viti, C., Cruciani, F., Mollo, S., Tesei, T., Trippetta, F., Valoroso, L. & **Chiaraluce, L.**, (2014a). Fault structure and slip localization in carbonate-bearing normal faults: An example from the Northern Apennines of Italy. *Journal of Structural Geology* 67, 154–166.

Collettini, C., Di Stefano, G., Carpenter, B., Scarlato, P., Tesei, T., Mollo, S., Trippetta, F., Marone, C., Romeo, G. & **Chiaraluce, L.**, (2014b). A novel and versatile apparatus for brittle rock deformation. *International Journal of Rock Mechanics and Mining Sciences* 66, 114–123.

De Paola, N., Collettini, C., Faulkner, D.R., & **Trippetta, F.** (2008). Fault zone architecture and deformation processes within evaporitic rocks in the upper crust. *Tectonics* 27.

De Paola, N., Holdsworth, R.E., Viti, C., Collettini, C. & **Bullock, R.**, (2015). Can grain size sensitive flow lubricate faults during the initial stages of earthquake propagation? *Earth and Planetary Science Letters* 431, 48–58.

Fredrich, J.T., Evans, B., & **Wong, T.-F.**, (1989). Micromechanics of the brittle to plastic transition in Carrara marble. *Journal of Geophysical Research* 94, 4129–4145.

Govoni, A., Marchetti, A., De Gori, P., Di Bona, M., Lucente, F.P., Improta, L., Chiarabba, C., Nardi, A., Margheriti, L., Agostinetti, N.P., Di Giovambattista, R., Latorre, D., Anselmi, M., Ciaccio, M.G., Moretti, M., Castellano, C., & **Piccinini, D.** (2014). The 2012 Emilia seismic sequence (Northern Italy): Imaging the thrust fault system by accurate aftershock location. *Tectonophysics* 622, 44–55.

Gratier, JP & **Gamond, JF** (1990). Transition between seismic and aseismic deformation in the upper crust. *Geological Society, London, Special Publications* 54, 461–473.

Gratier, J. P., Dysthe, D.K., & **Renard, F.,** (2013). The Role of Pressure Solution Creep in the Ductility of the Earth's Upper Crust, Advances in Geophysics, *Advances in Geophysics*. Elsevier.

Kennedy, L. & **Logan, J.,** (1998). Microstructures of cataclasites in a limestone-on-shale thrust fault: implications for low-temperature recrystallization of calcite. *Tectonophysics* 295, 167–186.

Koopman, A, (1983). Detachment tectonics in the central Apennines, Italy.

Logan, J.M., Dengo, C.A., Higgs, N.G., & **Wang, Z.Z.,** (1992). Fabrics of Experimental Fault Zones: Their Development and Relationship to Mechanical Behavior, *International Geophysics* 51, 33-67

Logan, J.M., Friedman, M., Higgs, C., Dengo, C., & **Shimamoto, T.**, (1979). Experimental studies of simulated gouge and their application to studies of natural fault zones, in: *Proc. 8th Conf. on Analysis of Actual Fault Zones in Bedrock*, pp. 305–343.

Lucente, F., De Gori, P., Margheriti, L., Piccinini, D., Di Bona, M., Chiarabba, C., & **Piana Agostinetti, N.**, (2010). Temporal variation of seismic velocity and anisotropy before the 2009 MW6.3 L'Aquila earthquake, Italy. *Geology* 38, 1015–1018.

Miller, S.A., Collettini, C., Chiaraluce, L., Cocco, M., Barchi, M.R., & **Kaus, B.J.P.** (2004). Aftershocks driven by a high-pressure CO2 source at depth. *Nature* 427, 724–727.

Mirabella, F., Barchi, M.R., Lupattelli, A., Stucchi, E., & **Ciaccio, M.G**. (2008). Insights on the seismogenic layer thickness from the upper crust structure of the Umbria-Marche Apennines (central Italy). *Tectonics* 27.

Paterson, M.S., (1958). Experimental deformation and faulting in Wombeyan Marble. *Geological Society of America Bulletin* 69, 465-476.

Pizzi, A., Di Domenica, A., Gallovič, F., Luzi, L., & Puglia, R. (2017). Fault Segmentation as Constraint to the Occurrence of the Main Shocks of the 2016 Central Italy Seismic Sequence. *Tectonics* 84, 6140.

Ramsay, J., (1967). Folding and fracturing of rocks.

Rutter, E.H., (1986). On the nomenclature of mode of failure transitions in rocks. *Tectonophysics* 122, 381–387.

Rutter, E.H., (1983). Pressure solution in nature, theory and experiment. *Journal of the Geological Society* 140, 725–740.

Sagy, A., Tesei, T., & **Collettini, C.**, (2017). Fault-surface geometry controlled by faulting mechanisms: Experimental observations in limestone faults. *Geology* 45, 851–854.

Scott, D.R., Marone, C.J., & **Sammis, C.G.** (1994). The apparent friction of granular fault gouge in sheared layers. *Journal of Geophysical Research* 99, 7231.

Scuderi, M.M., Collettini, C., & **Marone, C.** (2017). Frictional stability and earthquake triggering during fluid pressure stimulation of an experimental fault. *Earth and Planetary Science Letters* 477, 84–96.

Sibson, R.H., (1977). Fault rocks and fault mechanisms. *Journal of the Geological Society* 133, 191–213.

Siman-Tov, S., Aharonov, E., Sagy, A., & **Emmanuel, S.**, (2013). Nanograins form carbonate fault mirrors. *Geology* 41, 703–706.

Smith, S.A.F., Billi, A., Di Toro, G., & **Spiess, R.**, (2011). Principal Slip Zones in Limestone: Microstructural Characterization and Implications for the Seismic Cycle (Tre Monti Fault, Central Apennines, Italy). Pure and Applied Geophysics 168, 2365–2393.

Storti, F., Billi, A., & **Salvini, F.** (2003). Particle size distributions in natural carbonate fault rocks: insights for non-self-similar cataclasis. *Earth and Planetary Science Letters* 206, 173–186.

Tesei, T., Carpenter, B.M., Giorgetti, C., Scuderi, M.M., Sagy, A., Scarlato, P., & **Collettini, C.** (2017). Friction and scale-dependent deformation processes of large experimental carbonate faults. *Journal of Structural Geology* 100, 12–23.

Tesei, T., Collettini, C., Barchi, M.R., Carpenter, B.M., & **Di Stefano, G.** (2014). Heterogeneous strength and fault zone complexity of carbonate-bearing thrusts with possible implications for seismicity. *Earth and Planetary Science Letters* 408, 307–318.

Tesei, T., Collettini, C., Viti, C., & **Barchi, M.R.** (2013). Fault architecture and deformation mechanisms in exhumed analogues of seismogenic carbonate-bearing thrusts. *Journal of Structural Geology* 55, 167–181.

Valoroso, L., Chiaraluce, L., & **Collettini, C.** (2014). Earthquakes and fault zone structure. *Geology* 42, 343–346.

Ventura, G., & **Di Giovambattista, R.** (2012). Fluid pressure, stress field and propagation style of coalescing thrusts from the analysis of the 20 May 2012 ML5.9 Emilia earthquake (Northern Apennines, Italy). *Terra Nova* 25, 72–78.

Verberne, B.A., He, C., & **Spiers, C.J.** (2010). Frictional Properties of Sedimentary Rocks and Natural Fault Gouge from the Longmen Shan Fault Zone, Sichuan, China. *Bulletin of the Seismological Society of America* 100, 2767–2790.

Verberne, B.A., Niemeijer, A.R., de Bresser, J.H.P., & **Spiers, C.J.** (2015). Mechanical behavior and microstructure of simulated calcite fault gouge sheared at 20-600°C: Implications for natural faults in limestones. *J. Geophys. Res.* 120, 8169–8196.

Verberne, B.A., Spiers, C.J., Niemeijer, A.R., De Bresser, J.H.P., De Winter, D.A.M., & **Plümper, O.** (2014). Frictional Properties and Microstructure of Calcite-Rich Fault Gouges Sheared at Sub-Seismic Sliding Velocities. *Pure and Applied Geophysics* 171, 2617–2640.

Viti, C., Collettini, C., & **Tesei, T.** (2014). Pressure solution seams in carbonatic fault rocks: mineralogy, micro/nanostructures and deformation mechanism *Contributions to Mineralogy and Petrology* 167.

Wells, R.K., Newman, J., & **Wojtal, S.** (2014). Microstructures and rheology of a calcite-shale thrust fault. *Journal of Structural Geology* 65, 69 – 81.

3. Complex geometry and kinematics of subsidiary faults within a carbonate-hosted relay ramp

Marco Mercuri[1], Kenneth J. W. McCaffrey[2], Luca Smeraglia[1,3], Paolo Mazzanti[1,4], Cristiano Collettini[1], and Eugenio Carminati[1]

1: Dipartimento di Scienze della Terra, Sapienza Università di Roma, P.le Aldo Moro 5, 00185 Roma, Italy
2: Earth Sciences Department, Durham University, South Road, Durham, DH1 3LE, UK
3: Laboratoire Chrono-Environnement, Université de Bourgogne Franche-Comté, Besançon, France
4: NHAZCA S.r.l., spin-off company University of Rome "Sapienza", Via Vittorio Bachelet 12, 00185 Rome, Italy

Published in *Journal of Structural Geology* 130 (2020), 103915

ABSTRACT

Minor fault geometry and kinematics within relay ramps is strongly related to the stress field perturbations that can be produced when two major fault segments overlap and interact. Here we integrate classical fieldwork and interpretation of a virtual outcrop to investigate the geometry and kinematics of subsidiary faults within a relay ramp along the Tre Monti normal fault in the Central Apennines. Although the Tre Monti fault strikes parallel to the regional extension (NE-SW) it shows predominant dip-slip kinematics, suggesting a NW-SE oriented extension acting at sub-regional scale (1-10 km). Conversely, the slickenlines collected on the front segment of the relay ramp highlight right-lateral kinematics. The subsidiary faults in the relay ramp show a complex geometry (variable attitudes) and slickenlines describe multiple kinematics (left-lateral, dip-slip, right-lateral), independently of their orientation. Our fault slip analysis indicates that a local stress field retrieved from the kinematic inversion of the slickenlines collected on the front segment, and likely promoted by the interaction between the overlapping fault segments that bound the relay zone, can explain most of the geometry and kinematics of the subsidiary faults. Further complexity is added by the temporal interaction with both the regional and sub-regional stress fields.

3.1. INTRODUCTION

Relay ramps transfer displacement between two overlapping fault segments and are common in extensional tectonic regimes (e.g., Larsen, 1988, Peacock and Sanderson, 1991, 1994). They form in response to the mechanical interaction between the overlapping faults causing the tilting of beds, producing strong damage and, eventually, the linkage between the fault segments (Peacock and Sanderson, 1994; Fossen and Rotevatn, 2016 and references therein). Relay ramps (and interaction damage zones in general; e.g., Peacock et al., 2017) are characterized by stronger damage and by subsidiary faults and fractures having a wider range of orientations than isolated fault segments (Kattenhorn et al., 2000; Peacock et al., 2000; Peacock and Parfitt, 2002; Fossen et al., 2005; Çiftci and Bozkurt, 2007; Bastesen and Rotevatn, 2012; Long and Imber, 2012). The strong damage and the structural complexity in zones of fault interaction can have important consequences on fluid flow, leading to enhanced permeability (e.g., Berkowitz, 1995) and to a multi-directional migration of fluids, including hydrocarbons, CO_2, ground water, and hydrothermal fluids (Sibson, 1996; Curewitz and Karson, 1997; Rowland and Sibson, 2004; Rotevatn et al., 2009; Dockrill and Shipton, 2010; Fossen and Rotevatn, 2016). Since about the half of the current hydrocarbon reserves are held within carbonates, carbonate-hosted relay ramps represent a very interesting case study.

The variability in subsidiary structural orientations, including joints and normal faults striking orthogonally to the main fault segments (e.g., Kattenhorn et al., 2000; Ciftci and Bozkurt, 2007), can be very important for cross-fault fluid migration, increasing the chance of some fractures and faults being optimally oriented to open and/or slip under various stress fields (Fossen and Rotevatn, 2006). The presence of variably oriented faults and fractures is commonly attributed to local stress field perturbations due to the interaction and progressive linkage between the fault segments that border the relay ramp, or to the development of the relay ramp itself (Crider and Pollard, 1998; Kattenhorn et al., 2000; Bastesen and Rotevatn, 2012). The existence of various controlling factors (e.g., the displacement profiles, relative orientations, and growth rates of the interacting faults; Fossen and Rotevatn, 2016), makes it difficult to constrain the local stress field within a relay ramp. Although attempts have been made to model the stress field within a relay ramp (e.g., Crider and Pollard, 1998) its better characterization through field observations conducted on exhumed faults can help predicting faults and fractures orientations, with important consequences to the assessment of fluid flow within fault zones.

In the present work, we combined traditional fieldwork and virtual outcrop interpretation (Bellian et al., 2005; McCaffrey et al., 2005a,b; Hodgetts, 2013) to investigate the geometry and kinematics of the subsidiary faults within a portion of a carbonate-hosted relay ramp pertaining to the Tre Monti fault, a normal fault in the Central Apennines of Italy. The fault slip analysis shows that a local stress field retrieved from the kinematic inversion of the slickenlines locally observed on the front segment of the relay ramp is able to explain most, but not all, of the complex geometry and kinematics of the subsidiary faults. Transient effects of regional and sub-regional stress fields acting on the relay ramp structure may explain this complexity.

GEOLOGICAL SETTING

The central Apennines are a late-Oligocene to present fold-and-thrust belt that formed in response to the westward directed subduction of the Adria plate under the European plate (Doglioni, 1991). This produced a north-eastward migrating and NE-SW directed shortening which was accommodated by thrusts (Fig. 3.1a). The thrusts affected the sedimentary sequence of Adria, including a late-Triassic to middle Miocene thick carbonate succession (Cosentino et al., 2010 and references therein), and, according to some interpretations, also the underlying continental basement (Patacca et al., 2008). In the study area (Fucino basin) the thrusting events occurred from late Miocene to early Pliocene (Cavinato and De Celles, 1999) whilst the presently active compressive front is located ~ 60 km towards the NE.

Since the early Pliocene, extensional tectonics have affected the central Apennines in response to the opening of the Tyrrhenian back-arc basin (Doglioni, 1991) and, as testified by stress maps (Montone et al., 2004; Heidbach et al., 2016), GPS measurements (D’Agostino et al., 2001; Devoti et al., 2010), and focal mechanisms of earthquakes (Scognamiglio et al., 2010; Chiaraluce, 2012; Chiaraluce et al., 2017), is still ongoing. In particular, NE-SW oriented extension and uplift is accommodated by extensional faults, which dismember the shallow-water to pelagic carbonate succession that constitutes the backbone of the Central Apennines, generating several intermontane basins (Fig. 3.1a; e.g., Fucino, Sulmona, L’Aquila, Campo Imperatore) (Cosentino et al., 2010). The extensional faults bordering the intermontane basins mostly strike NW-SE, although rare SW-NE trending fault, such as the Tre Monti fault, are present (Fig. 3.1a). In this tectonic framework, the Tre Monti extensional fault marks the north-western boundary of the Fucino Basin and crops out for ~ 7 km through a series of right-stepping SE-dipping fault scarps (Fig. 3.2a).

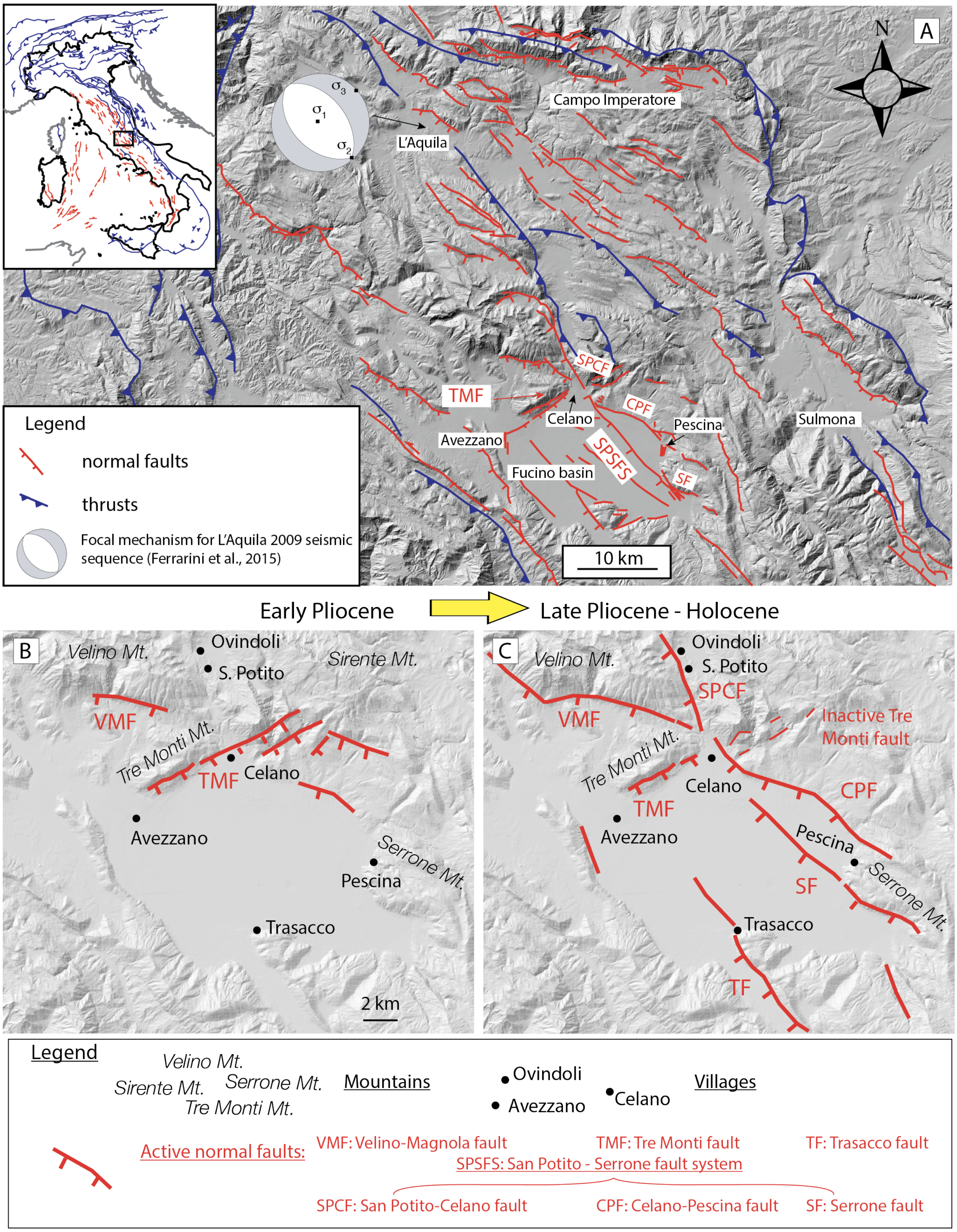

Figure 3.1 (previous page)- Structural setting of the Central Apennnines (A) and Plio-Quaternary tectonic evolution of the Fucino basin (B, C). The intermontane basins in the Central Apennines are commonly bordered by NW-SE and rarer WSW-ENE striking normal faults (red). Slip on normal faults accommodates a NE-SW oriented regional extension which started during late Miocene/early Pliocene and it is still ongoing, as testified by the stress field retrieved from recent seismic sequences (e.g., L'Aquila 2009; Scognamiglio et al., 2010; Ferrarini et al., 2015). The normal faults dismember a late Triassic to Miocene shallow-water to pelagic- carbonate succession shortened within the Apennines fold and thrusts belt. The Fucino Plain is an intermontane basin bordered by the Tre Monti fault (TMF) to NW and by the San Potito-Serrone fault system (SPSFS) to the NE. The San Potito – Serrone fault system comprises the San Potito-Celano (SPCF), Celano-Pescina (CPF), and Serrone (SF) faults. The tectonic evolution of the Fucino plain during early Pliocene time was controlled by dip-slip movements on the Tre Monti fault, which was longer at the time (B). Since Late Pliocene, the Fucino plain tectonics was controlled by NW-SE striking San Potito-Serrone fault system cutting the Tre Monti fault near the Celano village (C). Modified from Galadini and Messina (1994).

The reconstruction of Pliocene-Quaternary tectonic structures of the Fucino basin (Galadini and Messina, 1994, 2001; Cavinato et al., 2002; Gori et al., 2017) is based on the increasing thickness of Pliocene deposits towards the northern sector of the basin (Cavinato et al., 2002). The tectonic evolution of the Fucino basin during early Pliocene time was initially controlled by dip-slip movements along the Tre Monti fault, which was longer at the time (Fig. 3.1b), with the consequent formation of a NE-SW elongated semi-graben. Since Late Pliocene, the Fucino basin tectonics was controlled by NW-SE striking faults that border the Fucino basin to the NE (Cavinato et al., 2002), which cut and displaced the Tre Monti fault near the Celano village (Fig. 3.1c).

The main fault scarps of the Tre Monti fault juxtapose Pliocene to Holocene continental deposits in the hangingwall and early Cretaceous to middle Miocene shallow water carbonates in the footwall (Fig. 3.2a, b). Interpreted seismic reflection profiles (Cavinato et al., 2002; Smeraglia et al., 2016) show that the throw increases from ~800 m up to ~ 2,000 m moving from SW to NE. The exposed portion of the Tre Monti fault was exhumed from depth < 3 km (Smeraglia et al., 2016). The slickenlines on the fault scarps indicate mainly dip-slip kinematics, although rare right-lateral movements are locally recorded (Morewood and Roberts, 2000; Smeraglia et al., 2016). The Linked Bingham fault plane solution for these kinematic indicators indicate NW-SE oriented tension (Fig. 3.2a), i.e., orthogonal to regional NE-SW extension. Paleoseismological investigations with cosmogenic ^{36}Cl measurements on fault scarps (Benedetti et al., 2013; Cowie et al., 2017) suggest that the Tre Monti fault has been active between Early Pliocene and recent times with dip-slip kinematics. The occurrence of predominantly dip-slip movements on a fault striking nearly parallel to the regional extension vector has been explained by invoking a release fault geometry for the Tre Monti fault (Destro, 1995; Galadini and Messina, 2001). In this scenario the Tre Monti fault accommodates a differential throw along the strike of the

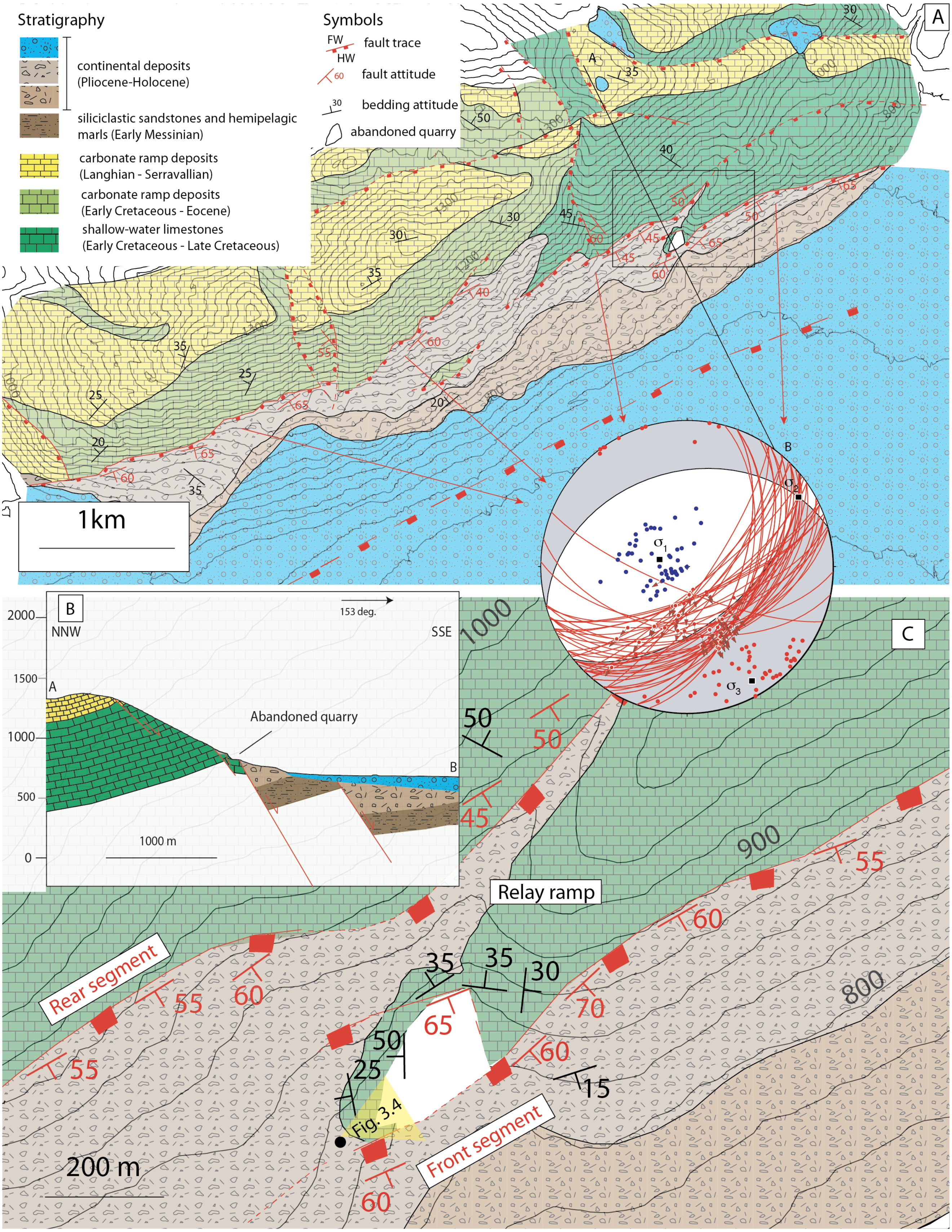

Figure 3.2 (previous page) - The Tre Monti fault. (A) Geological map of the Tre Monti area (modified from Smeraglia et al., 2016). The Tre Monti fault is ~7 km long and crops out in a series of SE-dipping and right-stepping fault scarps. Mainly dip-slip kinematic indicators were observed on the main fault scarps, suggesting NW-SE oriented extensional stress field (stereoplot in Figure 2a). Blue and red dots in the stereoplot represent respectively the orientation of σ_1 and σ_3 inferred from the inversion of each slickenline. (B) Geological cross-section (section trace indicated in Figure 2a) showing that the Tre Monti fault is composed of a series of sub-parallel fault strands. The principal fault strand represents the tectonic contact between early Cretaceous to Miocene carbonates (footwall) and Pliocene to Quaternary deposits (hangingwall). (C) Zoom of the study-area marked with a black square in Figure 2a. The abandoned quarry is located at the footwall of the front segment in a relay ramp environment defined by two main right-stepping fault strands and exposes the damage zone within Early Cretaceous shallow-water limestones. The small black circle in Figure 2c represents the view point for Figure 3.4.

NW-SE striking fault system that borders the Fucino basin to the NE and comprises the San Potito-Celano, Celano-Pescina, and Serrone faults (hereafter the San Potito–Serrone fault system, SPSFS; see Fig. 3.1a,c). Finally, microstructural analyses performed on the fault core suggest that the TMF experienced past earthquakes. This is testified by some seismic slip indicators found in the fault core: fluidized ultracataclasite layers, injection veins, and decomposed calcite crystals (Smith et al., 2011; Smeraglia et al., 2016, 2017).

In this work we focus on a key outcrop, represented by an abandoned quarry (the “La Forchetta” quarry in Smeraglia et al., 2016), located ~ 2 km WSW of Celano (42°04’35”N 13°30’00”E; Fig. 3.2).

3.3. Methods

We combine traditional fieldwork with the interpretation of a virtual outcrop to investigate minor faults within the damage zone of the study area. Using traditional fieldwork methods, we have (1) collected orientation data from the subsidiary faults to provide control on the virtual outcrop fault data and, (2) collected slickenline data to enable a kinematic analysis.

3.3.1. Virtual outcrop acquisition

The virtual outcrop consists of a high-resolution point cloud that has been collected through a terrestrial laser scanner (TLS) survey (Fig. 3.3).

To build the point cloud, the TLS records the time-of-flight of a series of laser pulses reflected by the outcrop surface (thousands of measurements per second). The TLS calculates the distance between the sensor and the outcrop knowing the velocity of the light. Knowing the exact position (absolute geographic coordinates) of some ground control points (GCP) in the scene, all distance measurements relative to the TLS instrument are then converted to a point cloud, where each point is identified by X, Y, Z values representing its geographic coordinates. The integration of the laser scanner device with images from a calibrated high-resolution camera (Fig. 3.3)

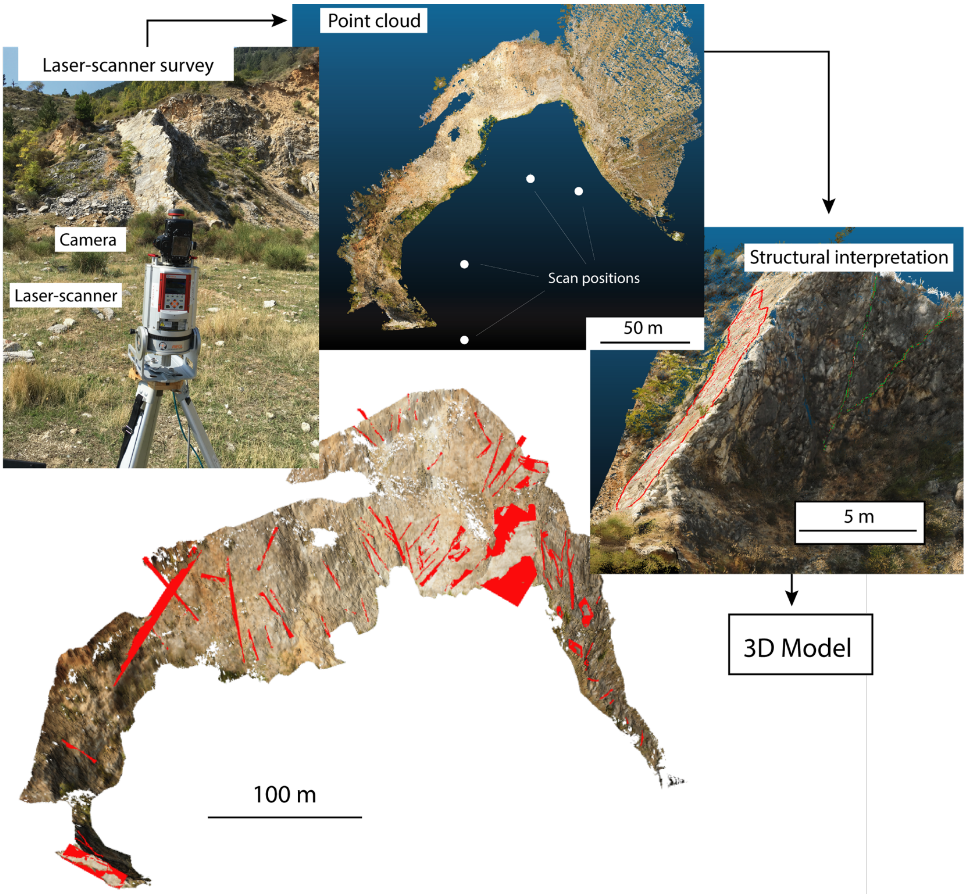

Figure 3.3 - Summary of the adopted methodology to build a 3D model representing the minor fault distribution in the abandoned quarry. A laser-scanner survey has been performed to produce a true-color point cloud. Using the CloudCompare software (www.cloudcompare.org), the minor faults were identified in the point cloud and manually picked to obtain a structural interpretation. Finally, we built a 3D model using the Move software.

enables true colours to be added to the scene. Consequently, RGB values are assigned to each point (White and Jones, 2008) to obtain a georeferenced and true-colour point cloud (Fig. 3.3). The reader is referred to the papers of Buckley et al., (2008) and Telling et al., (2017) for an extensive review of the terrestrial laser scanner methodology and its application in geology.

For this study we collected high-resolution point clouds from 4 different scan positions using a Riegl VZ1000 instrument (Fig. 3.3). During the point cloud acquisition, we used 7 ground control points (GCP) with known absolute coordinates. The absolute coordinates of the GCPs were obtained through a differential GPS survey performed using a Leica GX1230 GPS receiver. The point clouds were georeferenced and combined to obtain a single point cloud covering the whole quarry. The final result is a high-resolution (~ 100 million points) true-colour point cloud (Fig. 3.3).

3.3.2. Minor faults mapping on the virtual outcrop

Starting from a 3D model (Fig. 3.3), we constructed a map and a cross section illustrating the minor faults distribution in the quarry. We built the 3D model using the Move™ software, combining a topographic model of the abandoned quarry with a structural interpretation representing the minor faults distribution. Both the topographic model and the structural interpretations were extracted from the point cloud using the CloudCompare software (www.cloudcompare.org).

The topographic model is made of a Digital Terrain Model combined with an orthophoto of the abandoned quarry. Both have been extracted by converting the point cloud to raster files containing the elevation and RGB values with a grid resolution of 0.5 m steps. The two raster files have been subsequently merged using the Move software.

The structural interpretation was produced by manual picking all visible minor faults in the quarry using the Compass plugin in CloudCompare (Thiele et al., 2017). For each minor fault we have drawn a polyline representing its trace in the quarry topography and, eventually, a zig-zag polyline to include as much of the visible minor fault surfaces as possible (Fig. 3.3), as described in Pless et al., (2015). In order to produce a polygon and to obtain the attitude of minor faults, all the polylines pertaining to each fault have been fitted with planes using the Compass plugin (Thiele et al., 2017). The goodness of fit was evaluated by analysing the Root Mean Square (RMS) value provided by the plugin (Figs. A2 and A3). We finally built a 3D model of the quarry (Fig. 3.3) exporting the structural interpretation from CloudCompare and merging it with the topographic model using the Move software (Fig. 3.3).

The minor faults map was produced by combining the topographic model with the polylines representing fault traces and with point data representing fault attitudes. To produce the cross section, we used the Move™ software to project each fault polygon orthogonally to a vertical section oriented parallel to the main fault dip (156°) regardless of the orientation of the fault planes.

3.3.3. Fault slip analysis

We conducted a fault slip analysis on a dataset of 100 minor fault collected in the field. For each minor fault we collected the attitude of the slip surface (strike, dip, dip azimuth) and the slickenlines orientation (trend, plunge, rake). In detail, we evaluated the geometrical and kinematic compatibility of all the minor faults with different hypothetical stress fields.

The geometrical compatibility has been evaluated calculating the normalised slip tendency (Morris et al., 1996; Lisle and Srivastava, 2004; Collettini and Trippetta, 2007; Di Domenica et al., 2014) for each minor fault in a given stress field. The slip tendency (T_s) measures the potential for slip on a weakness plane subjected to a known stress field and is given by (Morris et al., 1996):

$$T_S = \frac{\tau}{\sigma'_n} \qquad (3.1),$$

where τ and σ_n' are respectively the resolved shear and effective normal stress ($\sigma_n' = \sigma_n - P_f$, where P_f is the pore fluid pressure) on the fault. According to the Amontons' law for fault reactivation ($\tau = \mu \cdot \sigma_n'$), the condition for slip on a fault is:

$$T_S = \frac{\tau}{\sigma'_n} > \mu_S \qquad (3.2),$$

where μ_s represents the coefficient of sliding friction. The resolved shear and effective normal stresses on a fault depend on (1) its orientation in the principal stresses reference frame, (2) on the differential stress ($\sigma_1 - \sigma_3$), (3) on the pore fluid pressure, and (4) on the stress shape ratio $\phi = \frac{(\sigma_2-\sigma_3)}{(\sigma_1-\sigma_3)}$. However, within a crustal volume, the differential stress and the pore fluid pressure are often not well-constrained. We can overcome this problem by assuming that the maximum slip tendency value is reached when the frictional sliding envelope given by the Amontons' law is tangential to the $\sigma_1\sigma_3$ Mohr's circle in a τ-σ_n space. By such an assumption we are able to evaluate the slip tendency in a mechanical system that depends only on the orientation of the fault within the principal stresses reference frame, on the coefficient of friction, and on the stress shape ratio. We assumed a 0.6 friction coefficient, typical of carbonates (Tesei et al., 2014; Carpenter et al., 2016) and a stress shape ratio of 0.56 (Ferrarini et al., 2015). We refer the reader to the papers by Lisle and Srivastava, (2004) and Collettini and Trippetta (2007) for the complete procedure. In the tangential condition assumption, we evaluate the slip potential of a fault through the normalised slip tendency (Lisle and Srivastava, 2004):

$$NT_S = \frac{T_S}{T_S^{max}} \quad (3.3),$$

Each fault can have $0 \leq NT_S \leq 1$. We define a fault well-oriented if $0.5 \leq NT_S \leq 1$, and misoriented if $0 \leq NT_S < 0.5$.

Although the normalised slip tendency method enables us to establish whether a fault is prone to slip in a given stress field, it does not predict its kinematics in that stress field. Assuming that slip on a fault occurs along the direction of the resolved shear stress (Wallace, 1951; Bott, 1959), we can evaluate the compatibility of the measured slickenlines within a given stress field. Hence, we calculated the predicted slickenlines orientations for the well-

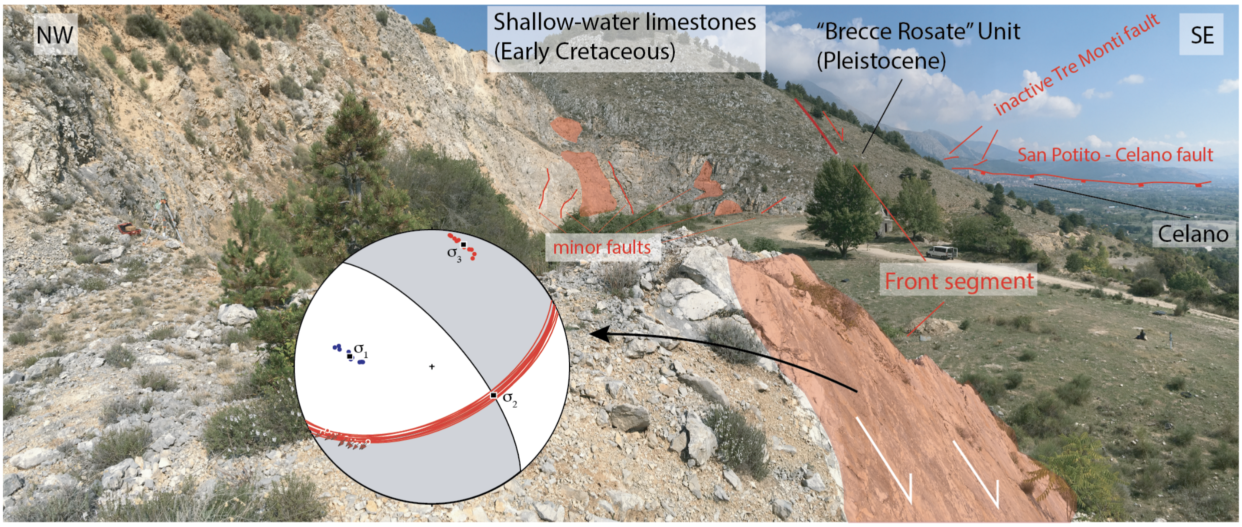

Figure 3.4 - View of the abandoned quarry from the point indicated in Figure 2c. The main fault (front segment of the relay ramp) crops out in the western portion of the quarry where it puts in contact the Early Cretaceous shallow-water limestones in the footwall, with Pleistocene continental breccias ("Brecce Rosate" Unit; Cavinato et al., 2002) in the hangingwall. The damage zone is located in Early Cretaceous shallow-water limestones and characterized by pervasive fracturing and the presence of minor faults. The fault is characterized by right-lateral kinematic indicators providing the stress field reported in the stereoplot (Schmidt net lower hemisphere). Blue and red dots in the stereoplot represent respectively the calculated σ_1 and σ_3 orientation for each slickenline.

oriented minor faults within the stress field using the software FaultKin (Marrett and Allmendinger, 1990; Allmendinger et al., 2011). Consequently, we calculated the difference (ΔR) between the observed (R_{obs}) and the predicted rake (R_{pred}) of the slickenlines on the well-oriented minor faults:

$$\Delta R = |R_{obs} - R_{pred}| \qquad (3.4),$$

We divided the extensional rake values, going from 0° for left-lateral kinematics to 180° for right-lateral kinematics, into 5 fields with amplitude of 36°. For this reason, we decided to classify the slickenlines as compatible with a certain stress field if $\Delta R \leq 36°$.

3.4. Results

3.4.1. Geometry of the minor faults

The study outcrop is located in the overlap zone between two right stepping segments of the main fault, defining a relay ramp environment (Fig. 3.2c). The distance between the front and the rear segment (sensu Crider and Pollard, 1998) of the relay ramp is ~ 400 m in map view, whilst the two segments overlap for at least 900 m along strike (Fig. 3.2c). The quarry is located immediately at the footwall and at the western tip of the front segment (Fig. 3.2c). The front segment dips moderately toward SE (156° mean dip azimuth) and puts Lower Cretaceous shallow-water limestones at the footwall in contact with Middle Pleistocene subaerial breccias ("Brecce Rosate" Unit; Cavinato et al., 2002) at the hangingwall (Fig. 3.2c and 3.4). The slickenlines, well-preserved in the western portion of the quarry (Fig. 3.4), suggest oblique to right-lateral (mean slickenlines rake 155°) kinematics for the front segment. Such kinematics are compatible with a non-Andersonian stress field characterized by oblique σ_1 and NNE gently plunging σ_3 (Fig. 3.4). The Lower Cretaceous limestones in the quarry host the fault damage zone, characterized by pervasive fracturing and the presence of various small-displacement (metric to decametric) slip surfaces (i.e., minor faults; Fig. 3.4).

The manual interpretation of the quarry virtual outcrop allowed us to map the minor faults in the damage zone (Fig. 3.5). Minor faults are pervasive and heterogeneously distributed, with the highest concentration in the northern sector (Fig. 3.5). Their trace length, measured from the DOM, spans from 1 m to 50 m with most of the values comprised between 5 m and 10 m (Fig. A1). The density contour stereoplot representing the poles to the minor faults attitudes measured in the field (stereoplot on the left in Fig. 3.5) is very similar to that obtained from the virtual outcrop (stereoplot on the right in Fig. 3.5). Both the stereoplots show evidence for two major sets of minor faults. The first set is characterized by orientations similar to the main fault, specifically faults dipping > 55° and striking both E-W and NE-SW (stereoplots in Fig. 3.5). The most prominent example is provided by a very large (~20 m x 25 m) and undulated fault surface exposed in the northern sector of the quarry (Figs. 3.5 and 3.6a). The second set is characterized by slip surfaces striking NW-SE (i.e., orthogonal to the main fault) and dipping > 60° (stereoplot in Fig. 3.5). This set is particularly evident in the eastern sector of the quarry (Fig. 3.6b). Notably, our observations did not provide any evidence of systematic cross-cutting relationship between the different sets of faults (Fig. 3.5).

A cross-section across the quarry allows us to visualize the minor faults distribution, and hence to illuminate the fault zone structure at the outcrop scale (Fig. 3.6c). The largest minor faults pertaining to the first set (Figs. 3.5 and 3.6c) are arranged with distances varying from 1-2 m to tens of meters (Fig. 3.6c). The second set is represented by a relatively high number of minor faults striking orthogonal to the main fault. Other minor faults show strikes similar the main fault and have low dip angles, and rare antithetic faults are also present (Fig. 3.6c).

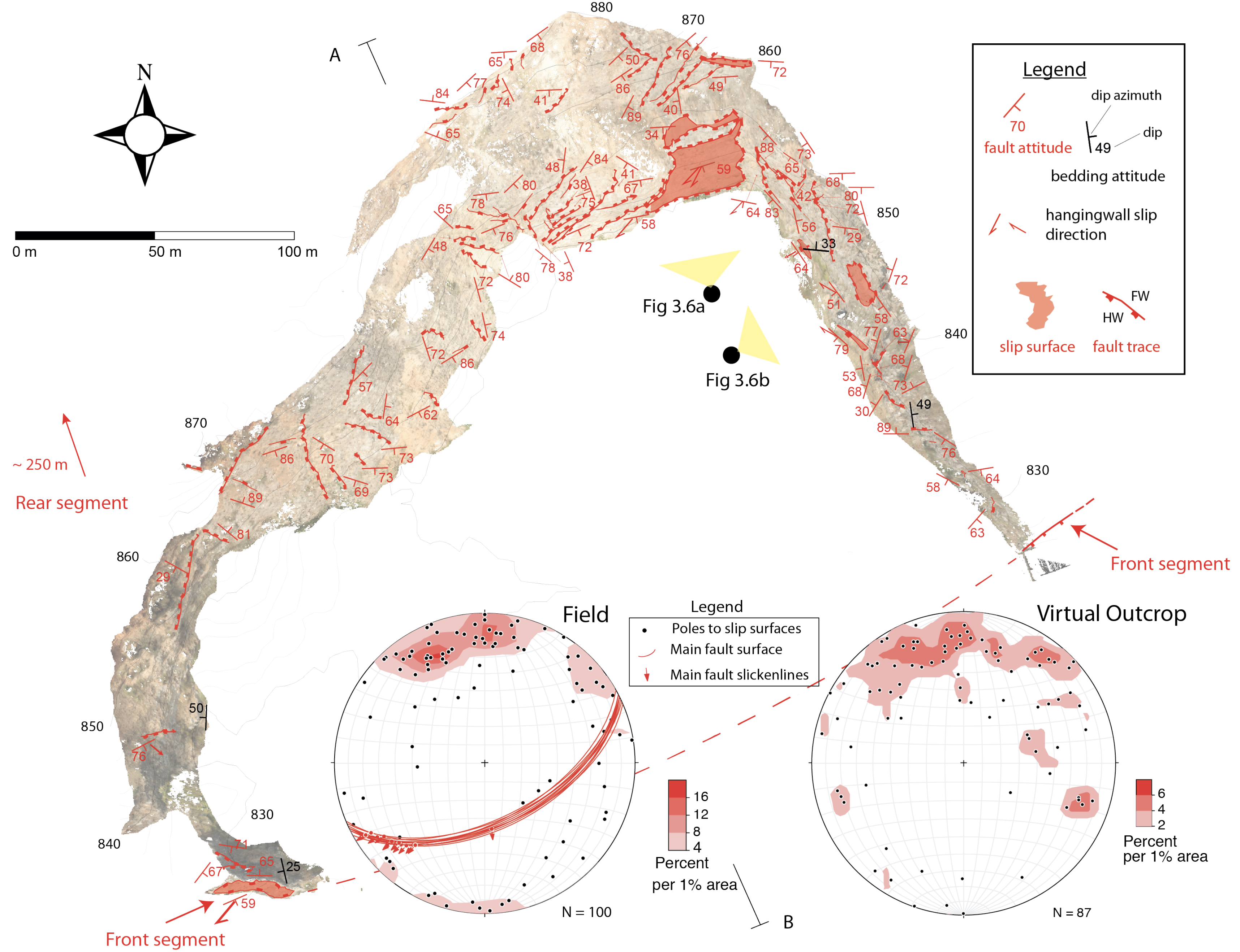

Figure 3.5 - Minor faults map obtained from the manual interpretation of the virtual outcrop. Minor faults are heterogeneously distributed within the damage zone, with the highest concentration in the northern sector of the quarry. The minor faults attitudes obtained from both the real and the virtual outcrop are represented as poles in the two stereoplot (Schmidt net lower hemisphere). The black line (AB) represent the trace of the cross-section reported in Figure 3.6. The black dots with yellow triangles indicate view points for Figure 3.6a and 3.6b.

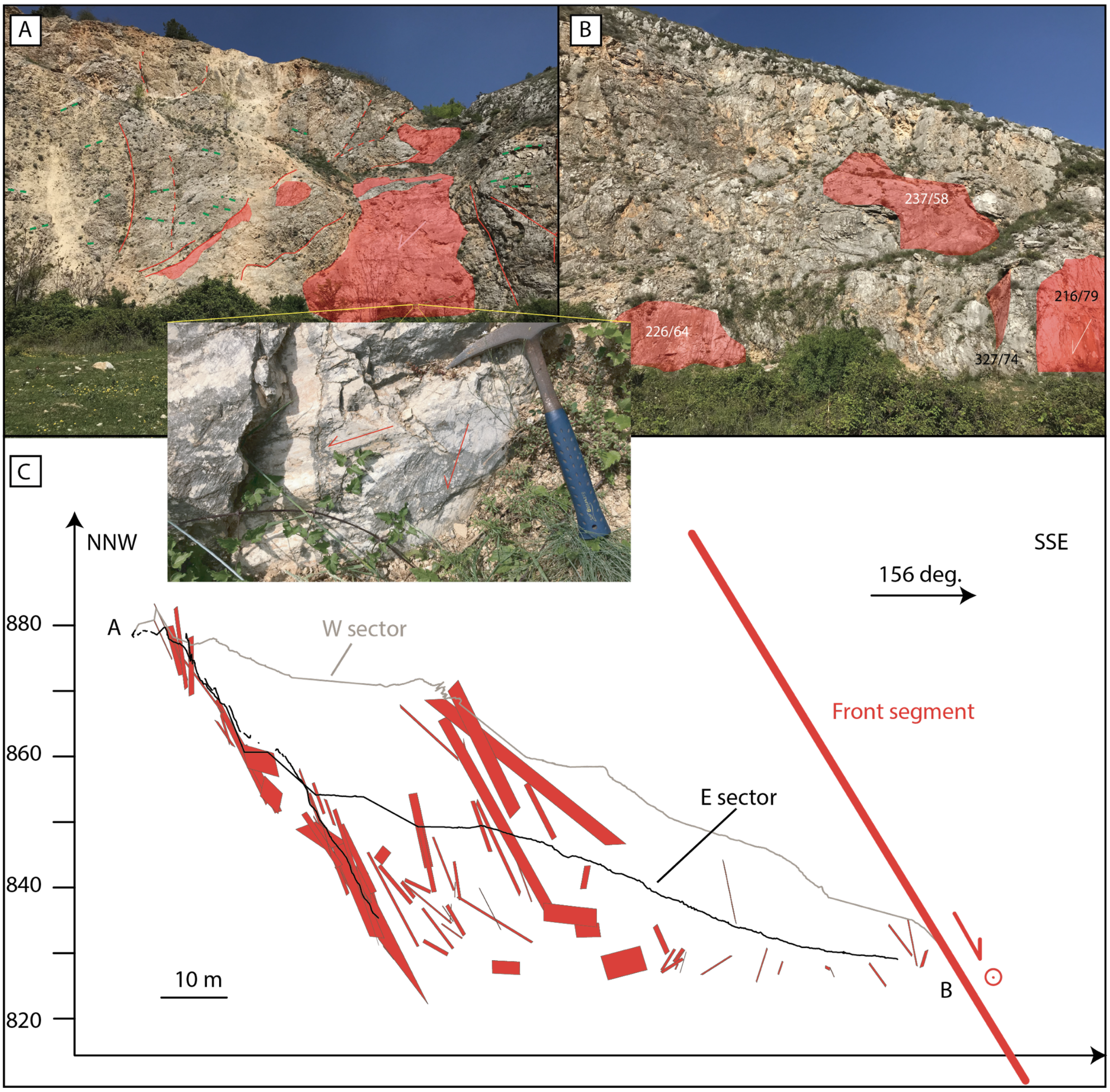

Figure 3.6 - Minor faults in the abandoned quarry. (A) Faults striking subparallel to the main fault are the most abundant and are often characterized by two slickenlines sets (inset). This set is accompanied by smaller faults striking orthogonal to the main fault (B). (C) Vertical cross-section parallel to the main fault dip. The outcrop-scale internal structure for the Tre Monti fault is depicted by the minor fault distribution, characterized by major fault strands sub-parallel to the main fault with smaller faults with different orientation.

3.4.2. Kinematics of the minor faults

The slickenlines collected on the minor faults indicate complex kinematics (Fig. 3.7). The density contour plot in Figure 3.7a shows that slickenlines on minor faults have azimuths in variable directions and plunges that range from horizontal to vertical. However, most of the slickenlines plunge between ~220° (SW) and ~ 320° (NW), with the highest density between 240° and 280° (WSW to W approximately; Fig. 3.7a). In this range we recognize two main clusters (~270°/35° and ~250°/15°) defining W-E oblique and WSW-ENE sub-horizontal movements respectively, and several minor clusters, including NW-SE and WSW-ENE oblique kinematics, and

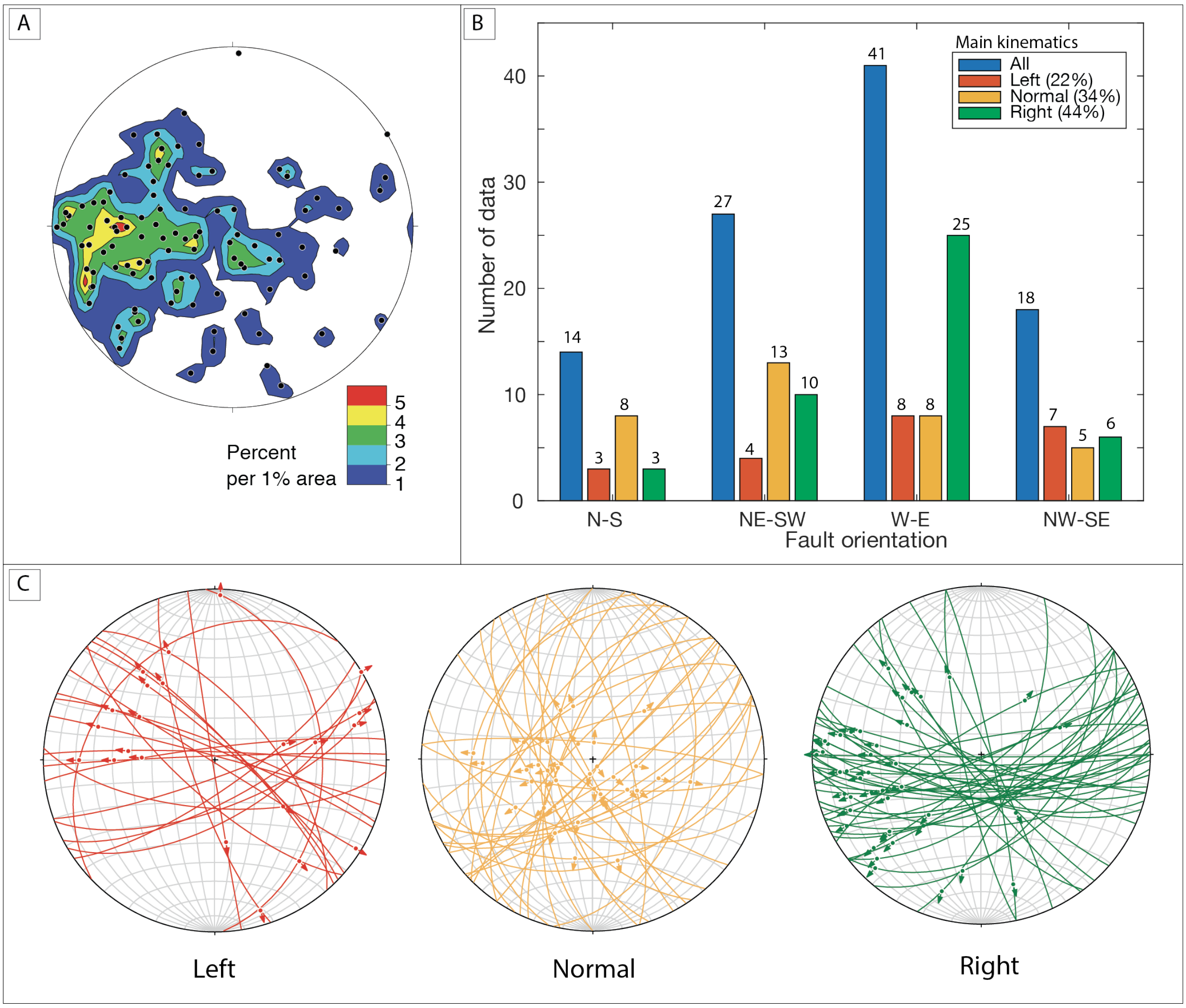

Figure 3.7 - Minor faults kinematics. (A) Density contour plot of slickenlines (Schmidt net, lower emisphere). The slickenlines point toward all directions, with maximum densities toward WSW, W, and NW. (B) Bar charts showing the distribution of fault orientation and kinematics. The faults exhibit various kinematics for each fixed orientation. (C) Stereoplot (Schmidt net, lower emisphere) of minor faults for left (red), normal (orange), and right main slip component.

W-E sub-horizontal movements. Finally, other minor clusters indicate sub-vertical movements with slickenlines pointing mainly toward WSW (~250°), SSE (~165°) and SW (~220°).

This wide range of slickenlines, together with the different orientation of the minor faults, results in variable kinematics, spanning from left lateral, to normal to right-lateral, independently of their orientation (Fig. 3.7b, c). Furthermore, a double set of slickenlines is sometimes observed on NE-SW and E-W striking faults (inset in Fig. 3.6b). Overall, a right-lateral slip component is the most recorded kinematic sense (44 %), followed by normal (34%), and left lateral motions (22%) (Fig. 3.7b). The faults that shows a main right-lateral component mostly strike in a W-E direction (~57%) and, secondarily, in a NE-SW direction (~23%) (Fig. 3.7b, c). The same kinematics is recorded also by faults striking NW-SE (13 %), and N-S (~7 %). Normal and left-lateral kinematics are nearly equally distributed for the various fault orientations (Fig. 3.7b, c). The highest number of faults with normal kinematics strike NE-SW (~ 38%), followed by N-S and W-E striking faults (~24% each) (Fig. 3.7b, c). Finally, left-lateral slip is mainly associated with E-W (36%) and NW-SE striking (32%) faults (Fig. 3.7b, c).

3.5. Discussion

3.5.1. Geometry of the subsidiary faults

Our study leverages the employment of a virtual outcrop to provide a very detailed description of minor faults within a portion of a carbonate-hosted relay ramp. The manual interpretation of the virtual outcrop allowed us to reconstruct the exact position of each minor fault in 3D space and we used this information to produce a map (Fig. 3.5) and a cross-section (Fig. 3.6c) representing their distribution. Furthermore, we were able to extract orientation data by fitting planes to polylines manually drawn on the 3D traces of the minor faults (Fig. 3.5). The low RMS and RMS/length values testify the goodness of fit (Figs. A2 and A3). The similarity between the stereoplots representing the minor fault attitudes retrieved from the natural and the virtual outcrops (Fig. 3.5) is the strongest evidence for the accuracy of the 3D model. Thus, our study further confirms and supports the applicability of analyses derived from virtual outcrops in structural geology problems (Tavani et al., 2014; Seers and Hodgetts, 2016; Vollgger and Cruden, 2016 and Telling et al., 2017 among others) and, in particular, the ability to create a precise 3D geometrical reconstruction at outcrop scales (1:5,000 and higher).

The structural map and the cross section reconstructed in our study (e.g. Fig. 3.5 and 3.6c) allow for a detailed characterization of the subsidiary fault geometries within the relay zone. The largest subsidiary faults are arranged in major sub-parallel strands striking sub-parallel to the main fault segments and are accompanied by smaller faults with various orientations including those that strike orthogonally to the main fault (Fig. 3.6c and stereoplot in Figure 3.5). The presence of subsidiary faults striking sub-parallel to the main fault segments has been observed for carbonate normal faults at different scales (e.g. Jackson and White, 1989; Agosta and Aydin, 2006; Bonson et al., 2007; Collettini et al., 2014 Valoroso et al., 2014; Demurtas et al., 2016; Smeraglia et al., 2016). Similar faults have been observed within relay ramps formed in basement rocks (e.g., Peacock et al., 2000) and been imaged in seismic reflection profiles (Hus et al., 2006). Nonetheless, our work provides one of the first detailed characterizations of the complex fault pattern (e.g. Figs. 3.5-3.6) within a

Stress field name	σ_1 (trend/plunge)	σ_3 (trend/plunge)	Stress shape ratio, ϕ	Friction coefficient, μ
Regional stress field	292/85	048/02	0.56 (Ferrarini et al., 2015)	0.6
Fault stress field	285/74	150/11	0.56 (Ferrarini et al., 2015)	0.6
Quarry stress field	277/39	015/09	0.56 (Ferrarini et al., 2015)	0.6

Table 3.1 – Parameters defining the stress fields assumed for the kinematic analysis of minor fault slickenlines

carbonate-hosted relay ramp. The detailed structural mapping (scale 1: 2,000) and the large number of subsidiary faults collected for this study (Fig. 3.5), allowed us to confirm the geometrical complexity (multiple orientations of subsidiary faults and fractures) that has been observed within relay ramps in a few previous studies (Kattenhorn et al., 2000; Çiftçi & Bozkurt, 2007; Bastesen & Rotevatn, 2012).

3.5.2. Kinematics and Dynamics of subsidiary faults

Associated with the complex geometry, the subsidiary faults in the damage zone also show complex kinematics, ranging from strike-slip (either dextral or sinistral) to dip-slip movements, independently from their orientations (Fig. 3.7b,c), with slickenlines plunging toward a wide range of directions (Fig. 3.7a). These observations suggest that slip on all the subsidiary faults is not related to a single stress field (e.g., Angelier, 1984). To explain this complex fault pattern, the first hypothesis to explore is that the complex geometry and kinematics results from the overprinting of two (or more) stress fields related to different tectonic regimes acting in different periods of time. This hypothesis can be easily ruled out. In fact, although some NE-SW and E-W striking faults record two slickenline sets (Fig. 3.6a), systematic cross-cutting relationships between various sets of minor faults are absent (see Fig. 3.5).

In the following, we test the hypothesis that complex minor fault geometry and kinematics result from the simultaneous activity and competition of at least 3 stress fields (Fig. 3.8) induced by: 1) active extension in Central Apennines (regional stress field); 2) the Tre Monti fault activity (fault stress field) and 3) the relay zone (quarry stress-field). We firstly provide geological and geophysical background for each stress field, and then we describe our fault slip analysis.

The axial zone of the Apennines is characterized by an extensional Andersonian stress field with NE-SW oriented σ_3 (regional stress field; Fig. 3.8a and Table 3.1), as shown by inversion of focal mechanisms (e.g. Chiaraluce et al., 2017). There is strong evidence for the recent activity of the Tre Monti normal fault in the framework of the active extensional fault system of Central Apennines. This is supported by the predominance of dip-slip slickenlines observed on the main fault scarps (stereoplot in Fig. 3.2a) and by paleoseismological investigations showing dip-slip kinematics (Benedetti et al., 2013; Cowie et al., 2017). The kinematic inversion of slickenlines measured along the main fault scarps defines a NW-SE orientated extension with a sub-vertical σ_1 (fault stress field; Fig. 3.8a and Table 3.1). Finally, in a relay zone, it is well documented that slip and stress distribution within the overlapping segments promote the development of a local stress field (Crider and Pollard, 1998; Kattenhorn et al., 2000; Çiftçi & Bozkurt, 2007; Bastesen & Rotevatn, 2012). For our case study we retrieved the local stress field from kinematic inversion of the right-lateral slickenlines observed on the main fault in the quarry (i.e., the front segment of the relay ramp; Fig. 3.4). This stress-field is characterized by a non-Andersionian orientation of the principal stress axes, with a W-trending oblique σ_1 and NNE trending gently dipping σ_3 (quarry stress field; Fig. 3.8c and Table 3.1).

The regional stress field (Fig. 3.8a, Table 3.1) used as input for the fault slip analysis show that 51% of minor faults are well-oriented in this stress field, but only 27% of them present compatible slickenlines (Fig. 3.8a). The regional stress field can only explain the right-lateral kinematics of W-E striking faults and the dip-slip kinematics on NW-SE striking faults (Fig. 3.8a and Table 3.2).

The fault stress field (Fig. 8b, Table 3.1) is able to explain the geometry of a large number of subsidiary faults (72%), however only 15% are well-oriented and have compatible kinematics (Fig. 3.8b). The fault stress field is able to explain only dip-slip slickenlines on NE-SW oriented minor faults (Fig. 3.8b and Table 3.2).

The quarry stress field (Fig. 3.8c and Table 3.1) is able to explain the distribution of a very high percentage of minor faults (81%) and a large number of these faults (53%) have slickenlines compatible with this stress field (Fig. 3.8c). The quarry stress field is able to explain the kinematics of minor faults striking both parallel (right-lateral kinematics on W-E and NE-SW striking faults) and orthogonal to the main fault (left-lateral kinematics on NW-SE striking faults) (Fig. 3.8c and Table 3.2).

Within a relay ramp, complex fault geometries are often associated with mechanical interaction and stress rotation between the overlapping faults (Peacock & Sanderson, 1994; Fossen and Rotevatn,

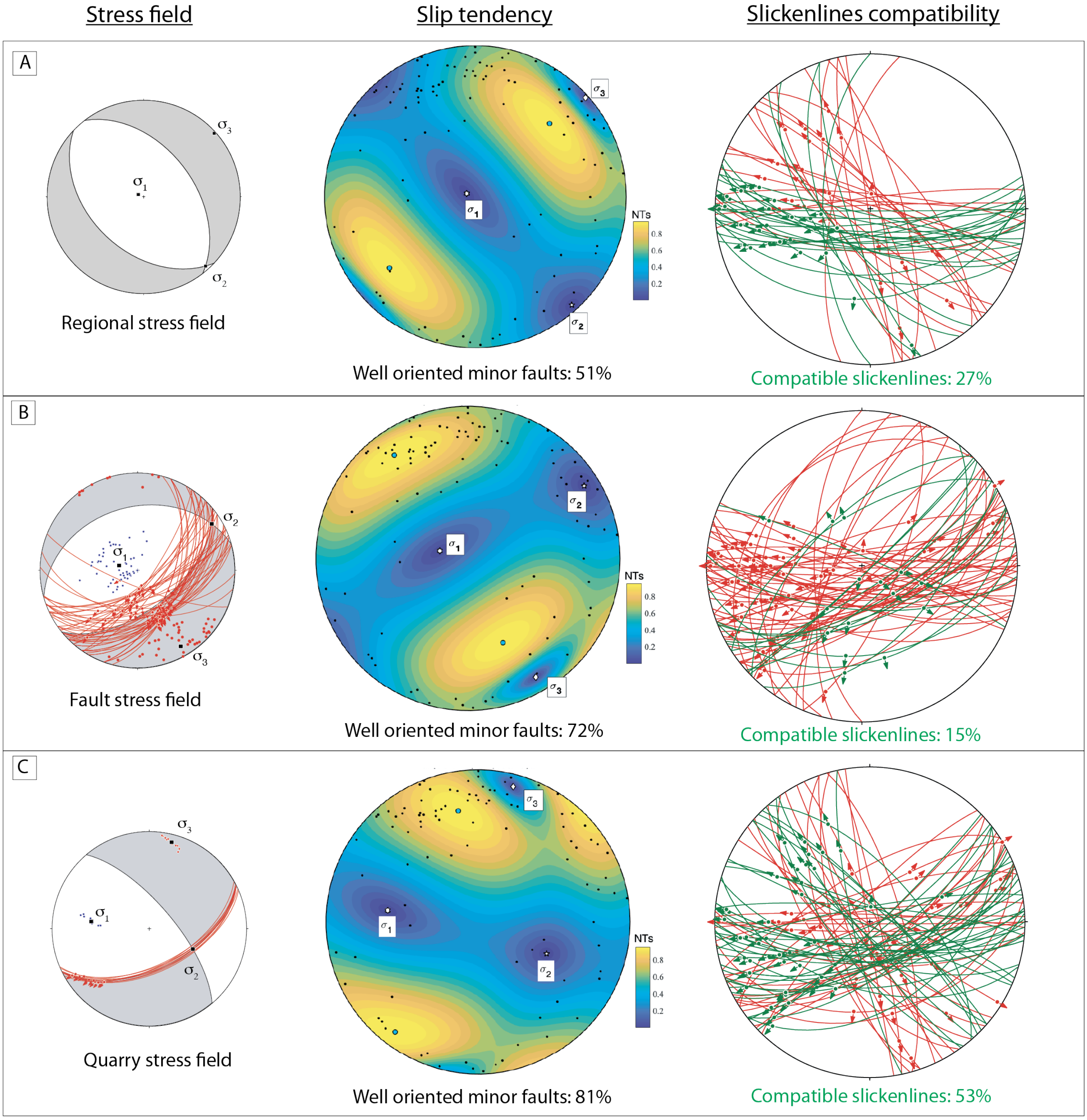

Figure 3.8 - Normalised slip tendency and slickenlines compatibility analysis for three hypothesized stress fields: active regional NE-SW orientated extension (regional stress field; A), NW-SE oriented extension (fault stress field; B) compatible with the mainly dip-slip slickenlines observed for the whole Tre Monti fault, and a quarry stress field (C) calculated from the inversion of the right-lateral slickenlines observed on the front segment of the relay ramp. Black dots in the slip tendency stereoplots represent the poles to the minor faults. The slip tendency stereoplots have been produced using a MATLAB tool for slip tendency (Bistacchi et al., 2012). Green and Red colours in the slickenlines compatibility stereoplots represent respectively compatible and non-compatible slickenlines with respect to the predicted slickenlines orientation in a given stress field.

2016). Our mechanical analysis suggests that in the case study of the Tre Monti fault, further geometrical and kinematic complexity can be added by the temporal competition and interaction of various stress fields. Each stress field can either be responsible of the formation of new faults, renewing the minor faults population and

Strike	Abundance	Well-oriented			Slickenlines compatibility		
		Regional	Fault	Quarry	Regional	Fault	Quarry
E-W	41%	29%	41%	36%	22%	5%	23%
NE-SW	27%	0%	26%	20%	0%	9%	9%
NW-SE	18%	12%	2%	18%	2%	3%	10%
N-S	14%	10%	5%	7%	3%	0%	1%
All	**100%**	**51%**	**72%**	**81%**	**27%**	**15%**	**53%**

Table 3.2 - Results for the slip tendency and slickenline compatibility analysis for different fault orientation.

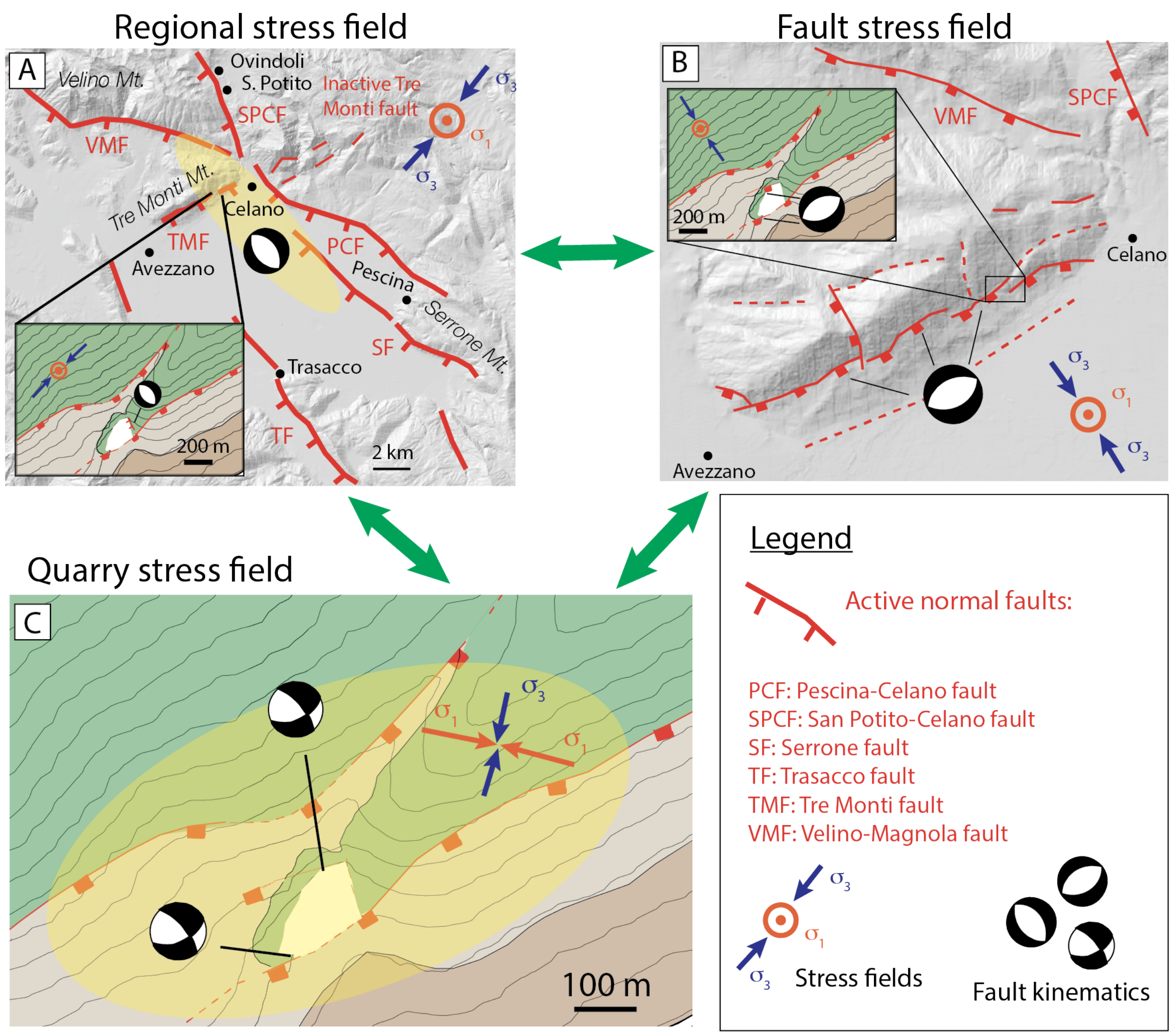

Figure 3.9 - Interpretation of the complex kinematics of minor faults. Minor faults geometry and kinematics reflect the local-scale temporal interaction between various stress fields. (A) a NE-SW oriented extension acting at regional scale (i.e., regional stress field), and (B) a NW-SE oriented extension (fault stress field) at sub-regional scale (10 km scale), due to the release fault geometry of the Tre Monti fault add further geometrical and kinematic complexity to (C) a quarry stress field due to the interaction of two main fault strands that borders the quarry.

increasing the geometrical complexity, or can promote slip on pre-existing well-oriented faults. In this area of Central Apennines, when the regional stress field prevails, promoting slip on the San Potito-Celano and/or Pescina-Celano faults (Fig.

3.9a), in the relay zone of the Tre Monti fault slip is favoured on NW-SE structures with dip-slip kinematics and on W-E striking structures with right-lateral movements. On the contrary, when the stress field associated with the Tre Monti fault prevails (i.e. fault stress field; Fig 3.9b), slip is favoured on NW-SE oriented structures with dip-slip kinematics.

However, the large number of minor faults that show geometric and kinematic compatibility with the quarry stress field (Fig. 3.8c) indicate that the majority of the minor structures are due to the interaction between the two main fault strands which creates an oblique dextral kinematics on the relay zone (Fig. 3.9c). We therefore suggest that the complex geometry and kinematics of the minor faults in the relay ramp of the Tre Monti fault is mainly a result of a local stress field caused by interaction between the overlapping fault segments. Further kinematic complexity can be explained by the transient influence of regional and fault-scale stress fields at a local scale.

3.6. CONCLUSION

Using fieldwork and virtual outcrop technologies, we investigated the subsidiary faults geometry and kinematics within a carbonate-hosted relay ramp. The structural map and cross section reconstructed in our study (scale 1: 2,000 and 1:1,000 respectively) allow for a detailed characterization of the subsidiary faults geometry. The largest subsidiary faults show an orientation that is sub-parallel to the main fault segments accompanied by smaller faults with different attitudes and often striking orthogonally to the main fault. Faults also show a wide range of kinematics (left-lateral, dip-slip, right-lateral) independently of their orientation. Based on fault slip analysis, accounting for both fault geometry and kinematics, we suggest that the complex minor fault geometry and kinematics can be mostly explained by the development of a stress perturbation within the relay zone, resulting from the interaction of the overlapping segments. Further geometrical and kinematic complexity may be interpreted as due to the temporary superposition of either the stress field associated with the slip of the entire Tre Monti Fault or the regional active extension. Our results highlight that the geometry and kinematics of minor faults within relay zones are dependent on stress field interactions across the scales.

ACKNOWLEDGEMENTS

We thank two anonymous reviewers, whose comments helped to improve the quality of the manuscript. We also thank Andrea Billi, Manuel Curzi, Carolina Giorgetti, Telemaco Tesei, Patrizio Petricca and

Fabio Trippetta for fruitful discussions, and Marco Baleani, Angelo Galeandro, and Francesco Mohammadi for their help during the laser scanner survey. The virtual outcrop analysis was carried out in Durham University, Earth Sciences Department during a 2-month internship. We also acknowledge Andrea Bistacchi who developed the slip tendency Matlab toolbox that we used for this study. This research was supported by the Sapienza University of Rome Earth Sciences Department Ph.D. funds and Sapienza Progetti di Ateneo 2017 to EC. KM's work in the Apennines was funded by NERC awards NE/I026715/1 and NE/E016545/1.

REFERENCES

Agosta, F. & **Aydin, A.** (2006). Architecture and deformation mechanism of a basin-bounding normal fault in Mesozoic platform carbonates, central Italy. *Journal of Structural Geology* 28, 1445–1467.

Allmendinger, R.W., Cardozo, N., & **Fisher, D.M.** (2011). Structural geology algorithms: Vectors and tensors, Cambridge University Press. Cambridge University Press.

Angelier, J. (1984). Tectonic analysis of fault slip data sets. *Journal of Geophysical Research: Solid Earth*, 89(B7), 5835-5848.

Bastesen, E. & **Rotevatn, A.** (2012). Evolution and structural style of relay zones in layered limestone–shale sequences: insights from the Hammam Faraun Fault Block, Suez Rift, Egypt. *Geol. Soc. Lond.* 169, 477–488.

Bellian, J.A., Kerans, C., & **Jennette, D.C.** (2005). Digital Outcrop Models: Applications of Terrestrial Scanning Lidar Technology in Stratigraphic Modeling. *Journal of Sedimentary Research* 75, 166–176.

Benedetti, L., Manighetti, I., Gaudemer, Y., Finkel, R., Malavieille, J., Pou, K., Arnold, M., Aumaître, G., Bourlès, D., & **Keddadouche, K.** (2013). Earthquake synchrony and clustering on Fucino faults (Central Italy) as revealed from in situ 36Cl exposure dating. *Journal of Geophysical Research: Solid Earth* 118, 4948–4974.

Berkowitz, B. (1995). Analysis of fracture network connectivity using percolation theory. *Math. Geol.* 27, 467–483.

Bistacchi, A., Massironi, M., Menegon, L., Bolognesi, F., & **Donghi, V.** (2012). On the nucleation of non-andersonian faults along phyllosilicate-rich mylonite belts. *Geol. Soc. Lond. Spec. Publ.* 367 (1), 185-199

Bonson, C.G., Childs, C., Walsh, J.J., Schöpfer, M.P.J., & **Carboni, V.** (2007). Geometric and kinematic controls on the internal structure of a large normal fault in massive limestones: The Maghlaq Fault, Malta. *Journal of Structural Geology* 29, 336–354.

Bott, M. (1959). The Mechanics of Oblique Slip Faulting. *Geological Magazine* 96, 109–117.

Buckley, S.J., Howell, J.A., Enge, H.D., & **Kurz, T.H.** (2008). Terrestrial laser scanning in geology: data acquisition, processing and accuracy considerations. *Journal of the Geological Society* 165, 625–638.

Carpenter, B. M., Collettini, C., Viti, C., & **Cavallo, A.** (2016). The influence of normal stress and sliding velocity on the frictional behaviour of calcite at room temperature: insights from laboratory experiments and microstructural observations. *Geophysical Journal International,* 205(1), 548-561.

Cavinato, G. P., Carusi, C., Dall'Asta, M., Miccadei, E., & **Piacentini, T**. (2002). Sedimentary and tectonic evolution of Plio–Pleistocene alluvial and lacustrine deposits of Fucino Basin (central Italy). *Sedimentary Geology*, 148(1-2), 29-59.

Cavinato, G.P. & **De Celles, P.G.** (1999). Extensional basins in the tectonically bimodal central Apennines fold-thrust belt, Italy: response to corner flow above a subducting slab in retrograde motion. *Geology* 27, 955–958.

Chiaraluce, L. (2012). Unravelling the complexity of Apenninic extensional fault systems: A review of the 2009 L'Aquila earthquake (Central Apennines, Italy). *Journal of Structural Geology* 42, 2–18.

Chiaraluce, L., Di Stefano, R., Tinti, E., Scognamiglio, L., Michele, M., Casarotti, E., ... & Lombardi, A. (2017). The 2016 central Italy seismic sequence: A first look at the mainshocks, aftershocks, and source models. *Seismological Research Letters*, *88*(3), 757-771.

Çiftçi, N. B. & **Bozkurt, E.** (2007). Anomalous stress field and active breaching at relay ramps: a field example from Gediz Graben, SW Turkey. *Geological Magazine*, 144(4), 687-699.

Collettini, C., Carpenter, B.M., Viti, C., Cruciani, F., Mollo, S., Tesei, T., Trippetta, F., Valoroso, L., & **Chiaraluce, L.**, (2014). Fault structure and slip localization in carbonate-bearing normal faults: An example from the Northern Apennines of Italy. *Journal of Structural Geology* 67, 154–166.

Collettini, C. & **Trippetta, F**. (2007). A slip tendency analysis to test mechanical and structural control on aftershock rupture planes. *Earth and Planetary Science Letters* 255, 402–413.

Cosentino, D., Cipollari, P., Marsili, P., & **Scrocca, D.** (2010). Geology of the central Apennines: a regional review. *Journal of the virtual explorer*, *36*(11), 1-37.

Cowie, P., Phillips, R., Roberts, G., McCaffrey, K., Zijerveld, L., Gregory, L., Walker, F.J., Wedmore, L., Dunai, T., Binnie, S., Freeman, S., Wilcken, K., Shanks, R., Huismans, R., Papanikolaou, I., Michetti, A., & **Wilkinson, M.** (2017). Orogen-scale uplift in the central Italian Apennines drives episodic behaviour of earthquake faults. *Scientific Reports* 7, 44858.

Crider, J.G., & **Pollard, D.D.** (1998). Fault linkage: Three-dimensional mechanical interaction between echelon normal faults. *Journal of Geophysical Research: Solid Earth* 103, 24373–24391.

Curewitz, D. & **Karson, J.A.** (1997). Structural settings of hydrothermal outflow: fracture permeability maintained by fault propagation and interaction. *J. Volcanol. Geotherm.Res.* 79, 149–168

D'Agostino, N., Giuliani, R., Mattone, M., & **Bonci, L.** (2001). Active crustal extension in the Central Apennines (Italy) inferred from GPS measurements in the interval 1994–1999. *Geophysical Research Letters* 28, 2121–2124.

Demurtas, M., Fondriest, M., Balsamo, F., Clemenzi, L., Storti, F., Bistacchi, A., & **Di Toro, G.** (2016). Structure of a normal seismogenic fault zone in carbonates: The Vado di Corno Fault, Campo Imperatore, Central Apennines (Italy). *Journal of Structural Geology* 90, 185–206.

Destro, N. (1995). Release fault: A variety of cross fault in linked extensional fault systems, in the Sergipe-Alagoas Basin, NE Brazil. *Journal of Structural Geology* 17, 615–629.

Devoti, R., Pietrantonio, G., Pisani, A., Riguzzi, F., & **Serpelloni, E.** (2010). Present day kinematics of Italy. *Journal of the virtual explorer* 36.

Di Domenica, A., Petricca, P., Trippetta, F., Carminati, E., & **Calamita, F.,** (2014). Investigating fault reactivation during multiple tectonic inversions through mechanical and numerical modeling: An application to the Central-Northern Apennines of Italy. *Journal of Structural Geology* 67, 167–185.

Dockrill, B. & **Shipton, Z.K.,** (2010). Structural controls on leakage from a natural CO2 geologic storage site: Central Utah, U.S.A. *J. Struct. Geol.* 32.

Doglioni, C. (1991). A proposal for the kinematic modelling of W dipping subductions possible applications to the Tyrrhenian Apennines system. *Terra Nova* 3, 423–434.

Ferrarini, F., Lavecchia, G., de Nardis, R., & **Brozzetti, F.** (2015). Fault Geometry and Active Stress from Earthquakes and Field Geology Data Analysis: The Colfiorito 1997 and L'Aquila 2009 Cases (Central Italy). *Pure and Applied Geophysics* 172, 1079–1103.

Fossen, H., Johansen, T.E.S., Hesthammer, J., & **Rotevatn, A**. (2005). Fault interaction in porous sandstone and implications for reservoir management; examples from Southern Utah. *AAPG Bull.* 89, 1593–1606.

Fossen, H., & **Rotevatn, A.** (2016). Fault linkage and relay structures in extensional settings—A review. *Earth-Science Reviews*, 154, 14-28.

Galadini, F., & **Messina, P.** (1994). Plio-Quaternary tectonics of the Fucino basin and surrounding areas (central Italy). *Giornale di Geologia*, 56(2), 73-99.

Galadini, F. & **Messina, P**. (2001). Plio-Quaternary changes of the normal fault architecture in the Central Apennines (Italy). *Geodinamica Acta* 14, 321–344.

Gori, S., Falcucci, E., Ladina, C., Marzorati, S., & **Galadini, F.** (2017). Active faulting, 3-D geological architecture and Plio-Quaternary structural evolution of extensional basins in the central Apennine chain, Italy. *Solid Earth* 8, 319–337.

Heidbach, O., Rajabi, M., Reiter, K., Moritz, & **WSM Team** (2016). World Stress Map Database Release 2016. GFZ Data Services.

Hodgetts, D. (2013). Laser scanning and digital outcrop geology in the petroleum industry: A review. *Marine and Petroleum Geology* 46, 335–354.

Hus, R., De Batist, M., Klerkx, J., & **Matton, C**. (2006). Fault linkage in continental rifts: structure and evolution of a large relay ramp in Zavarotny; Lake Baikal (Russia). *Journal of structural geology*, 28(7), 1338-1351.

Kattenhorn, S.A., Aydin, A., & **Pollard, D.D**. (2000). Joints at high angles to normal fault strike: an explanation using 3-D numerical models of fault-perturbed stress fields. *J. Struct. Geol*. 22, 1–23.

Larsen, P. H. (1988). Relay structures in a Lower Permian basement-involved extension system, East Greenland. *Journal of Structural Geology*, 10(1), 3-8.

Lisle, R.J. & **Srivastava, D.C.** (2004). Test of the frictional reactivation theory for faults and validity of fault-slip analysis. *Geology* 32, 569.

Long, J.J. & **Imber, J.** (2012). Strain compatibility and fault linkage in relay zones on normal faults. *Journal of Structural Geology* 36, 16–26.

Marrett, R., & **Allmendinger, R.W.** (1990). Kinematic analysis of fault-slip data. *Journal of Structural Geology* 973–986.

McCaffrey, K., Holdsworth, R., Imber, J., Clegg, P., De Paola, N., Jones, R., Hobbs, R., Holliman, N., & **Trinks, I.** (2005a). Putting the geology back into Earth models. Eos, *Transactions American Geophysical Union* 86, 461–466.

McCaffrey, K.J.W., Jones, R.R., Holdsworth, R.E., Wilson, R.W., Clegg, P., Imber, J., Holliman, N., & **Trinks, I.** (2005b). Unlocking the spatial dimension: digital technologies and the future of geoscience fieldwork. *Journal of the Geological Society* 162, 927–938

Montone, P., Mariucci, T.M., Pondrelli, S., & **Amato, A.** (2004). An improved stress map for Italy and surrounding regions (central Mediterranean). *Journal of Geophysical Research: Solid Earth* 109.

Morewood, N.C. & **Roberts, G.P.** (2000). The geometry, kinematics and rates of deformation within an en échelon normal fault segment boundary, central Italy. *Journal of Structural Geology* 22, 1027–1047.

Morris, A., Ferrill, D.A., & **Henderson D.B.,** (1996). Slip-tendency analysis and fault reactivation. *Geology* 24, 275–278.

Patacca, E., Scandone, P., Di Luzio, E., Cavinato, G. P., & **Parotto, M**. (2008). Structural architecture of the central Apennines: Interpretation of the CROP 11 seismic profile from the Adriatic coast to the orographic divide. *Tectonics*, 27(3).

Peacock, D.C.P. & **Parfitt, E.A.** (2002). Active relay ramps and normal fault propagation on Kilauea Volcano, Hawaii. *J. Struct. Geol*. 24, 729–742.

Peacock, D.C.P., Price, S.P., & **Pickles, C.S.** (2000). The world's biggest relay ramp: hold with hope, NE Greenland. J. *Struct. Geol*. 22, 843–850.

Peacock, D. C. P., & **Sanderson, D. J.** (1991). Displacements, segment linkage and relay ramps in normal fault zones. *Journal of Structural Geology,* 13(6), 721-733.

Peacock, D. C. P., & **Sanderson, D. J.** (1994). Geometry and development of relay ramps in normal fault systems. *AAPG bulletin,* 78(2), 147-165.

Peacock, D.C.P., Dimmen, V., Rotevatn, A., & **Sanderson, D.J.** (2017). A broader classification of damage zones. *Journal of Structural Geology* 102, 179–192.

Pless, J., McCaffrey, K., Jones, R., Holdsworth, R., Conway, A., & **Krabbendam, M.** (2015). 3D characterization of fracture systems using Terrestrial Laser Scanning: an example from the Lewisian basement of NW Scotland. *Geological Society, London, Special Publications* 421, 125–141.

Rotevatn, A., Buckley, S., Howell, J., & **Fossen, H.** (2009). Overlapping faults and their effect on fluid flow in different reservoir types: A LIDAR-based outcrop modeling and flow simulation study. *AAPG Bulletin* 93, 407–427.

Rowland, J.V. & **Sibson, R.H.** (2004). Structural controls on hydrothermal flow in a segmented rift system, Taupo Volcanic Zone, New Zealand. *Geofluids* 4, 259–283.

Scognamiglio, L., Tinti, E., Michelini, A., Dreger, D., Cirella, A., Cocco, M., Mazza, S., & Piatanesi, A. (2010). Fast Determination of Moment Tensors and Rupture History: What Has Been Learned from the 6 April 2009 L'Aquila Earthquake Sequence. *Seismological Research Letters* 81, 892–906.

Seers, T. & Hodgetts, D. (2016). Extraction of three-dimensional fracture trace maps from calibrated image sequences. *Geosphere* 12, 1323–1340.

Sibson, R.H. (1996). Structural permeability of fluid-driven fault-fracture meshes. *J. Struct. Geol.* 18, 1031–1042.

Smeraglia, L., Berra, F., Billi, A., Boschi, C., Carminati, E., & Doglioni, C. (2016). Origin and role of fluids involved in the seismic cycle of extensional faults in carbonate rocks. *Earth and Planetary Science Letters* 450, 292–305.

Smeraglia, L., Bettucci, A., Billi, A., Carminati, E., Cavallo, A., Di Toro, G., Natali, M., Passeri, D., Rossi, M., & Spagnuolo, E. (2017). Microstructural evidence for seismic and aseismic slips along clay-bearing, carbonate faults. *Journal of Geophysical Research: Solid Earth*, 122(5), 3895-3915.

Smith, S.A., Billi, A., Toro, G., & Spiess, R. (2011). Principal Slip Zones in Limestone: Microstructural Characterization and Implications for the Seismic Cycle (Tre Monti Fault, Central Apennines, Italy). *Pure and Applied Geophysics* 168, 2365–2393.

Tavani, S., Granado, P., Corradetti, A., Girundo, M., Iannace, A., Arbués, P., ... & Mazzoli, S. (2014). Building a virtual outcrop, extracting geological information from it, and sharing the results in Google Earth via OpenPlot and Photoscan: An example from the Khaviz Anticline (Iran). *Computers & Geosciences*, 63, 44-53.

Telling, J., Lyda, A., Hartzell, P., & Glennie, C. (2017). Review of Earth science research using terrestrial laser scanning. *Earth-Science Reviews*, *169*, 35-68.

Tesei, T., Collettini, C., Barchi, M. R., Carpenter, B. M., & Di Stefano, G. (2014). Heterogeneous strength and fault zone complexity of carbonate-bearing thrusts with possible implications for seismicity. *Earth and Planetary Science Letters*, *408*, 307-318.

Thiele, S.T., Lachlan, Samsu, A., Micklethwaite, S., Voggler, S.A., & Cruden, A.R. (2017). Rapid, semi-automatic fracture and contact mapping for point clouds, images and geophysical data. *Solid Earth* 8, 1241–1253.

Valoroso, L., Chiaraluce, L., & Collettini, C. (2014). Earthquakes and fault zone structure. *Geology* 42, 343–346.

Wallace, R.E. (1951). Geometry of Shearing Stress and Relation to Faulting. *The Journal of Geology* 59, 118–130.

4. Lithological and structural control on fracture distribution within a carbonate-hosted relay ramp

Marco Mercuri[1], Eugenio Carminati[1], Maria Chiara Tartarello[1], Marco Brandano[1], Paolo Mazzanti[1,2], Alessandro Brunetti[2], Ken J. W. McCaffrey[3], and Cristiano Collettini[1]

1: Dipartimento di Scienze della Terra, Sapienza Università di Roma, P.le Aldo Moro 5, 00185 Roma, Italy.
2: NHAZCA S.r.l., spin-off company University of Rome "Sapienza", Via Vittorio Bachelet 12, 00185 Rome, Italy
3: Earth Sciences Department, Durham University, South Road, Durham, DH1 3LE, UK

Submitted to *Journal of Structural Geology*

ABSTRACT

Understanding the factors controlling fracture distribution is fundamental to better assess fluids circulation in fault damage zones, with evident implications for fault mechanics, hydrogeology and hydrocarbon exploration. Being usually characterized by a strong damage and structural complexity, this is of particularly importance for relay zones. We investigated the fracture distribution within a portion of a relay ramp hosted within peritidal carbonates and pertaining to the Tre Monti fault (Central Italy). We analysed the distribution of the fracture frequency in the outcrop through (1) scanlines measured in the field, (2) oriented rock samples, and (3) scan-areas performed on a virtual outcrop model. Fracture frequency increases with distance from the front segment of the relay ramp. Moreover, supratidal and intertidal carbonate facies exhibit higher fracture frequency than subtidal limestones. This trend of increased fracture frequency has two main explanations. (1) The increase in the number of subsidiary faults and their associated damage zones moving away from the front segment. (2) The increase of supratidal and intertidal carbonate facies content toward the centre of the relay ramp. Our results highlight structural and lithological control on fracture distribution within relay ramps hosted in shallow water limestones.

4.1. INTRODUCTION

Fractures in the damage zone (Chester and Logan, 1986; Chester et al., 1993) constitute the main pathway for fluids within faults hosted in low-porosity rocks (Caine et al., 1996; Aydin, 2000; Gudmundsson et al., 2001; Bense et al., 2013; Bigi et al., 2013). The distribution of fractures and the variation of their geometrical and topological properties in space can have important consequences on permeability, and hence on the fluid flow and fault mechanics. For example, it may define traps and leakage points within hydrocarbon reservoirs affected by the presence of faults and promote or prevent local fluid overpressures. A poorly connected fracture system might lead to the development of high fluid pressures, which can in turn influence the evolution of the stress state (Sibson, 1994) with profound implications for earthquake triggering (e.g., Nur and Booker, 1972; Miller et al., 2004). Conversely, a well-connected fracture system prevents the development of fluid overpressures and this leads to the maintenance of a strong but critically stressed crust (Townend and Zoback, 2000). Furthermore, fracture distribution can have a direct effect on fault mechanics: the change of the elastic properties of the host rock promoted by fracturing may lead to a stress field rotation within the damage zone, allowing the reactivation of unfavourably orientated faults (Faulkner et al., 2006). The characterization of fracture distribution and its controlling factors is therefore fundamental to better understand fluid circulation and the mechanics of fault zones, with obvious consequences for hydrogeology and hydrocarbon exploration. Assessing fracture distribution is particularly relevant for relay ramps (and generally, for zones of faults interaction), as they are commonly characterized by a stronger damage than isolated fault segments (Kim et al., 2004; Peacock et al., 2017) and by high structural complexity (Kattenhorn et al., 2000; Peacock et al., 2000; Peacock and Parfitt, 2002; Fossen et al., 2005; Ciftci & Bozkurt, 2007; Bastesen and Rotevatn, 2012; Peacock et al., 2017), with important consequences for fluid flow (Sibson, 1996; Rotevatn et al., 2007; Fossen and Rotevatn, 2016 and references therein). Here we integrate classical and modern structural geology techniques to investigate the fracture distribution and its controlling factors within a well-exposed portion of a carbonate-hosted relay ramp damage zone pertaining to the Tre Monti fault, a normal fault in the Central Apennines of Italy. We observe that lithology (carbonate facies) and the secondary faults accompanying the relay ramp development play an important role in the fracture distribution.

4.1.1. Factors controlling fracture distribution within fault zones.

Many field and laboratory studies have been carried out to investigate the factors controlling fracture distribution within fault zones. A first factor is represented by the distance from the main fault: fracture intensity generally increases moving toward the fault core (Brock and Engelder, 1977; Wilson et al., 2003; Faulkner et al., 2006; Mitchell and Faulkner, 2009). However, fracture intensity does not scale with the displacement accommodated by the main fault (Anders and Wiltschko, 1994; Shipton and Cowie, 2003). This has been attributed to the existence of a critical value of deformation intensity marking the transition from a strain hardening to a strain softening behaviour induced by the development of slip surfaces (Shipton and Cowie, 2003). Thus, bigger displacements accommodated by faults lead to an increase in the damage zone thickness (Shipton and Cowie, 2001, 2003; Mitchell and Faulkner, 2009; Savage and Brodsky, 2011). This can be attributed to the continuous development of subsidiary faults producing their own damage zone (Shipton and Cowie, 2003). Other fault-related factors that influence the distribution and the geometrical/topological properties of fractures are related to the stress field. For example, the asymmetric pattern of the stress field occurring during the long-term propagation of a fault (Berg and Skar, 2005), and the rupture directivity during earthquakes (Dor et al., 2006a, 2006b; Mitchell et al., 2011) may produce an asymmetric damage distribution between the hangingwall and footwall, whilst the development of local stresses may promote the deflection of fractures (Gudmundsson et al., 2010).

Another important role in fracture distribution is played by lithology. The stratigraphic or tectonic juxtaposition of different lithologies leads to contrasts in mechanical properties (e.g., brittleness; Peacock and Xing, 1994) causing a mechanical layering that influences the deformation pattern (Tavani et al., 2008), and fracture spacing, propagation and arrest (Odling et al., 1999; McGinnis et al., 2017). In general, fractures tend to form in more brittle layers and they often arrest at interfaces where mechanical contrasts are present (e.g., bedding). For carbonate lithologies, even a variation in carbonate facies at metric to decametric scale can affect fracturing (Wennberg et al., 2006; De Paola et al., 2008; Larsen et al., 2010a, 2010b; Michie et al., 2014; Rustichelli et al., 2016; Volatili et al., 2019). For example, Rustichelli et al. (2016) observed higher fracture intensity, trace length and connectivity in platform compared to ramp carbonates, whilst Larsen and co-authors (2010a, b) found that fractures forming in the subtidal facies tend to arrest in proximity to the intertidal laminated limestones. Finally, the thickness of sedimentary beds can influence fracturing: a widely observed relationship is that, for strata-bound fractures, fracture intensity is inversely proportional to bed thickness (Ladeira and Price, 1981; Pollard and Aydin, 1988; Huang and Angelier, 1989; Narr and Suppe, 1991; Wu and Pollard, 1995; Bai and Pollard, 2000).

4.1.2. The structure-from-motion algorithm to build virtual outcrops

In this study we integrate classical field techniques (i.e., scanlines; Wu and Pollard, 1995) and a virtual outcrop (Bellian et al., 2005; McCaffrey et al., 2005a, 2005b) to investigate the fracture distribution and its controlling factors in a relay ramp system formed in carbonate host rocks.

In the last decade, virtual outcrops have been extensively used in structural geology (Bemis et al., 2014; Telling et al., 2017 for a review), and in particular for studies dealing with fractures (Olariu et al., 2008; Vasuki et al., 2014; Pless et al., 2015; Casini et al., 2016; Seers and Hodgetts, 2016; Corradetti et al., 2017; Bonali et al., 2019 and many others). The employment of virtual outcrops in geology has increased our ability and efficiency to collect data, allowing the collection of high-precision georeferenced datasets, also from inaccessible portions of the outcrop (Bellian et al., 2005; McCaffrey et al., 2005a, 2005b). An increasingly adopted methodology to build virtual outcrops is represented by the structure-from-motion technique (Westoby et al., 2012; Bemis et al., 2014; Colomina and Molina, 2014; Tavani et al., 2014; Vasuki et al., 2014; Bistacchi et al., 2015; Bonali et al., 2019), because it has a higher efficiency to cost ratio than others techniques such as laser scanning (LiDAR) (Wilkinson et al., 2016; Cawood et al., 2017). The structure-from-motion algorithm exploits a series of overlapping photos taken from various positions by a person or a drone (UAV, Unmanned Aerial Vehicle) to build a 3D model of the scene (Bemis et al., 2014). The model can be sized and georeferenced using the knowledge of the geographic position of some objects (i.e., ground control points) in the scene (Bemis et al., 2014). For this study, the employment of a virtual outcrop allowed us to accurately map the fracture distribution in our study outcrop.

4.2. GEOLOGICAL SETTING

4.2.1. The central Apennines tectonic framework

The central Apennines are an active NE to ENE verging fold-and-thrust belt that started to form in the late-Oligocene in response to the westward directed subduction of the Adria plate beneath the European plate (Doglioni, 1991; Carminati et al., 2010). Thrusting scraped-off and piled up the sedimentary sequence overlying the continental basement of Adria, including a shallow- to deep- water Upper Triassic to Middle Miocene carbonate succession (Cosentino et al., 2010 and references therein). Since the Early Pliocene, NE-SW oriented extensional tectonics started to act in the Apennines to west of the compressive front, in response to the opening of the Thyrrenian back-arc basin (Doglioni, 1991). The compressive-extensional couple has continuously migrated to the northeast (Cavinato and De Celles, 1999). Extension is currently active in the Apennines (D'Agostino et al., 2001a; Devoti et al., 2010) and is accommodated by normal faults striking mainly NW-SE, although some SW-NE trending fault, such as the Tre Monti fault are present (Fig. 4.1a). These faults cut through both the pre-orogenic carbonates and the syn-orogenic flysch deposits (Fig. 4.1a), and their activity is manifested in the numerous earthquakes that have affected Italy in the recent past, such as the L'Aquila 2009 (Chiaraluce, 2012 and references therein), and the 2016-17 central Italy seismic sequences (Chiaraluce et al., 2017; Scognamiglio et al., 2018). The exhumation associated with the uplift that accompanies the extensional tectonic regime (D'Agostino et al., 2001b; Devoti et al., 2010) has exposed formerly buried active normal faults that now usually constitute the borders of the intermountain basins. The Tre Monti fault borders to the north-west the Fucino intermontane basin (Fig. 4.1a). In the Fucino basin, thrusting occurred from the Late Miocene to Early Pliocene, whilst the extensional tectonics started in the Late Pliocene and it is still ongoing, as testified by the 1915 Avezzano earthquake (e.g., Galadini and Galli, 1999).

4.2.2. The Tre Monti fault

Tre Monti fault has been exhumed from a depth < 3 km (Smeraglia et al., 2016) and crops out with a series of right-stepping, SE dipping fault scarps for a length of ~ 7 km (Fig. 4.1b). The fault accommodates a throw that is comprised between ~ 0.7 km in the SW to ~ 2 km towards the NE (Smeraglia et al., 2016). The fault scarps juxtapose the Early Cretaceous to Miocene carbonates in the footwall with the Pliocene to Holocene continental deposits in the hangingwall (Fig. 4.1a, b). The predominance of dip slip slickenlines on the main fault scarps (Fig. 4.1b; See also

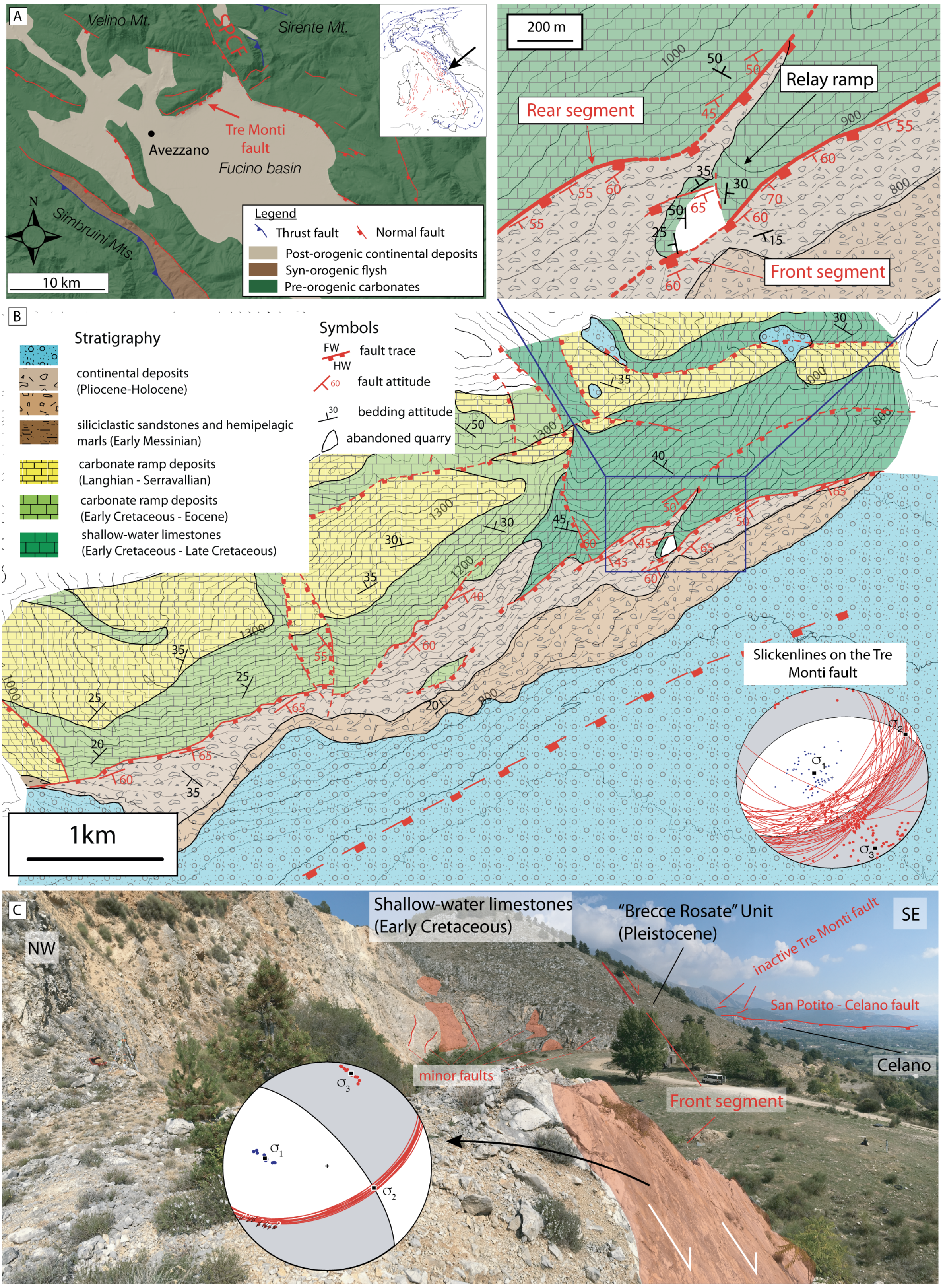

Figure 4.1 - Geological setting of the analysed outcrop. (A) The Tre Monti fault is located in the Central Apennines of Italy (inset in panel A) and borders the Fucino basin to the NNW. SPCF: San Potito – Celano fault. (B) The Tre Monti fault crops out with a series of right-stepping fault scarps and puts in contact the Cretaceous to Miocene shallow water carbonates in the footwall with Pliocene to Holocene continental deposits in the hangingwall. The fault scarps are characterized by mainly dip-slip slickenlines (stereoplot in B; Schmidt's net, lower hemisphere). The study quarry is located in the footwall of the front segment of a relay zone (inset in figure B). (C) The damage zone is characterized by heavily fractured shallow water limestones, early Cretaceous in age. Kinematic indicators on the main fault in the quarry (front segment of the relay ramp) indicate a right-lateral kinematics. The stress inversion and the fault plane solutions in (B) and (C) have been performed through Linked-Bingham Analysis in FaultKin (Marrett and Allmendinger, 1990; Allmendinger et al., 2011)

Morewood and Roberts, 2000; Smeraglia et al., 2016 and Chapter 3) and paleoseismological investigations (Benedetti et al., 2013; Cowie et al., 2017) indicate that the Tre Monti fault has been active as a normal fault since the Pliocene, probably acting as a release fault (sensu Destro, 1995) for the San Potito – Celano fault (Fig. 4.1a). Finally, the Tre Monti fault has experienced past earthquakes, as suggested by microstructural studies of the fault core (Smith et al., 2011; Smeraglia et al., 2016, 2017).

A key outcrop for the Tre Monti fault zone structure is provided by an abandoned quarry located ~ 2 km WSW of Celano village (42°04'35"N 13°30'00"E; see also Fig. 4.1b). The quarry is located within a portion of a relay zone delimitated by two right-stepping segments on the main fault (zoom in Fig. 4.1b) and has been named "La Forchetta quarry" in previous studies (Smeraglia et al., 2016, 2017; see also Chapter 3). The quarry extends for ~ 200 m in a SW-NE direction and for ~ 100 m in the NW-SE direction (inset of Fig. 4.1b). The south-eastern limit of the quarry is marked by the front segment of the relay ramp (Fig. 4.1b-c). This dips (~55°) to the southeast (156° mean dip azimuth) (Smeraglia et al., 2016; see also Chapter 2; Fig. 4.1c). The slickenlines on the front segment indicate a right-transtensional to right-lateral kinematics (mean rake 155°; Fig. 4.1c). The kinematics observed here may be due to a stress field rotation promoted by the interaction of the segments that border the relay zone (Chapter 3).

The damage zone is exposed in an almost 360° perspective on the quarry walls (Fig. 4.1c) and is hosted by Lower Cretaceous limestones pertaining to the "*Calcari Ciclotemici a Gasteropodi e ooliti*" Formation (Centamore et al., 2006). They were deposited at the transition between tidal flat and lagoon carbonate platform environments (Fig. 4.2a) and are organized in metric-scale peritidal cycles (Fig. 4.2b), reflecting the variation of accommodation space (c.f., Osleger 1991; D'Argenio et al., 1997). The supratidal facies is composed of light-gray to havana-brown poorly sorted grainstones with radial ooids and pisoids (Fig. 4.2e, h). The intertidal facies is defined by laminated, white coloured microbial bindstones with birdseyes and fenestrae (Fig. 4.2f, i). Finally, the subtidal facies is mainly composed of white packstones with peloids and oncoids (Fig. 4.2g, j), although some sporadic floatstones with gastropods and some oncoidal rudstones are present.

The bedding organization is strongly controlled by the relative abundance of the carbonate facies mentioned above. Where the supratidal and the intertidal are the most abundant facies, the limestones crops out in cm- to dm- scale tabular beds (Fig. 4.2c). Conversely, a predominance of the subtidal facies leads to beds that are more than 1 m thick (Fig. 4.2d).

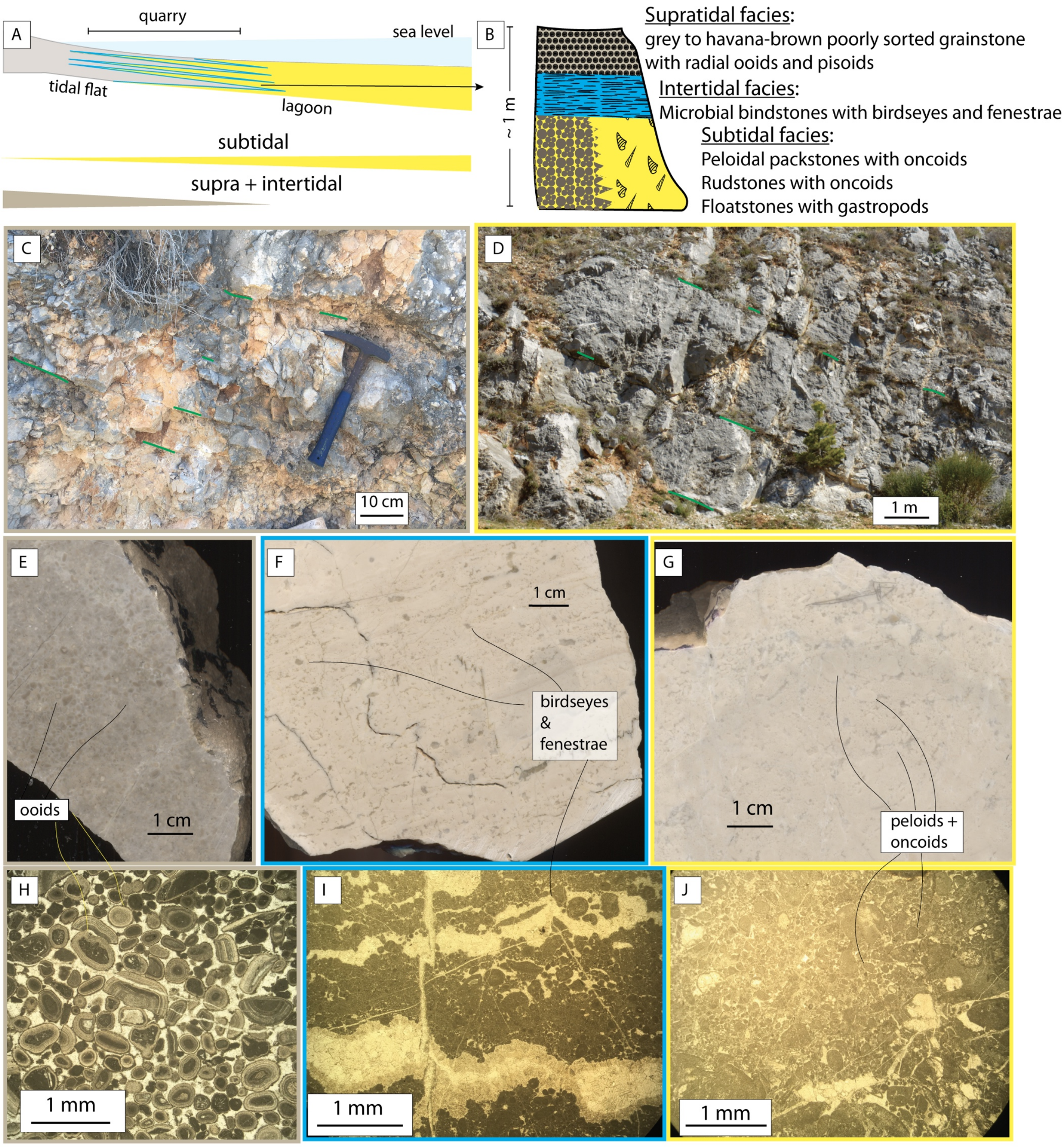

Figure 1.2 - Lithological characterization of the damage zone host rock. (A) Cartoon representing the hypothesized depositional environment of the limestones in the quarry: the transition between a tidal flat and a lagoon carbonate platform environment. The carbonates are organized in peritidal cycles reflecting the variation of accommodation space. The subtidal facies content increases moving toward the lagoon environment. (B) Representation of an ideal peritidal cycle with the associated carbonate facies. (C) Where the supratidal and intertidal content is high, the limestones crop out in centimetric to decimetric beds. (D) Bed thickness can be > 1 m when the subtidal facies predominates. (E-J): scans (E-G) and optical micrographs at plane polarized light (H-I) of samples pertaining to the supratidal (E, H), intertidal (F, I), and subtidal (G, J) carbonate facies.

4.3. Methods

We characterized the fracture distribution in the quarry using data acquired at different scales of observations (from millimetric to decametric) and from various techniques. Classical field techniques (scan-lines; Fig. 4.3; Priest and Hudson, 1981) were combined with modern approaches, such as extraction of fracture properties from digital images obtained from high-resolution scans of rock samples (Fig. 4.4) and from a virtual outcrop model (Fig. 4.5). In the following we present the methodology employed to extract fracture properties from scanlines (section 4.3.1), samples (section 4.3.2), and the virtual outcrop (section 4.3.3).

4.3.1. Scan-lines

We performed 26 scan-line surveys (see the example in Fig. 4.3) in the quarry area (see Section B1.1 for their location). The length, the position, and the orientation of the scan-lines were established in order to maximise their length and to maintain a sub-horizontal direction in irregular outcrops. The effective length and the orientation of each scanline is reported in Table B5.1. The effective length of the scan-line surveys was calculated by subtracting the portions of the outcrop hidden by vegetation to their total length. For each scanline survey we collected the trace lengths and the orientations of all the fractures (mostly joints, minor shear fractures, and rare veins) intersecting the

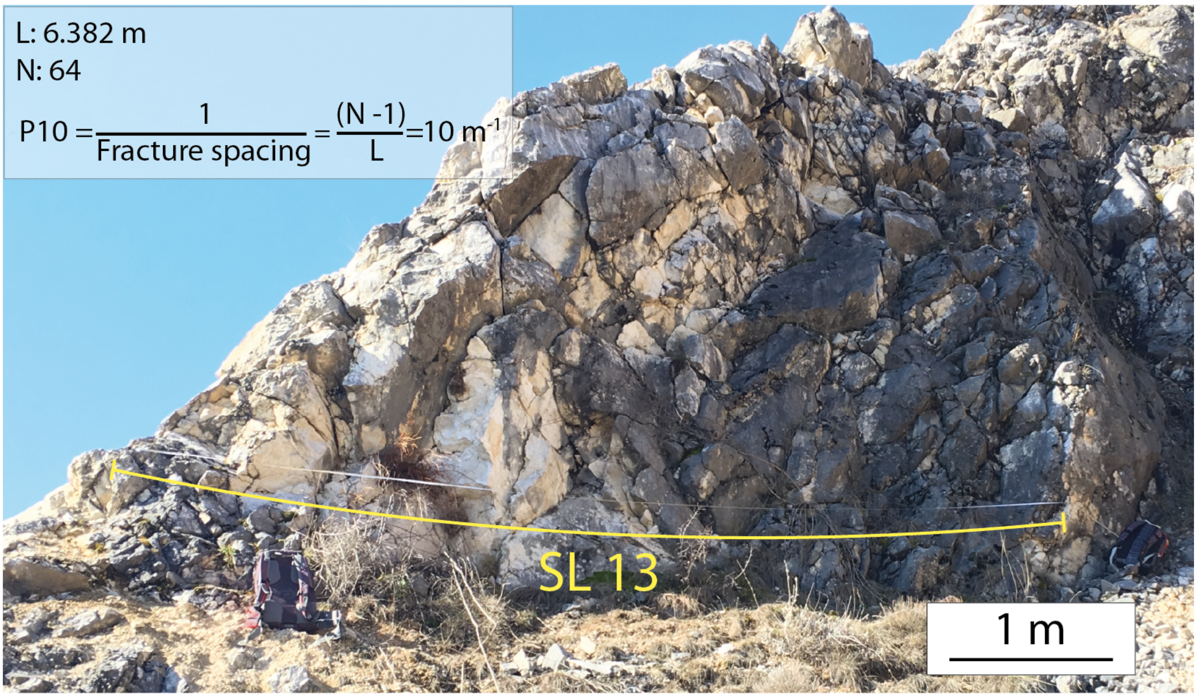

Figure 4.3 - Scanlines. Example of a scanline survey (SL13, see Section. B1 for the location) and linear fracture frequency calculation. L: scanline length; N: number of fractures intercepted by the scanline; P10: linear fracture frequency.

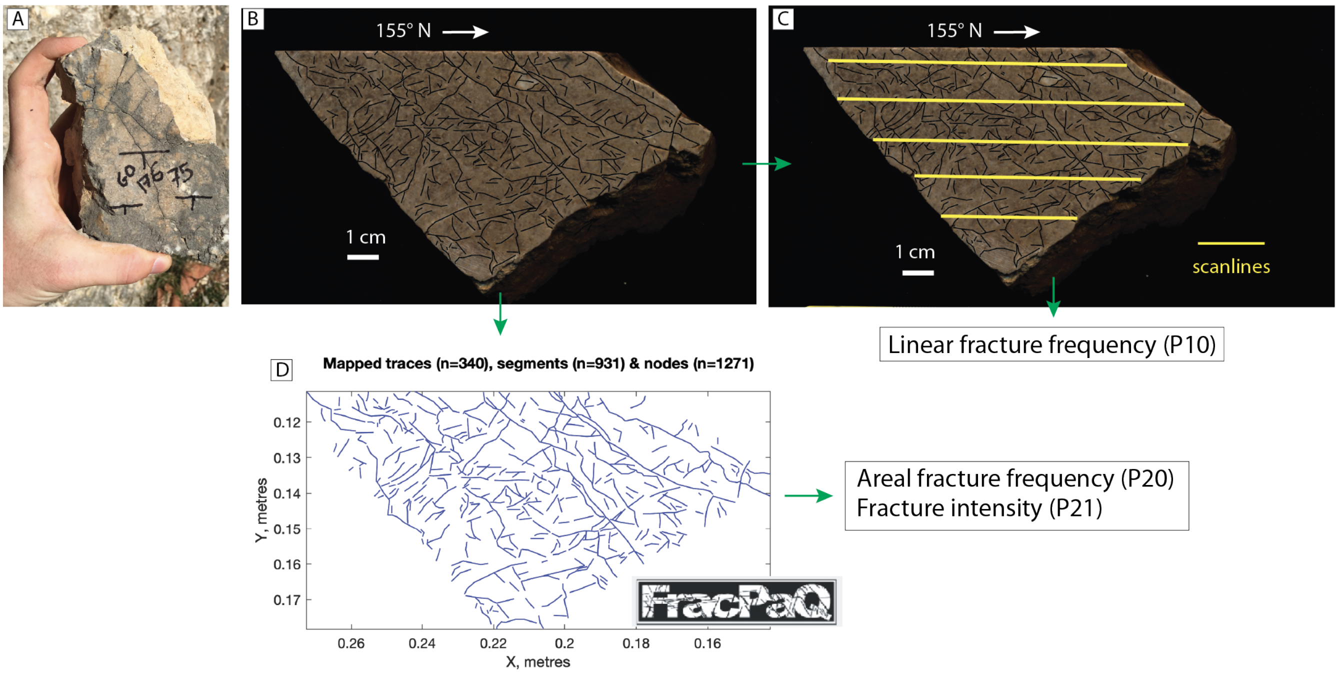

Figure 4.4 - Fracture analysis on the oriented samples. (A) An example of oriented rock sample. (B) 27 oriented samples, such as the one in panel A, have been collected and cut along vertical sections striking parallel to the main fault dip (i.e., ~155° N). Fracture traces have been digitized on a high-resolution scan of the sample (dark blue lines). (C) The linear fracture frequency has been calculated by counting the fracture traces sampled by sub-horizontal scanlines (yellow lines). (D) Other fracturing parameters such as areal fracture frequency and fracture intensity have been calculated by using the FracPaQ software (Healy et al., 2017).

measuring tape. We calculated the mean fracture spacing by dividing the effective length of the scanline for (N-1), where N is the number of fractures intercepted by the scan-line. The linear fracture frequency, or P10 (Sanderson and Nixon, 2015), was calculated as the reciprocal of the mean spacing (Fig. 4.3). Finally, we assigned a carbonate facies to each scanline through a visual inspection in the field (Table B5.1). For this purpose, we considered the intertidal facies together with the supratidal one.

4.3.2. Samples

27 oriented hand-samples (Fig. 4.4a) were collected, mostly in the same locations as the scanlines (section B1.2). Oriented samples were cut along vertical sections striking ~ 155° N (i.e., parallel to the main fault dip), polished, and scanned at a 1200 dpi resolution. Fracture traces were digitized using a commercial vector graphic software (Fig. 4.4b). For each sample, we evaluated the fracture spacing, the linear and areal fracture frequency (P10 and P20 respectively; Sanderson and Nixon, 2015), and fracture intensity (P21; Sanderson and Nixon, 2015). The spacing and the linear fracture frequency (P10), were calculated by tracing a series of sub-parallel scanlines on each sample (Fig. 4.4c), and following the same procedure adopted for the "regular" scan-lines (section 4.3.1). The others

fracture properties were extracted using the FracPaQ (v. 2.4) Matlab tool (Fig. 4.4d; Healy et al., 2017). This software takes a .svg file containing the polylines of fracture traces as input, and, according to the parameters inserted by the user, calculates the fracturing properties mentioned above. We refer the reader to the paper of (Healy et al., 2017) for a complete description of the algorithms used by the FracPaQ software. For each sample, we inserted the appropriate pixel/m ratio, in order to obtain the outputs in unit length (Healy et al., 2017). Furthermore, a carbonate facies was assigned to each sample by visual inspection. In addition, we evaluated the fracture permeability of each sample by using FracPaQ (Healy et al., 2017). We refer the reader to section B4 for the details on the methodology and the results. The lists of fracture parameters obtained are summarised in section B5.2.

4.3.3. Fracture analysis on the virtual outcrop

The photos used for the structure from motion algorithm were captured by an Unmanned Aerial Vehicle survey performed with an Aeromax X4 quadcopter equipped with a Sony Alpha 5000 camera (Fig. 4.5a). We collected 650 photos with an overlap of ~ 70% between adjacent pictures. The workflow we adopted to build the 3D model is very similar to that described by other authors (e.g., Tavani et al., 2014; Bistacchi et al., 2015; Bonali et al., 2019): photos were aligned through a semi-automatic identification of common points in adjacent pictures in order to create a point cloud. The point cloud is subsequently used to build a mesh and, finally, a textured mesh, that is the virtual outcrop (Fig. 4.5b). The virtual outcrop was scaled and georeferenced with respect to a previous terrestrial laser-scanner derived virtual outcrop (see Chapter 3). We constructed 6 ortho-mosaics (such as the one represented in Fig. 4.5c), with a resolution of 1 pixel per 1 cm, from the virtual outcrop, one for each quarry wall (labelled with capital letters in the inset in Fig. 4.6). We subdivided each orthomosaic into several squares with 5 m side length, to form virtual scan-areas (Fig. 4.5c, d). The location of all the virtual scan-areas is shown in Section B1.3. All the processing for the virtual outcrop and ortho-mosaic were executed within the 3DFlow Zephyr Aerial software. Each scan-area was manually interpreted in Adobe Illustrator® by drawing polylines, representing the traces of fractures, minor faults, and bedding (Fig. 4.5e), and polygons to map the supratidal and the intertidal facies (Fig. 4.5f). The supratidal and intertidal facies were recognized where cm to dm thick beds were visible. The fracture analysis was

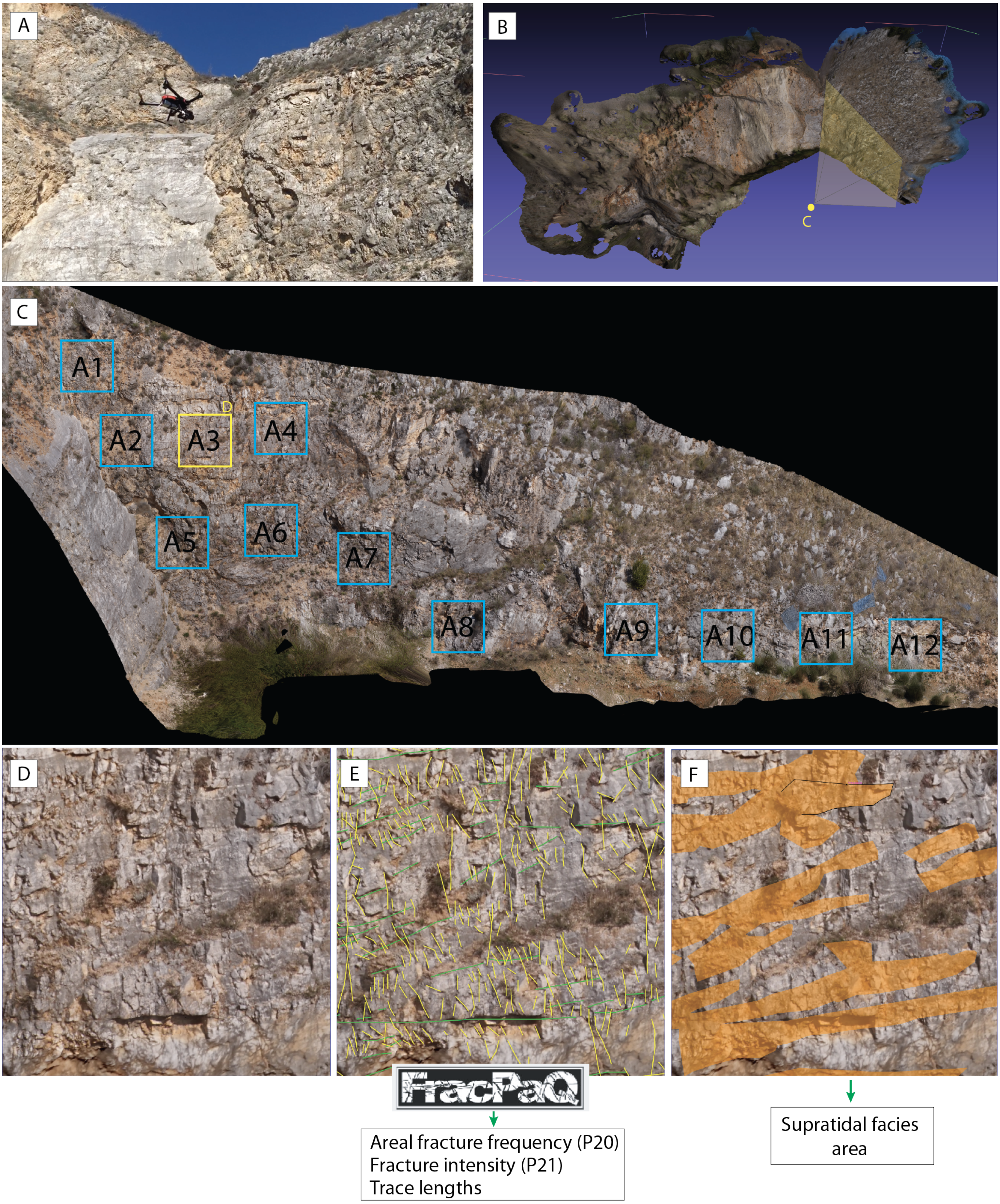

Figure 4.5 - Fracture analysis on the virtual outcrop. (A) An Unmanned Aerial Vehicle survey was performed to collect pictures from different points of view. (B) A virtual outcrop model of the quarry was obtained by a structure-from-motion processing. (C) A series of orthorectified panels with 1 mm per pixel resolution were extracted from the virtual outcrop model. (D) The virtual scan-area surveys were obtained by cutting the orthorectified panels (labelled with A1-12 in panel C) along squares with 5 m side length. (E, F) The orthorectified squares were interpreted by drawing fractures (yellow lines in panel E), bedding (green lines in panel E), and supratidal/intertidal carbonate facies (F). The fracture analysis was performed using FracPaQ software (Healy et al., 2017).

parameters as described in the previous section, to evaluate the areal fracture frequency (P20), fracture intensity (P21), and trace length. We also evaluated the minimum content of supratidal and intertidal facies in each scan-area by calculating their area in pixel^2 and dividing it by 250,000 px^2 (the scan-area). The results of the fracture analysis of each scan-area are reported in Section B5.3.

Finally, we captured 420 aerial photos using a Phantom 4 Pro quadcopter. The photos were processed using the same procedure described above to produce an aerial orthophoto of the quarry. This orthophoto was used as base map to check the position of all the georeferenced data we collected.

4.4. RESULTS

Fractures in the quarry are mainly joints and shear fractures. Calcite-filled veins are quite rare and, if present, can be appreciated only at the hand sample scale. Fractures are accompanied by at least 80 minor faults with various orientations and kinematics (Fig. 4.6; see Chapter 3 for further details). In this study we distinguish the minor faults from the shear fractures by the presence of a fault core. Fractures exhibit a centimetre- to a meter-scale trace-length, with modal values comprised between 10 and 50 cm (Section B2.1). The mean trace length calculated for each scanline is quite homogeneous in the whole quarry and is mostly everywhere smaller than 0.25 m (section B2.2). Virtual scan-areas suggest that the mean trace length is heterogeneous, with longer fractures located in the northern (trace lengths > 0.58 m) and in the western (0.46 m < trace length < 0.58 m) sectors of the quarry (B2.3). Most of the fractures are sub-vertical and E-W striking, while two minor clusters indicate the occurrence of sub-vertical fractures striking approximately NE-SW and N-S (stereoplot in Fig. 4.6).

Although the quarry is characterized by high fracture frequency values, both scanlines and virtual scan-area show similar fracture distribution patterns (Fig. 4.6). The portions of the quarry located immediately at the footwall of the front segment of the relay ramp are characterized by relatively low fracture frequency values (Fig. 4.6). On the SW side of the quarry (sectors E and F; see Fig. 4.6) the linear fracture frequency (P10) is lower than 25 m^{-1}, reaching a value of 10 m^{-1} close to front segment (for the scanline SL13; see B1.2 and B5.1), whilst the areal fracture frequency values (P20) are lower than 27 m^{-2}. The whole NE side of the quarry (sector A in B1.3) is characterized by relatively low fracture frequency values (Fig. 4.6); in this sector the linear fracture frequency is generally lower than 28 m^{-1}, although it locally reaches values higher than 38 m^{-1} near the front

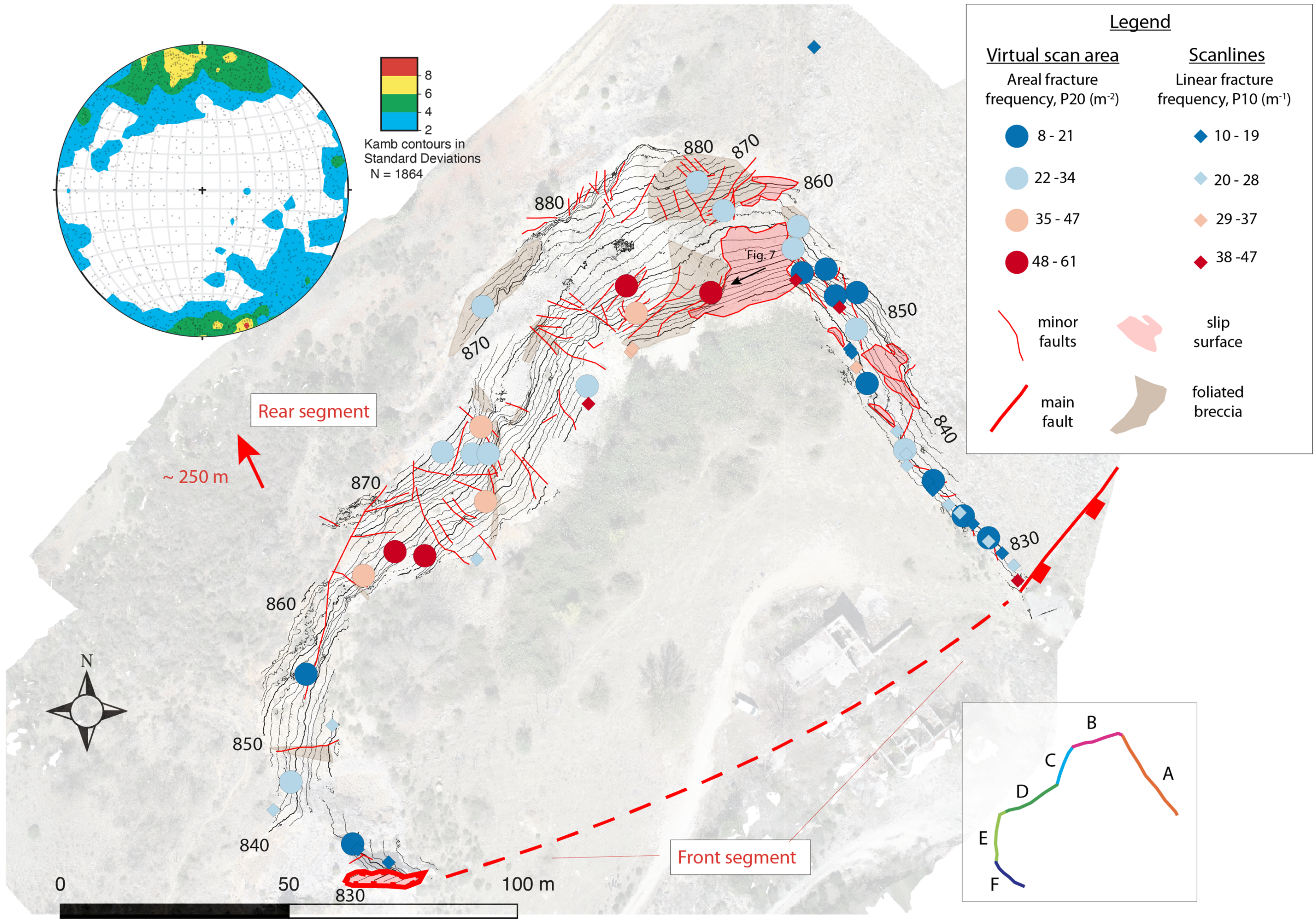

Figure 4.6 - Fracture frequency and geometry. Space distribution of the linear (diamonds, P10) and areal (circles, P20) fracture frequencies respectively measured along scanlines and obtained from virtual scan-areas. Fracture frequency is heterogeneously distributed, and both the methods highlight highest fracture frequencies far from the front segment of the main fault. In the same sectors we observe a higher number of minor faults and the local presence of foliated breccias. The minor faults traces are retrieved from Chapter 3. The stereoplot (Schmidt's net, low hemisphere) in the upper left shows a density contour plot of the poles to the fractures collected along the scanlines. The inset in the lower right shows the six quarry walls labelled with capital letters.

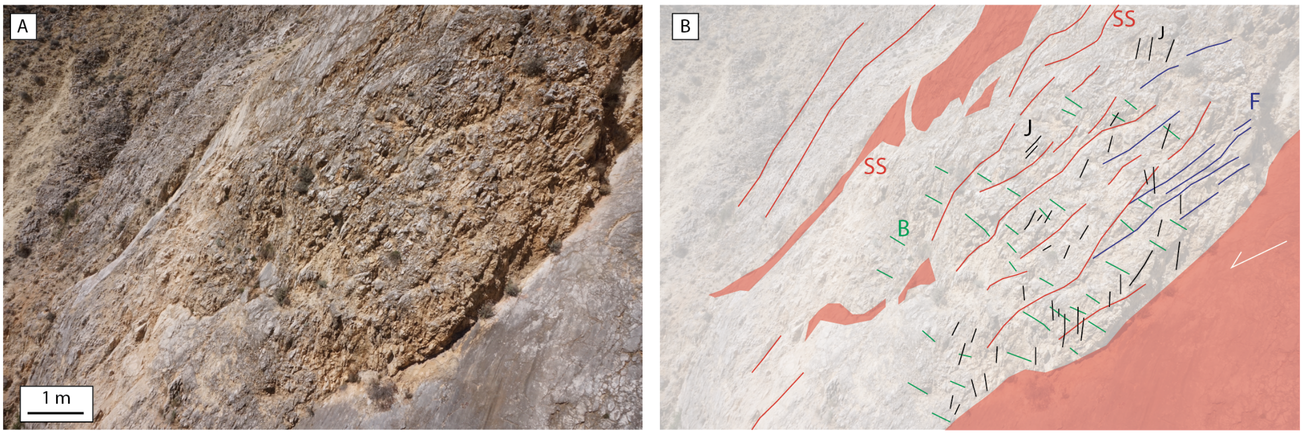

Figure 4.7 - Foliated breccias. Photo (A) and interpretation (B) of an exposure of foliated breccias. B: bedding, F: foliation, J: joints, SS: slip surfaces. The location of the photo is reported in Figure 4.6.

segment (for the scanline SL12; see B1.2 and B5.1). High linear fracture frequency values (P10 ≥ 39 m^{-1}) are also located far from the front segment (for scanlines SL21 and 22; see B1.2 and B5.1).

The areal fracture frequency is always smaller than 34 m^{-2} in the NE sector of the quarry. The portions of the quarry located far from the front segment of the relay ramp (sectors B, C, D; see Fig. 4.6) are characterized by the highest fracture frequencies. In detail the sectors B and D show areal fracture frequencies reaching values larger than 48 m^{-2}, up to 60 m^{-2}; Fig. 4.6, B5.3). Furthermore, the northern sector shows the highest concentration of minor faults (Fig. 4.6), that are often associated with foliated breccias (Fig. 4.6).

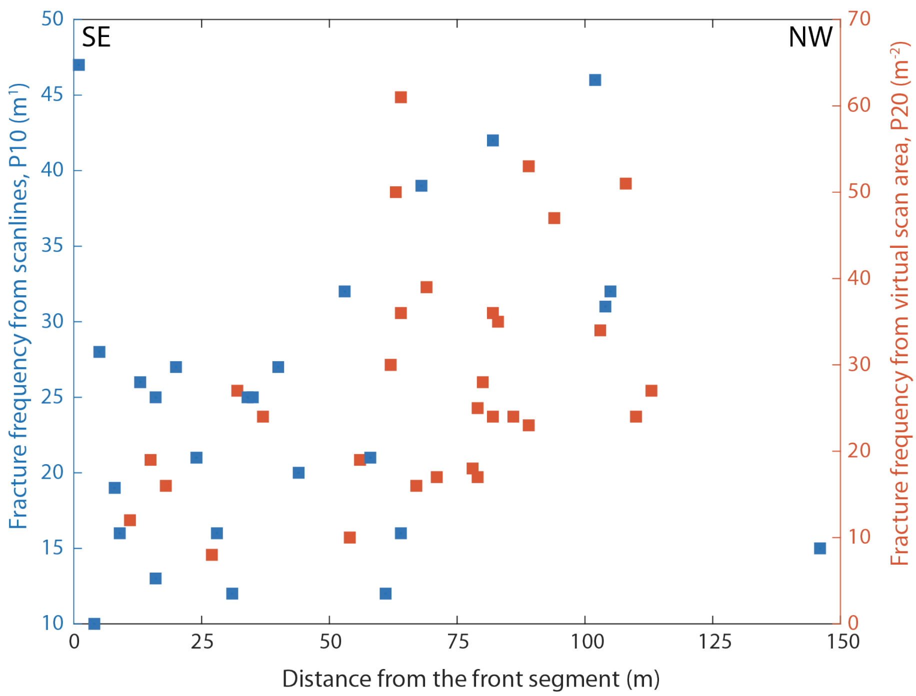

Figure 4.8 - Evolution of the linear and areal fracture frequency respectively measured through scanlines (blue) and virtual scan-areas (red). Fracture frequency increases moving away from the front segment.

Breccias are characterized by anastomosing foliations, consisting in undulated, sharp and striated slip surfaces, which are roughly parallel to the associated subsidiary faults (Fig. 4.7; see also Smeraglia et al., 2016). At hand-sample scale, the clasts are characterized by chaotic to crackle breccia textures (Woodcock and Mort, 2008; Smeraglia et al., 2016). The scan-area derived fracture intensity (P21) distribution mimics the distribution mentioned above (section B3.2).

In Figure 4.8 we show the variation in fracture frequency with the distance from the main fault in the quarry (i.e., the front segment of the relay ramp). Despite the high variability in fracture frequency for each fixed distance from the main fault, we recognize a slight fracture frequency increase moving away from the front segment (Fig. 4.8). This trend can be

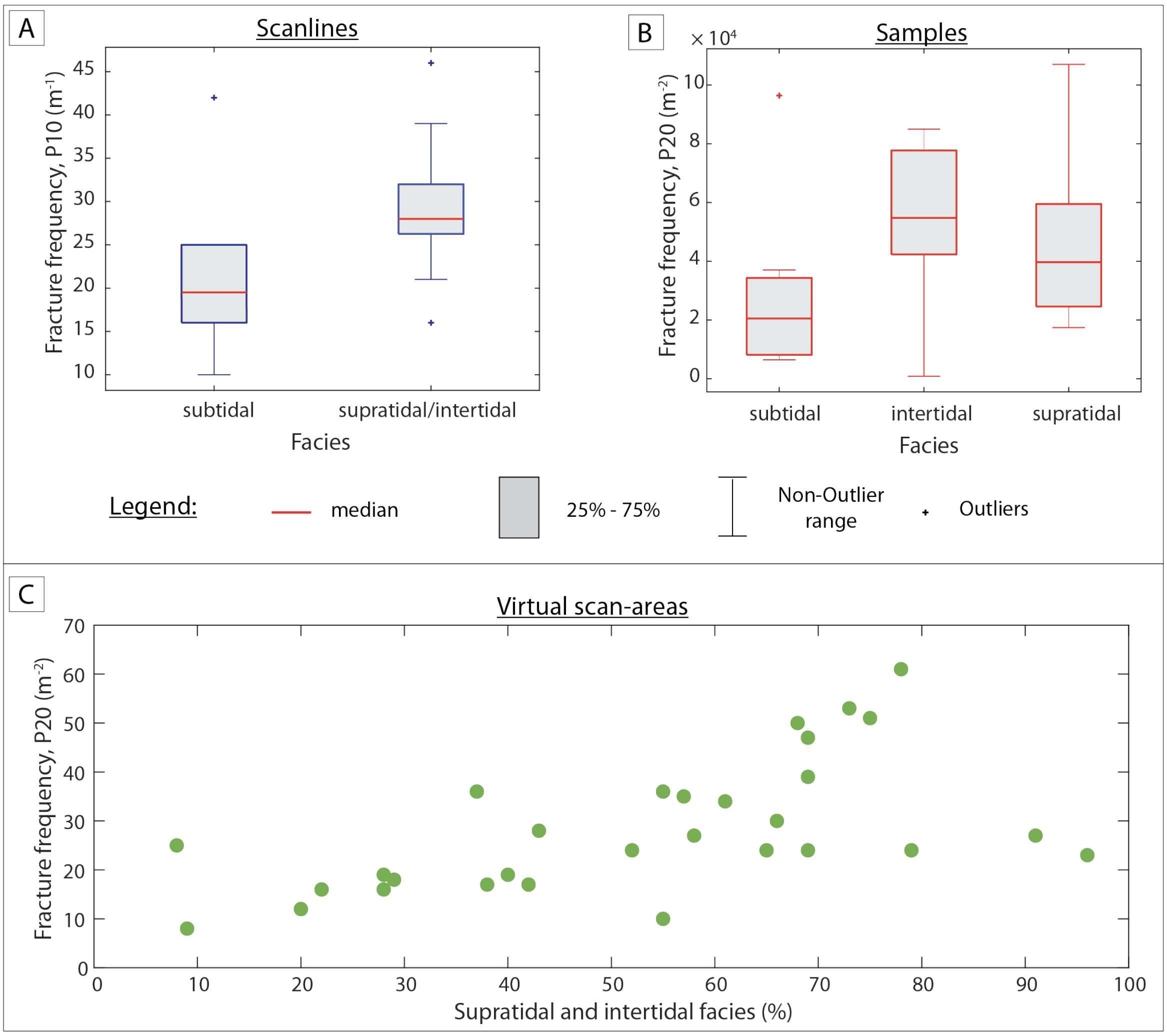

Figure 4.9 – Relationship between fracture frequency and carbonate facies from scanlines (A), oriented samples (B), and (C) virtual scan-areas. (A) Scanlines performed within supratidal and/or intertidal carbonate facies have a higher median of fracture frequency than those performed within subtidal facies. (B) The samples pertaining to the intertidal facies show a higher median of fracture frequency than supratidal and subtidal samples. (C) The areal fracture frequency measured through virtual scan-areas is directly proportional to the supratidal and intertidal facies content.

recognized from the data retrieved both from the virtual scan-areas and from scanlines (Fig. 4.8). Conversely, we do not observe any particular relationship between fracture frequency/intensity distribution and distance from the front segment from data retrieved from the oriented samples (section B3.1.4).

We observe that supratidal and intertidal carbonates are more fractured than subtidal carbonates both in scanlines and oriented samples (Fig. 4.9a,b). The median of the linear fracture frequency retrieved from scanlines measured in supratidal and intertidal facies (28 m^{-1}) is ~40 % larger than that measured in subtidal facies (20 m^{-1}) (Fig. 4.9a).

Intertidal and supratidal oriented samples show a mean areal fracture frequencies (P20) that are respectively 170 % (5.4×10^4 m^{-2}) and 100% (4.0×10^4 m^{-2}) higher than the subtidal samples (2.0×10^4 m^{-2}) (Fig. 4.9b). The relationship between fracture frequency and carbonate facies is even clearer in virtual scan-areas (Fig. 4.9c), where the areal fracture frequency increases with the supratidal and intertidal content (Fig. 4.9c). In detail, fracture frequency ranges between 10 m^{-2} and 30 m^{-2} for supratidal and intertidal content <50%, whilst it reaches ~ 60 m^{-2} where the percentage is ~ 80 %.

4.5. Discussion

4.5.1. Classical field techniques vs. virtual outcrop models

Our data show a consistent fracture distribution in the fault damage zone in both data retrieved from the scanlines and from the virtual scan areas (Figs. 4.6, 4.8). The strong similarity of results produced by classical field techniques such as scanlines (Priest and Hudson, 1981; Wu and Pollard, 1995) and by the virtual scan areas, further demonstrates the high potential of the virtual outcrops in structural geology (e.g., McCaffrey et al., 2005a, 2005b; Tavani et al., 2014; Bistacchi et al., 2015; Cawood et al., 2017). However, we do observe a small difference between the fracture trace length distribution computed from scanlines and virtual scan areas (Sect. B2.1). This discrepancy can be only partially attributed to the employment of a virtual outcrop. We believe that such a difference is due to two main biases. Firstly, scanlines are subjected to higher censoring effects (e.g., Priest and Hudson, 1981 among others) than virtual scan-areas. In fact, due to the vertical cliffs of the quarry, the sampling of vertical fractures longer than ~ 2 m - 3 m was impossible during most of the scanlines, whilst all the 5 m × 5 m virtual scan-areas allowed the collection of trace lengths smaller than 5 m. Secondly, scanlines allowed the collection of very small (< 10 cm) fractures that, despite their high resolution (1 cm per pixel), was quite impossible to identify in virtual scan-areas. The biases mentioned above produce a censoring of long fractures and oversampling of small fractures during scanlines, and this is evident when the histograms of trace lengths measured through the two methods are compared (B2.1).

The main advantage of using a virtual outcrop is the ability to collect fracture data on inaccessible or dangerous portions of the quarry. In this way we exploited most of the quarry walls surfaces for data collection (section B1.3), whilst only the base of the cliffs was analysed with scanlines for safety reasons (section B1.1). Since we manually interpreted the fractures, the employment of a virtual outcrop has not provided a consistent advantage in a matter of time efficiency. In fact, in addition to the generation of virtual outcrop model (photo acquisition and processing), which took about a week of work, the interpretation of each scan-area took approximately 2 hours, whilst the time needed for the data collection along a scanline in the field was ~2-3 hours. Despite the time requirements, the manual interpretation of fractures enabled us to preserve the interpretation ability of the user. In addition, the virtual scan-areas method enabled us to use the FracPaQ software (Healy et al., 2017) on the virtual outcrop models (Vinci et al., 2018; Giuffrida et al., 2019), which means that once interpretation is complete it is easy to extract a large number of fracture parameters. We believe that an important improvement in time-efficiency for the fracture analysis from virtual outcrops would be provided by the development of algorithms and workflows for the semi-automatic identification of fractures (e.g. Vasuki et al., 2014).

4.5.2. Fracture density distribution

The employment of scanlines allowed us to collect more than 1800 fracture attitudes (stereoplot in Fig. 4.6) that were used as a control on the fracture frequency distribution obtained from the virtual scan-areas. Fractures are mostly subvertical and strike in an E-W direction (± 20°). The pole to such an orientation is coherent with the Tre Monti fault kinematics (stereoplots in Fig. 4.1b and 4.1c). Other minors fracture sets strike NE-SW and NNW-SSE (Fig. 4.6).

Although many studies have demonstrated that the fracture frequency in the damage zone increases moving toward the main fault (Brock and Engelder, 1977; Wilson et al., 2003; Faulkner et al., 2006; Mitchell and Faulkner, 2009; Savage & Brodsky, 2011), for our case study both scanlines and

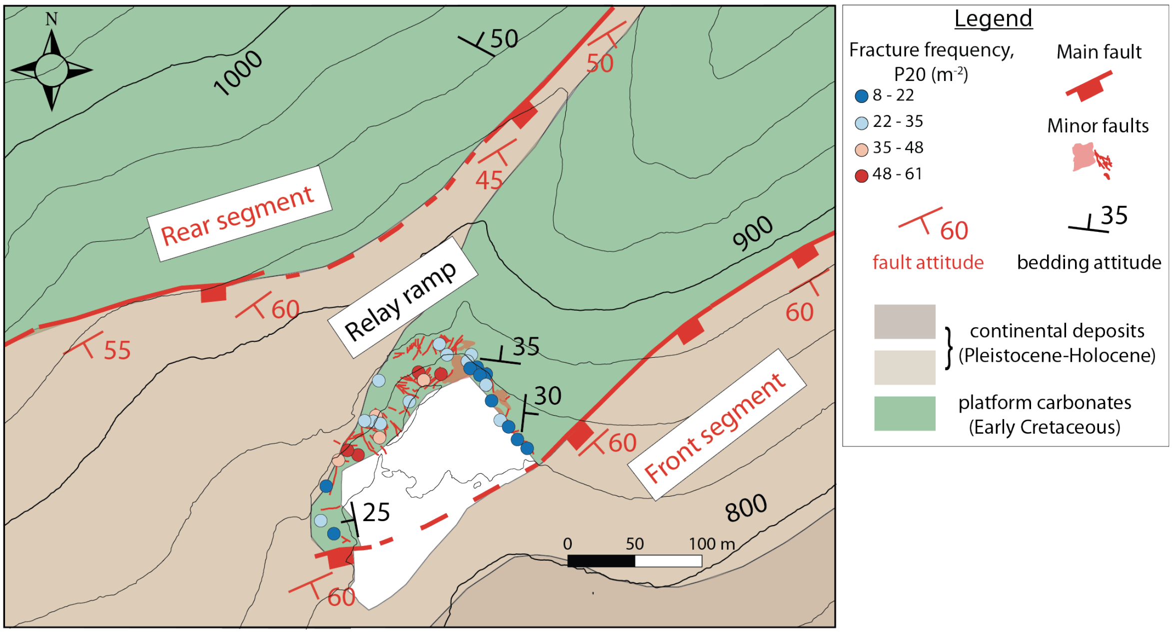

Figure 4.10 - Structural control on the fracture frequency. The quarry is located in the overlap zone between two right-stepping main fault strands defining a relay ramp environment. The fracture frequency increases approaching the centre of the relay ramp zone, i.e., moving from SE to NW in the quarry.

virtual scan-areas show that fracture frequency increases with distance away from the main fault plane, represented by the front segment of the relay ramp (i.e., moving from SE to NW; Figs. 4.6, 4.8). We interpret this unusual trend of fracture frequency as the result of two main factors. The first control is due the structural setting: an increase in number of minor faults and fractures (Figs. 4.6, 4.10, 4.11a) reflects the increasing interaction between the rear and the front fault approaching the relay zone (i.e., in the north-western sector; Fig. 4.10) (Fossen and Rotevatn, 2016; Peacock et al., 2017 and references therein). In this scenario, due to the direct relationship between the number of fractures and faults, the fracture distribution reflects the activity on the subsidiary faults (e.g., Shipton and Cowie, 2003).

The second important role on fracture distribution is played by carbonate facies. Approaching the centre of the relay zone we document an increase in supratidal/intertidal facies (Fig. 4.11) that are characterized by a higher fracture frequency (Fig. 4.9). We suggest two main causes for the more intense fracturing in supratidal/intertidal facies. Firstly, differential fracturing may be due to different petrophysical properties of the carbonate facies (i.e., different strength, or elasticity). Secondly, the supratidal/intertidal facies are characterized by thinner bedding (cm- to dm- scale) facilitating a larger fracture frequency (Ladeira and Price, 1981; Pollard and

Aydin, 1988; Huang and Angelier, 1989; Narr and Suppe, 1991; Wu and Pollard, 1995; Bai and Pollard, 2000). At the outcrop scale, the alternation of subtidal and intertidal/supratidal lithofacies is responsible for the formation of a mechanical stratigraphy in the quarry, with strongly fractured intervals confined in the

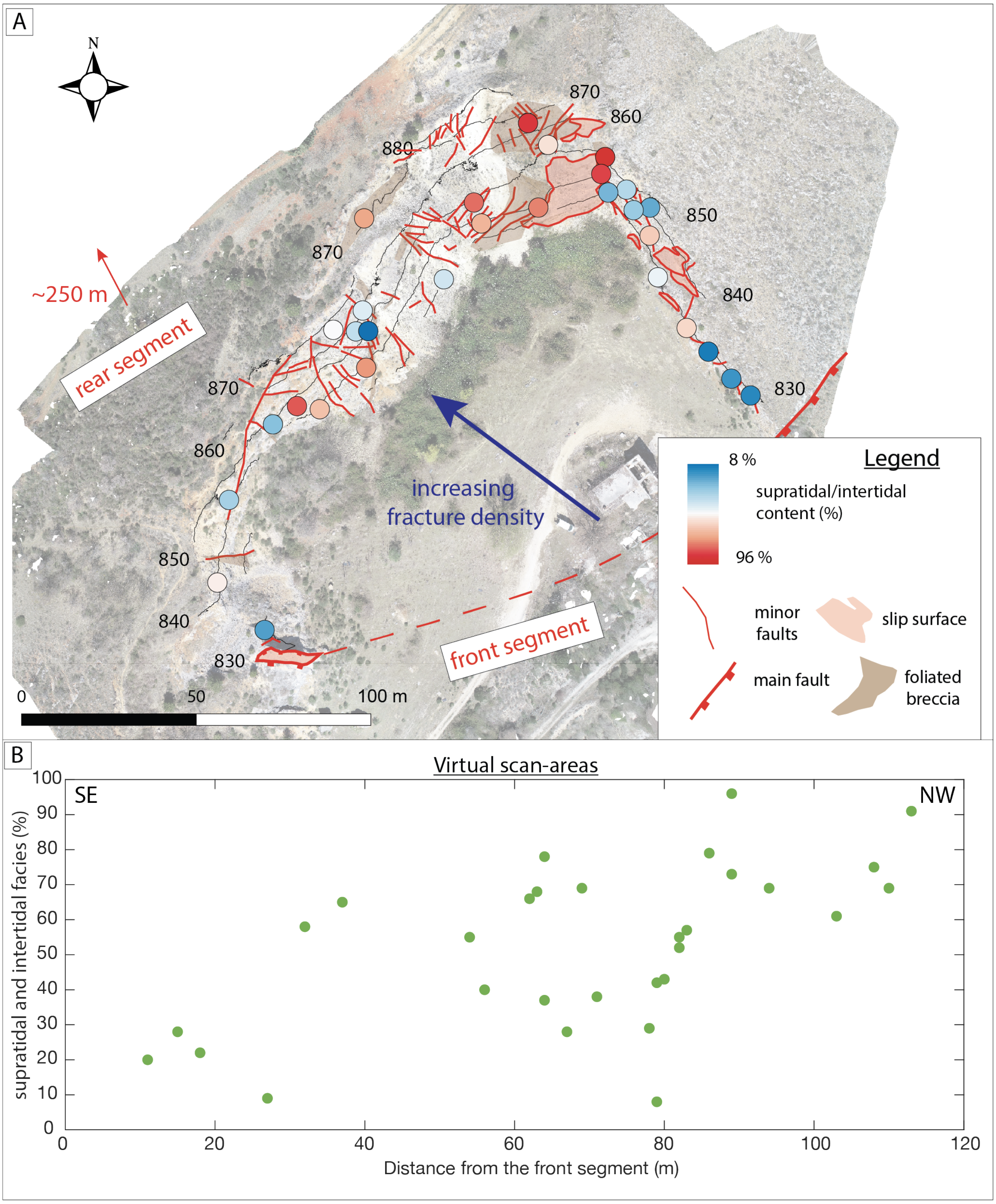

Figure 4.11 - Facies distribution in the quarry. (A) Map of the quarry showing the percentage of supratidal and intertidal carbonate facies measured in the virtual-scan areas. The supratidal and intertidal content is higher in the north-western sector of the quarry. High supratidal/intertidal facies contents are often accompanied by the development of foliated breccias. (B) The supratidal and intertidal carbonate facies content increases moving away from front segment (i.e. moving toward NW).

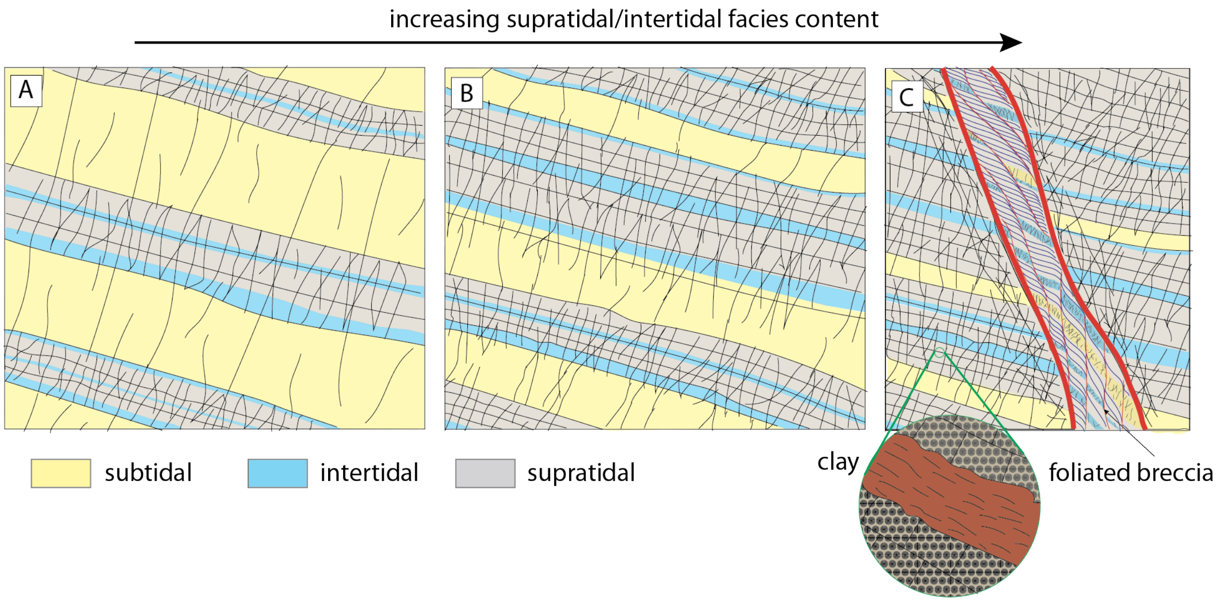

Figure 4.12 - Damage evolution versus supratidal and intertidal facies content. (A) The alternance of supratidal/intertidal and subtidal carbonate facies promotes a mechanical stratigraphy. The higher fracture intensity observed in the supratidal and intertidal facies can be related to smaller thickness of the beds (cm- to dm-thick, whilst the subtidal facies is characterized by m-thick beds) and to the development of compartmentalized fractures. The supratidal portions can contain small amount of clay minerals. (B) The average fracture intensity increases with increasing supratidal/intertidal content for a fixed sampling area (C) Foliated breccias can eventually develop in portions of the quarry dominated by the supratidal facies. The fluid-assisted diffusion mass transfer mechanisms, responsible for the development of the foliated breccia can be promoted in the supratidal facies by the high surface vs. area ratio of the small clasts produced by fracturing, and by the presence of small amount of clay.

supratidal/intertidal facies beds (Fig. 4.12a,b; see also Fig. 4.5e-f). Several authors have shown that carbonate facies can control fracture spacing in shallow-water limestones because of the different Dunham's texture (Wennberg et al., 2006; Larsen et al., 2010b) or different mechanical properties (e.g., Rustichelli et al., 2016). In particular, Wennberg and co-authors (2006) show that carbonate facies can be even more important than the mechanical layer thickness if the interbeds are strong (e.g., absence of a well-developed bedding). Our results highlight that in shallow-water limestones carbonate facies can control fracture spacing also by determining the bed thickness.

4.5.3. Deformation style

The relative content of supratidal/intertidal facies plays an important role also in the deformation style developed in the damage zone. In fact, the presence of the foliated breccias is always restricted to the portions of the quarry that are characterized by high supratidal/intertidal facies content (Fig. 11a). We suggest that during the fault activity, the high fracturing within the supratidal/intertidal facies increased permeability, favoring the influx of fluids into these portions of the relay zone. Fluids reacted with the fine grains within the fractured rocks promoting fluid-assisted dissolution and precipitation mass transfer processes (i.e., pressure-solution; Rutter, 1983; Gratier et al., 1999; Collettini et al., 2019). Furthermore, small amounts of clay minerals, that are present in the supratidal facies due to brief sedimentary episodes of subaerial exposure and karstification (Strasser et al 1999; Fig. 4.12a), may concentrate within S planes of the foliated breccias and further enhance pressure-solution (Gratier et al., 1999; Renard et al., 2001).

Our results highlight that fracture distribution within a relay ramp damage zone hosted in carbonate platform limestones can be very complex and not easily predictable. Beside the structural control played by the interaction between the fault segments bordering the relay ramp, a non-negligible role is played by carbonate facies. We suggest that both of these factors should be strongly considered during fluid flow modelling within relay ramps hosted in shallow water limestones.

4.6. Conclusions

We evaluated the fracture distribution and its controlling factors within a relay ramp damage zone hosted in shallow water limestones. Combining classical (i.e., scanlines) and modern (i.e., virtual scan-areas) techniques, we have shown that fracture frequency increases moving toward the center of the relay zone. Two main factors can explain such trend:

1) The increasing interaction between the front and the rear fault moving toward the centre of the relay zone leads to an increase in the number of subsidiary faults and their associated damage zones.

2) The content in supratidal and intertidal carbonate facies increases toward the centre of the relay zone. All the employed techniques show that supratidal and intertidal carbonate facies are characterized by higher fracture frequencies than the subtidal carbonates.

To conclude, our results highlight that fracture distribution patterns with respect the main faults are not easily predictable within a relay ramp, because they can be modulated by the subsidiary faults formation and slip during the relay ramp development. Moreover, carbonate facies may play a non-negligible role in fracture distribution within fault zones hosted in shallow water carbonates. Our results therefore provide important suggestions for factors controlling fracture distribution and fluid flow within relay ramps hosted by shallow water limestones.

ACKNOWLEDGEMENTS

We thank Billy Andrews, Sabina Bigi, Carolina Giorgetti, Luca Smeraglia, Marco Scuderi, Telemaco Tesei and Fabio Trippetta for fruitful discussions, Damiano Steri for his help during the aero-photogrammetry survey, and Domenico (Mimmo) Mannetta for his help during rock samples cutting and polishing and for high-quality thin sections preparation. We acknowledge 3DFlow for providing the Education License of Zephyr Aerial. MM also thanks Manuel Curzi, Roberta Ruggieri and Lavinia Squadrilli for their help in the fieldwork and Marta Della Seta for her help with the QGIS software. This research was supported by the Sapienza University of Rome Earth Sciences Department Ph.D. funds and Sapienza Progetti di Ateneo 2017 to EC.

REFERENCES

Allmendinger, R.W., Cardozo, N. & Fisher, D.M., (2011). Structural Geology Algorithms: Vectors and Tensors. Cambridge University Press.

Anders, M.H. & Wiltschko, D.V. (1994). Microfracturing, paleostress and the growth of faults. *Journal of Structural Geology* 16, 795–815.

Aydin, A. (2000). Fractures, faults, and hydrocarbon entrapment, migration and flow. *Marine and petroleum geology*, *17*(7), 797-814.

Bai, T. & Pollard, D.D. (2000). Closely spaced fractures in layered rocks: initiation mechanism and propagation kinematics. *Journal of Structural Geology* 22, 1409–1425.

Bastesen, E. & Rotevatn, A. (2012). Evolution and structural style of relay zones in layered limestone–shale sequences: insights from the Hammam Faraun Fault Block, Suez rift, Egypt. *Journal of the Geological Society*, 169(4), 477-488.

Bellian, J.A., Kerans, C. & Jennette, D.C. (2005). Digital Outcrop Models: Applications of Terrestrial Scanning Lidar Technology in Stratigraphic Modeling. *Journal of Sedimentary Research* 75, 166–176.

Bemis, S.P., Micklethwaite, S., Turner, D., James, M.R., Akciz, S., Thiele, S.T. & **Bangash, H.** (2014). Ground-based and UAV-Based photogrammetry: A multi-scale, high-resolution mapping tool for structural geology and paleoseismology. *Journal of Structural Geology* 69, 163–178.

Benedetti, L., Manighetti, I., Gaudemer, Y., Finkel, R., Malavieille, J., Pou, K., Arnold, M., Aumaître, G., Bourlès, D. & **Keddadouche, K.** (2013). Earthquake synchrony and clustering on Fucino faults (Central Italy) as revealed from in situ 36Cl exposure dating. *Journal of Geophysical Research: Solid Earth* 118, 4948–4974.

Bense, V.F., Gleeson, T., Loveless, S.E., Bour, O., & **Scibek, J.** (2013). *Fault zone hydrogeology. Earth-Science Reviews* 127, 171–192.

Berg, S.S. & **Skar, T.** (2005). Controls on damage zone asymmetry of a normal fault zone: outcrop analyses of a segment of the Moab fault, SE Utah. *Journal of Structural Geology* 27, 1803–1822.

Bigi, S., Battaglia, M., Alemanni, A., Lombardi, S., Campana, A., Borisova, E., & **Loizzo, M.** (2013). CO2 flow through a fractured rock volume: Insights from field data, 3D fractures representation and fluid flow modeling. International *Journal of Greenhouse Gas Control* 18, 183–199.

Bistacchi, A., Balsamo, F., Storti, F., Mozafari, M., Swennen, R., Solum, J., Tueckmantel, C., & **Taberner, C.** (2015). Photogrammetric digital outcrop reconstruction, visualization with textured surfaces, and three-dimensional structural analysis and modeling: Innovative methodologies applied to fault-related dolomitization (Vajont Limestone, Southern Alps, Italy). *Geosphere* 11, 2031–2048.

Bonali, F.L., Tibaldi, A., Marchese, F., Fallati, L., Russo, E., Corselli, C., & **Savini, A.** (2019). UAV-based surveying in volcano-tectonics: An example from the Iceland rift. *Journal of Structural Geology* 121, 46–64.

Brock, W.G. & **Engelder, T.** (1977). Deformation associated with the movement of the Muddy Mountain overthrust in the Buffington window, southeastern Nevada. *GSA Bulletin* 88, 1667–1677.

Caine, J.S., **Evans, J.P.** & **Forster, C.B.** (1996). Fault zone architecture and permeability structure. *Geology* 24, 1025–1028.

Carminati, E., **Lustrino, M.**, **Cuffaro, M.**, & **Doglioni, C.** (2010). Tectonics, magmatism and geodynamics of Italy: What we know and what we imagine. *Journal of the Virtual Explorer* 36.

Casini, G., **Hunt, D.**, **Monsen, E.**, & **Bounaim, A.** (2016). Fracture characterization and modeling from virtual outcrops. *AAPG Bulletin* 100, 41–61.

Cavinato, G.P. & **De Celles, P.G.** (1999). Extensional basins in the tectonically bimodal central Apennines fold-thrust belt, Italy: response to corner flow above a subducting slab in retrograde motion. *Geology* 27, 955–958.

Cawood, A.J., **Bond, C.E.**, **Howell, J.A.**, **Butler, R.W.**, & **Totake, Y.** (2017). LiDAR, UAV or compass-clinometer? Accuracy, coverage and the effects on structural models. *Journal of Structural Geology* 98, 67–82.

Centamore, E., **Crescenti, U.**, & **Dramis, F.** (2006). Note Illustrative della Carta Geologica d'Italia alla scala 1:50.000. Foglio 368, Avezzano.

Chester, F.M., **Evans, J.P.**, & **Biegel, R.L.** (1993). Internal structure and weakening mechanisms of the San Andreas fault. *Journal of Geophysical Research* 98, 771–786.

Chester, F. & **Logan, J.**, (1986). Implications for mechanical properties of brittle faults from observations of the Punchbowl fault zone, California. *Pure and Applied Geophysics* 124, 79–106.

Chiaraluce, L. (2012). Unravelling the complexity of Apenninic extensional fault systems: A review of the 2009 L'Aquila earthquake (Central Apennines, Italy). *Journal of Structural Geology* 42, 2–18.

Chiaraluce, L., **Di Stefano, R.**, **Tinti, E.**, **Scognamiglio, L.**, **Michele, M.**, **Casarotti, E.**, **...** & **Lombardi, A.** (2017). The 2016 central Italy seismic sequence: A first look at the mainshocks, aftershocks, and source models. *Seismological Research Letters*, *88*(3), 757-771.

Çiftci, B. & **Bozkurt, E.** (2007). Anomalous stress field and active breaching at relay ramps: a field example from Gediz Graben, SW Turkey. *Geological Magazine* 144, 687–699.

Collettini, C., **Tesei, T.**, **Scuderi, M.M.**, **Carpenter, B.M.**, & **Viti, C.** (2019). Beyond Byerlee friction, weak faults and implications for slip behavior. *Earth and Planetary Science Letters* 519, 245–263.

Colomina, I. & **Molina, P.** (2014). Unmanned aerial systems for photogrammetry and remote sensing: A review. ISPRS *Journal of Photogrammetry and Remote Sensing* 92, 79–97.

Corradetti, A., **Tavani, S.**, **Parente, M.**, **Iannace, A.**, **Vinci, F.**, **Pirmez, C.**, **Torrieri, S.**, **Giorgioni, M.**, **Pignalosa, A.**, & **Mazzoli, S.** (2017). Distribution and arrest of vertical through-going joints in a seismic-scale carbonate platform exposure (Sorrento peninsula, Italy): insights from integrating field survey and digital outcrop model. *Journal of Structural Geology*.

Cosentino, D., **Cipollari, P.**, **Marsili, P.**, & **Scrocca, D.** (2010). Geology of the central Apennines: a regional review. *Journal of the virtual explorer*, *36*(11), 1-37.

Cowie, P., **Phillips, R.**, **Roberts, G.**, **McCaffrey, K.**, **Zijerveld, L.**, **Gregory, L.**, **Walker, F.J.**, **Wedmore, L.**, **Dunai, T.**, **Binnie, S.**, **Freeman, S.**, **Wilcken, K.**, **Shanks, R.**, **Huismans, R.**, **Papanikolaou, I.**, **Michetti, A.**, & **Wilkinson, M.** (2017). Orogen-scale uplift in the central Italian Apennines drives episodic behaviour of earthquake faults. *Scientific Reports* 7, 44858.

D'Agostino, N., **Giuliani, R.**, **Mattone, M.**, & **Bonci, L.** (2001a). Active crustal extension in the Central Apennines (Italy) inferred from GPS measurements in the interval 1994–1999. *Geophysical Research Letters* 28, 2121–2124.

D'Agostino, N., **Jackson, J.**, **Dramis, F.**, & **Funiciello, R**. (2001b). Interactions between mantle upwelling, drainage evolution and active normal faulting: an example from the central Apennines (Italy). *Geophysical Journal International* 147, 475–497.

D'Argenio, B., **Ferreri, V.**, **Amodio, S.**, & **Pelosi, N.** (1997). Hierarchy of high-frequency orbital cycles in Cretaceous carbonate platform strata. *Sedimentary Geology*, 113(3-4), 169-193.

De Paola, N., **Collettini, C.**, **Faulkner, D. R.**, & **Trippetta, F.** (2008). Fault zone architecture and deformation processes within evaporitic rocks in the upper crust. *Tectonics*, *27*(4).

Destro, N. (1995). Release fault: A variety of cross fault in linked extensional fault systems, in the Sergipe-Alagoas Basin, NE Brazil. *Journal of Structural Geology* 17, 615–629.

Devoti, R., Pietrantonio, G., Pisani, A. R., Riguzzi, F., Serpelloni, E., Beltrando, M., ... & Doglioni, C. (2010). Present day kinematics of Italy. *Journal of the Virtual Explorer*, *36*(2)

Doglioni, C. (1991). A proposal for the kinematic modelling of W dipping subductions possible applications to the Tyrrhenian Apennines system. *Terra Nova* 3, 423–434.

Dor, O., Ben-Zion, Y., Rockwell, T., & Brune, J. (2006a). Pulverized rocks in the Mojave section of the San Andreas Fault Zone. *Earth and Planetary Science Letters* 245, 642–654.

Dor, O., Rockwell, T., & Ben-Zion, Y. (2006b). Geological Observations of Damage Asymmetry in the Structure of the San Jacinto, San Andreas and Punchbowl Faults in Southern California: A Possible Indicator for Preferred Rupture Propagation Direction. *Pure and Applied Geophysics* 163, 301–349.

Faulkner, D., Mitchell, T., Healy, D., & Heap, M., (2006). Slip on "weak" faults by the rotation of regional stress in the fracture damage zone. *Nature* 444.

Fossen, H., Johansen, T. E. S., Hesthammer, J., & Rotevatn, A. (2005). Fault interaction in porous sandstone and implications for reservoir management; examples from southern Utah. *AAPG bulletin*, *89*(12), 1593-1606.

Fossen, H. & Rotevatn, A. (2016). Fault linkage and relay structures in extensional settings—A review. *Earth-Science Reviews* 154, 14–28.

Galadini, F. & Galli, P. (1999). The Holocene paleoearthquakes on the 1915 Avezzano earthquake faults (central Italy): implications for active tectonics in the central Apennines. *Tectonophysics* 308, 143–170.

Giuffrida, A., Agosta, F., Rustichelli, A., Panza, E., La Bruna, V., Eriksson, M., ... & Giorgioni, M. (2019). Fracture stratigraphy and DFN modelling of tight carbonates, the case study of the Lower Cretaceous carbonates exposed at the Monte Alpi (Basilicata, Italy). *Marine and Petroleum Geology*, 104045.

Gratier, J.-P., Renard, F. & Labaume, P. (1999). How pressure solution creep and fracturing processes interact in the upper crust to make it behave in both a brittle and viscous manner. *Journal of Structural Geology* 21, 1–9.

Gudmundsson, A., Berg, S.S., Lyslo, K.B., & Skurtveit, E. (2001). Fracture networks and fluid transport in active fault zones. *Journal of Structural Geology* 23, 343–353.

Gudmundsson, A., Simmenes, T.H., Larsen, B., & Philipp, S.L. (2010). Effects of internal structure and local stresses on fracture propagation, deflection, and arrest in fault zones. *Journal of Structural Geology* 32, 1643–1655.

Healy, D., Rizzo, R.E., Cornwell, D.G., Farrell, N., Watkins, H., Timms, N.E., Gomez-Rivas, E., & Smith, M. (2017). FracPaQ: A MATLAB™ toolbox for the quantification of fracture patterns. *Journal of Structural Geology* 95, 1–16.

Huang, Q., & Angelier, J. (1989). Fracture spacing and its relation to bed thickness. *Geological Magazine*, *126*(4), 355-362.

Kattenhorn, S., Aydin, A., & Pollard, D. (2000). Joints at high angles to normal fault strike: an explanation using 3-D numerical models of fault-perturbed stress fields. *Journal of Structural Geology* 22, 1–23.

Kim, Y.-S., Peacock, D., & Sanderson, D. (2004). Fault damage zones. *Journal of Structural Geology* 26, 503–517.

Ladeira, F.L. & Price, N.J. (1981). Relationship between fracture spacing and bed thickness. *Journal of Structural Geology* 3.

Larsen, B, Grunnaleite, I., & Gudmundsson, A. (2010a). How fracture systems affect permeability development in shallow-water carbonate rocks: An example from the Gargano Peninsula, Italy. *Journal of Structural Geology* 32, 1212–1230.

Larsen, B, Gudmundsson, A., Grunnaleite, I., Sælen, G., Talbot, M.R., & Buckley, S.J. (2010b). Effects of sedimentary interfaces on fracture pattern, linkage, and cluster formation in peritidal carbonate rocks. *Marine and Petroleum Geology* 27, 1531–1550.

McCaffrey, K., Holdsworth, R., Imber, J., Clegg, P., Paola, N., Jones, R., Hobbs, R., Holliman, N., & Trinks, I. (2005a). Putting the geology back into Earth models. *Eos, Transactions American Geophysical Union* 86, 461–466.

McCaffrey, K.J.W., Jones, R.R., Holdsworth, R.E., Wilson, R.W., Clegg, P., Imber, J., Holliman, N., & Trinks, I. (2005b). Unlocking the spatial dimension: digital technologies and the future of geoscience fieldwork. *Journal of the Geological Society* 162, 927–938.

McGinnis, R.N., Ferrill, D.A., Morris, A.P., Smart, K.J., & **Lehrmann, D.** (2017). Mechanical stratigraphic controls on natural fracture spacing and penetration. *Journal of Structural Geology* 95, 160–170.

Mercuri, M., McCaffrey, K. J., Smeraglia, L., Mazzanti, P., Collettini, C., & **Carminati, E.** (2020). Complex geometry and kinematics of subsidiary faults within a carbonate-hosted relay ramp. *Journal of Structural Geology*, 130, 103915.

Michie, E., Haines, T., Healy, D., Neilson, J., Timms, N., & **Wibberley, C.** (2014). Influence of carbonate facies on fault zone architecture. *Journal of Structural Geology* 65, 82–99.

Miller, S.A., Collettini, C., Chiaraluce, L., Cocco, M., Barchi, M.R., & **Kaus, B.J.** (2004). Aftershocks driven by a high-pressure CO2 source at depth. *Nature* 427, 724–727.

Mitchell, T. M., Ben-Zion, Y., & **Shimamoto, T.** (2011). Pulverized fault rocks and damage asymmetry along the Arima-Takatsuki Tectonic Line, Japan. *Earth and Planetary Science Letters*, *308*(3-4), 284-297.

Mitchell, T.M. & **Faulkner, D.R.,** (2009). The nature and origin of off-fault damage surrounding strike-slip fault zones with a wide range of displacements: A field study from the Atacama fault system, northern Chile. *Journal of Structural Geology* 31, 802–816.

Morewood, N.C. & **Roberts, G.P.,** (2000). The geometry, kinematics and rates of deformation within an en échelon normal fault segment boundary, central Italy. *Journal of Structural Geology* 22, 1027–1047.

Narr, W. & **Suppe, J.,** (1991). Joint spacing in sedimentary rocks. *Journal of Structural Geology* 13, 1037–1048.

Nur, A. & **Booker, J.R.** (1972). Aftershocks Caused by Pore Fluid Flow? Sc*ience* 175, 885–887.

Odling, N. E., Gillespie, P., Bourgine, B., Castaing, C., Chiles, J. P., Christensen, N. P., ... & **Trice, R.** (1999). Variations in fracture system geometry and their implications for fluid flow in fractures hydrocarbon reservoirs. *Petroleum Geoscience*, *5*(4), 373-384.

Olariu, M.I., Ferguson, J.F., Aiken, C., & **Xu, X.** (2008). Outcrop fracture characterization using terrestrial laser scanners: Deep-water Jackfork sandstone at Big Rock Quarry, Arkansas. *Geosphere* 4, 247–259.

Osleger, D. (1991). Subtidal carbonate cycles: Implications for allocyclic vs. autocyclic controls. *Geology*, 19(9), 917-920.

Peacock, D. C. P., Dimmen, V., Rotevatn, A., & **Sanderson, D. J.** (2017). A broader classification of damage zones. *Journal of Structural Geology*, *102*, 179-192.

Peacock, D.C.P. & **Parfitt, E.A.** (2002). Active relay ramps and normal fault propagation on Kilauea Volcano, Hawaii. *Journal of Structural Geology* 24, 729–742.

Peacock, D.C.P., Price, S.P., Whitham, A.G., & **Pickles, C.S.** (2000). The World's biggest relay ramp: Hold With Hope, NE Greenland. *Journal of Structural Geology* 22, 843–850.

Peacock, D.C.P. & **Xing, Z.** (1994). Field examples and numerical modelling of oversteps and bends along normal faults in cross-section. *Tectonophysics* 234, 147–167.

Pless, J., McCaffrey, K., Jones, R., Holdsworth, R., Conway, A., & **Krabbendam, M.** (2015). 3D characterization of fracture systems using Terrestrial Laser Scanning: an example from the Lewisian basement of NW Scotland. *Geological Society, London, Special Publications* 421, 125–141.

Pollard, D.D. & **Aydin, A.A.** (1988). Progress in understanding jointing over the past century. *Geological Society of America Bulletin* 100, 1181–1204.

Priest, S.D. & **Hudson, J.A.** (1981). Estimation of discontinuity spacing and trace length using scanline surveys. *Int. J. Rock Mech. Min. Sci. & Geomech. Abstr* 18, 183–197.

Renard, F., Dysthe, D., Feder, J., Bjørlykke, K., & **Jamtveit, B.** (2001). Enhanced pressure solution creep rates induced by clay particles: Experimental evidence in salt aggregates. *Geophysical Research Letters*, *28*(7), 1295-1298.

Rotevatn, A., Fossen, H., Hesthammer, J., Aas, T., & **Howell, J.** (2007). Are relay ramps conduits for fluid flow? Structural analysis of a relay ramp in Arches National Park, Utah. *Geological Society, London, Special Publications* 270, 55–71.

Rustichelli, A., Torrieri, S., Tondi, E., Laurita, S., Strauss, C., Agosta, F., & **Balsamo, F.** (2016). Fracture characteristics in Cretaceous platform and overlying ramp carbonates: An outcrop study from Maiella Mountain (central Italy). *Marine and Petroleum Geology* 76, 68–87.

Rutter, E.H. (1983). Pressure solution in nature, theory and experiment. **Journal of the Geological Society** 140, 725–740.

Sanderson, D., Nixon, C. (2015). The use of topology in fracture network characterization *Journal of Structural Geology* 72, 55-66.

Savage, H., & **Brodsky, E.** (2011). Collateral damage: Evolution with displacement of fracture distribution and secondary fault strands in fault damage zones. **Journal of Geophysical Research: Solid Earth** (1978–2012) 116.

Scognamiglio, L., Tinti, E., Casarotti, E., Pucci, S., Villani, F., Cocco, M., Magnoni, F., Michelini, A., & **Dreger, D.** (2018). Complex Fault Geometry and Rupture Dynamics of the MW 6.5, 30 October 2016, Central Italy Earthquake. *Journal of Geophysical Research: Solid Earth* 123, 2943–2964.

Seers, T.D. & **Hodgetts, D.** (2016). Extraction of three-dimensional fracture trace maps from calibrated image sequences. Geosphere 12, 1323–1340.

Shipton, Z. K., & **Cowie, P. A.** (2003). A conceptual model for the origin of fault damage zone structures in high-porosity sandstone. *Journal of Structural Geology*, *25*(3), 333-344.

Shipton, Z.K. & **Cowie, P.A.** (2001). Damage zone and slip-surface evolution over μm to km scales in high-porosity Navajo sandstone, Utah. *Journal of Structural Geology* 23, 1825–1844

Sibson, R.H. (1994). Crustal stress, faulting and fluid flow. *Geological Society, London, Special Publications* 78, 69–84.

Sibson, R.H. (1996). Structural permeability of fluid-driven fault-fracture meshes. *Journal of Structural Geology* 18, 1031–1042.

Smeraglia, L., Berra, F., Billi, A., Boschi, C., Carminati, E., & **Doglioni, C.** (2016). Origin and role of fluids involved in the seismic cycle of extensional faults in carbonate rocks. *Earth and Planetary Science Letters* 450, 292–305.

Smeraglia, L., Billi, A., Carminati, E., Cavallo, A., Di Toro, G., Spagnuolo, E., & **Zorzi, F.** (2017). Ultra-thin clay layers facilitate seismic slip in carbonate faults. *Scientific Reports* 7, 974.

Smith, S.A., Billi, A., Di Toro, G., & **Spiess, R.** (2011). Principal Slip Zones in Limestone: Microstructural Characterization and Implications for the Seismic Cycle (Tre Monti Fault, Central Apennines, Italy). *Pure and Applied Geophysics* 168, 2365–2393.

Strasser, A., Pittet, B., Hillgartner, H. & **Pasquier, J.-B.** (1999) Depositional sequences in shallow carbonate-dominated sedimentary systems: concepts for a high-resolution analysis. *Sedimentary Geology*, *128*(3-4), 201-221.

Tavani, S., Granado, P., Corradetti, A., Girundo, M., Iannace, A., Arbués, P., Muñoz, J.A., & **Mazzoli, S.,** (2014). Building a virtual outcrop, extracting geological information from it, and sharing the results in Google Earth via OpenPlot and Photoscan: An example from the Khaviz Anticline (Iran). *Computers & Geosciences* 63, 44–53.

Tavani, S., Storti, F., Salvini, F., & **Toscano, C.,** (2008). Stratigraphic versus structural control on the deformation pattern associated with the evolution of the Mt. Catria anticline, Italy. *Journal of Structural Geology* 30, 664–681.

Telling, J., Lyda, A., Hartzell, P., & **Glennie, C.** (2017). Review of Earth science research using terrestrial laser scanning. *Earth-Science Reviews*, *169*, 35-68.

Townend, J., & **Zoback, M.D.** (2000). How faulting keeps the crust strong. *Geology*, *28*(5), 399-402

Vasuki, Y., Holden, E.-J., Kovesi, P., & **Micklethwaite, S.** (2014). Semi-automatic mapping of geological Structures using UAV-based photogrammetric data: An image analysis approach. *Computers & Geosciences* 69, 22–32.

Vinci, F., Tavani, S., Iannace, A., Parente, M., Pirmez, C., Torrieri, S., Giorgioni, M., Pignalosa, A., & **Mazzoli, S.** (2018). Extracting and quantifying fracture patterns from a reservoir-scale Virtual Outcrop Model. *Geophysical Research Abstracts.*

Volatili, T., Zambrano, M., Cilona, A., Huisman, H., Rustichelli, A., Giorgioni, M., Vittori, S., & **Tondi, E.** (2019). From fracture analysis to flow simulations in fractured carbonates: The case study of the Roman Valley Quarry (Majella Mountain, Italy). *Marine and Petroleum Geology* 100, 95–110.

Wennberg, O., Svånå, T., Azizzadeh, M., Aqrawi, A., Brockbank, P., Lyslo, K., & **Ogilvie, S.** (2006). Fracture intensity vs. mechanical stratigraphy in platform top carbonates: the

Aquitanian of the Asmari Formation, Khaviz Anticline, Zagros, SW Iran. *Petroleum Geoscience* 12, 235–246.

Westoby, M.J., Brasington, J., Glasser, N.F., Hambrey, M.J., & **Reynolds, J.M.** (2012). 'Structure-from-Motion' photogrammetry: A low-cost, effective tool for geoscience applications. *Geomorphology* 179, 300–314.

Wilkinson, M.W., Jones, R.R., Woods, C.E., Gilment, S.R., McCaffrey, K.J.W., Kokkalas, S., & **Long, J.J.** (2016). A comparison of terrestrial laser scanning and structure-from-motion photogrammetry as methods for digital outcrop acquisition. *Geosphere* 12, 1865–1880.

Wilson, J., Chester, J., & **Chester, F.,** (2003). Microfracture analysis of fault growth and wear processes, Punchbowl Fault, San Andreas system, California. *Journal of Structural Geology* 25, 1855–1873.

Woodcock, N.H. & **Mort, K.** (2008). Classification of fault breccias and related fault rocks. *Geological Magazine* 145, 435–440.

Wu, H. & **Pollard, D.D.** (1995). An experimental study of the relationship between joint spacing and layer thickness. *Journal of Structural Geology* 17, 887–905.

5. Conclusions

In this thesis, different aspects of the carbonate-hosted faults structure and mechanics have been investigated. Rock mechanics experiments allowed me to highlight the role of normal stress and sliding velocity in the structure and mechanics of simulated carbonate-bearing principal slip zones.

High normal stress (σ_n > 20 MPa) and low slip velocities (v < 100 μm/s) promote the activation of pressure insensitive deformation mechanisms (pressure solution and granular plasticity), leading to the development of an anastomosed foliation coupled with grain indentations, cementation and folding within the simulated carbonate-bearing principal slip zones. The progressive contribution of pressure insensitive deformation mechanisms with increasing normal stress and decreasing slip velocity is mechanically coupled with a decrease in steady-state friction. Since the co-existence of pressure sensitive (cataclasis) and pressure insensitive deformation mechanisms is well-documented in natural carbonate-hosted faults exhumed from seismogenic depths, the results obtained in this thesis suggest that the pressure insensitive deformation mechanisms, particularly pressure-solution, can play a key-role in carbonate-hosted fault mechanics, facilitating the onset of slip.

The integration of traditional fieldwork and virtual outcrops allowed me to analyse the geometry and the kinematics of subsidiary faults, and the factors controlling fracture distribution, within a carbonate-hosted relay ramp damage zone.

The subsidiary faults show a high geometrical and kinematic complexity that cannot be explained by a single stress field. On the contrary, subsidiary faults record the local scale temporal interaction of multiple stress fields. An important role is played by the development of a local stress field, probably related to the interaction of the two main fault strands that border the relay ramp.

The interaction between the overlapping fault segments also affects the fracture distribution. In fact, an increase of fracture density and number of subsidiary faults with distance from the front segment of the relay ramp has been observed. Such a trend can be explained with the increase of secondary faults and associated damage zones approaching the centre of the relay ramp. A non-negligible role in fracture distribution is also played by the carbonate facies. In fact, supratidal and intertidal carbonates show a higher fracture density than subtidal facies and, at the same time, an increase in supratidal/intertidal facies with distance from the main fault has been observed. Since fracture density was proven to scale inversely with layer thickness, the thinner bedding (cm- to dm-thick beds) in intertidal/supratidal than the subtidal facies (m-thick beds), can play an important role in the lithological control on fracturing.

This thesis emphasizes the importance of friction experiments and virtual outcrops in structural geology studies dealing with fault zone structure and mechanics. On one hand, friction experiments enabled a direct comparison between microstructures and mechanics, allowing to assess the effect of pressure insensitive deformation processes on carbonate-faults mechanics. On the other hand, the employment of virtual outcrops allowed to (1) map structural features (e.g., minor faults) at very high scales (1:100 and higher), (2) collect an high number of structural measurements in a short period of time, (3) apply classical field techniques (e.g., scan-areas) in a more comfortable way and to inaccessible portions of the outcrop and, (4) to efficiently illuminate complex relationships (e.g., fracture density vs. carbonate facies).

Suggestions for further research

The results obtained in this thesis provide some suggestions for future work. Further insights on the stress field perturbation within a relay ramp and, more generally, on the minor fault geometry and kinematics within fault damage zones can be provided by the investigation of case studies simpler than the Tre Monti fault. It is worth noting that some mechanical complexity in the observed minor faults geometry and kinematics could have been indeed introduced by the release fault nature of the Tre Monti fault, which, although striking almost parallel to the direction of the regional extension, shows mostly dip-slip slickenlines. For example, the role exerted by the release fault nature of the Tre Monti fault can be evaluated by comparing our results with an analysis of a relay ramp within one of the NW-SE striking faults in the Fucino basin. Furthermore, the stress field perturbation caused by the relay ramp can be better quantified by the investigation of the minor fault geometry and kinematics on isolated segments of both the Tre Monti fault and NW-SE striking faults in the Fucino basin.

Other case studies can also help to better understand the role of carbonate facies in fracturing. For example, a case study where the same lithologies crops out far from a fault zone can help to discern the

lithological from the structural control in the fracture density pattern observed in chapter 4.
Moreover, triaxial experiments can be conducted on undeformed samples to illuminate eventual differences of strength and/or elastic moduli between the facies. These experiments would lead to discern the role played by layer thickness and/or different petrophysical properties on the lithological control on fracturing.
Finally, our preliminary approach to retrieve permeability from virtual scan-area using FracPaQ could be improved and extended to rock mechanics experiments. For example, the comparison between the permeability measured during the experiments with that computed using FracPaQ on the deformed rock samples would lead to better constrain the relationship between fracture parameters (aperture, length, connectivity, orientation, and density) and fluid flow.

Annex A: Supplementary material of Chapter 3

Supplementary material

Complex geometry and kinematics of subsidiary faults within a carbonate-hosted relay ramp

Marco Mercuri[1], Ken J. W. McCaffrey[2], Luca Smeraglia[1,3], Paolo Mazzanti[1,4], Cristiano Collettini, C.[1], and Eugenio Carminati[1]

1: Dipartimento di Scienze della Terra, Sapienza Università di Roma, Piazzale Aldo Moro 5, 00185, Rome, Italy

2: Earth Sciences Department, Durham University, South Road, Durham, DH1 3LE, UK

3: Laboratoire Chrono-Environnement, Université de Bourgogne Franche-Comté, Besançon, France

4: NHAZCA S.r.l., spin-off company University of Rome "Sapienza", Via Vittorio Bachelet 12, 00185 Rome, Italy

Under Review for *Journal of Structural Geology*

A1 – Bar chart representing the distribution of fault trace values measured from the Digital Outcrop Model

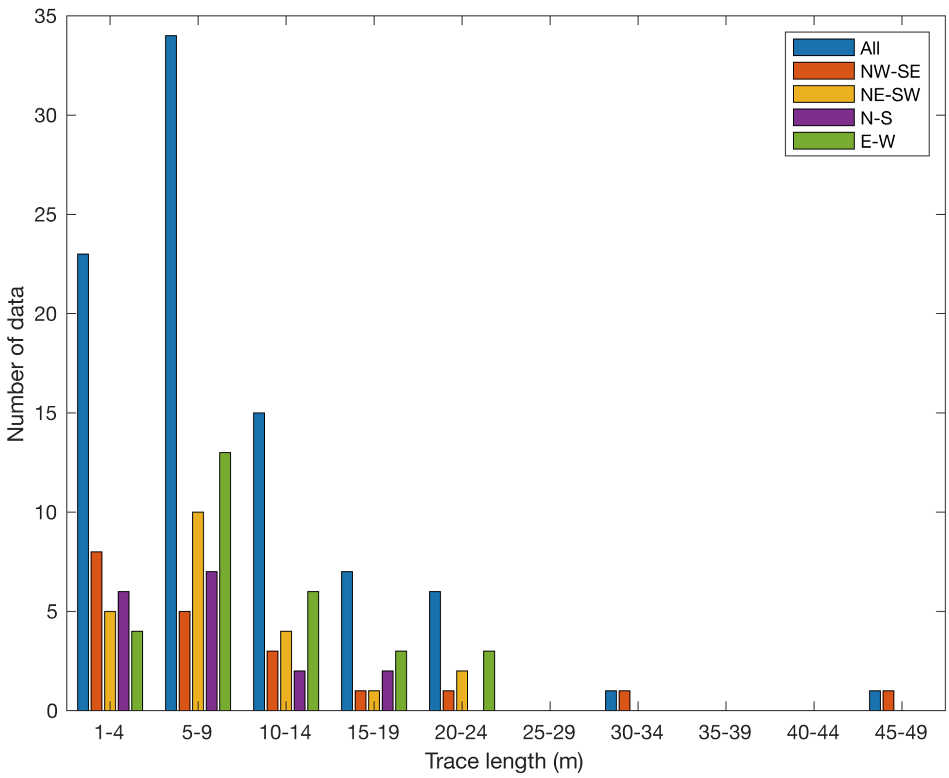

A2 – Histogram representing the distribution of Root Mean Squared (RMS) values for the polylines fitting with planes.

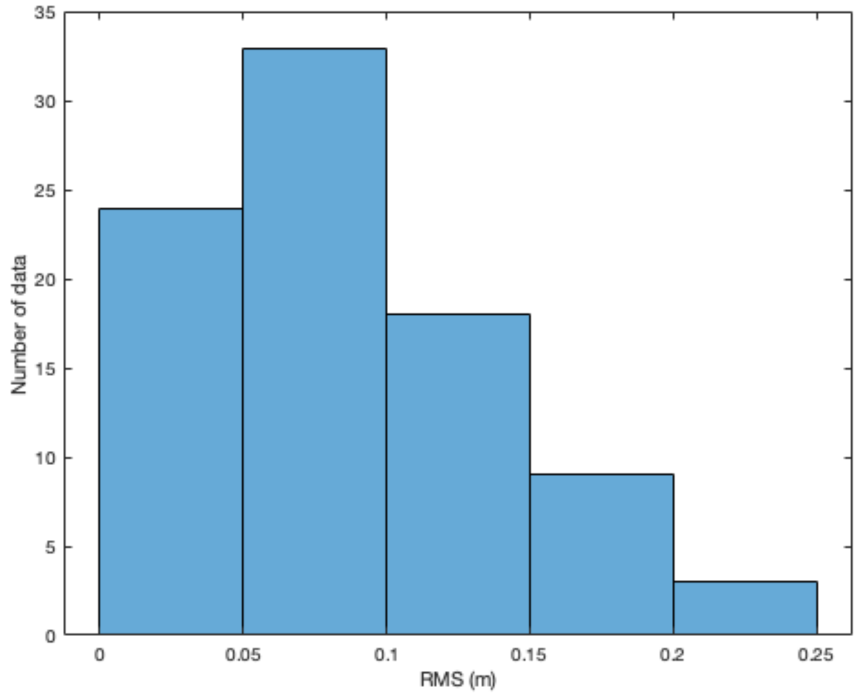

A3- Histogram representing the distribution of Root Mean Squared (RMS) vs. trace length values for the polylines fitting with planes.

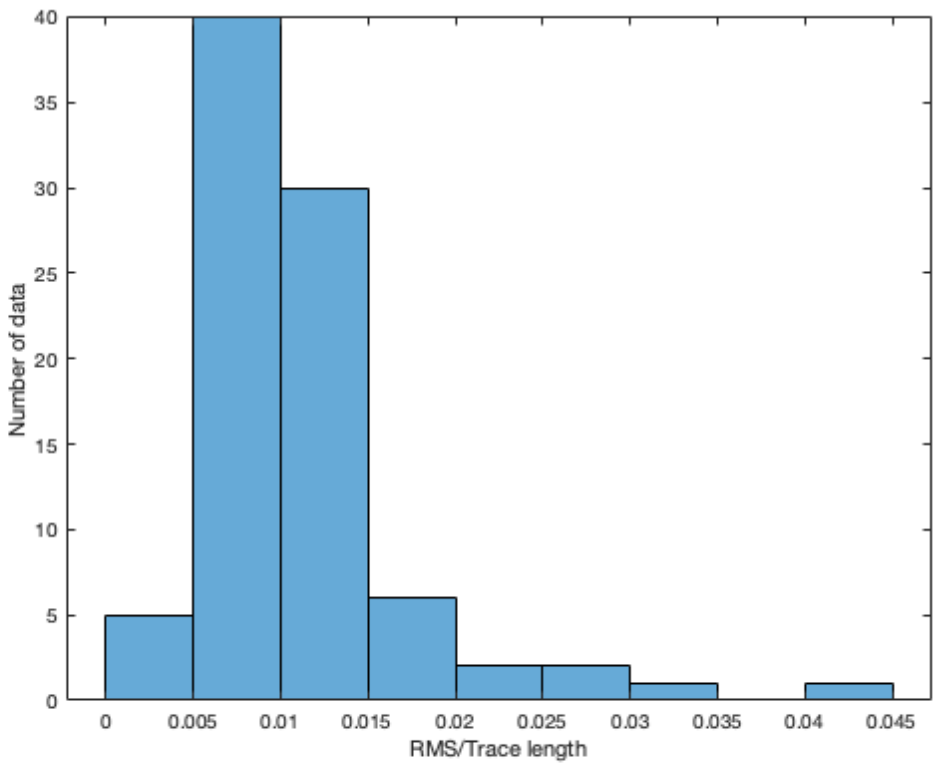

Annex B: Supplementary material of Chapter 4

Supplementary material

Lithological and structural control on fracture distribution within a carbonate-hosted relay ramp

Marco Mercuri[1], Eugenio Carminati[1], Maria Chiara Tartarello[1], Marco Brandano[1], Paolo Mazzanti[1,2], Luca Smeraglia[1,3], Ken J. W. McCaffrey[4], and Cristiano Collettini, C.[1]

1: Dipartimento di Scienze della Terra, Sapienza Università di Roma, Piazzale Aldo Moro 5, 00185, Rome, Italy

2: NHAZCA S.r.l., spin-off company University of Rome "Sapienza", Via Vittorio Bachelet 12, 00185 Rome, Italy

3: Laboratoire Chrono-Environnement, Université de Bourgogne Franche-Comté, Besançon, France

4: Earth Sciences Department, Durham University, South Road, Durham, DH1 3LE, UK

Auxiliary material for this manuscript contains:

- B1 – Locations of scanlines, sampling sites, and virtual scan area
- B2 – Trace length measurements
- B3 – Additional data on fracture frequency and intensity
- B4 – Preliminary results on permeability estimation
- B5 – Supplementary tables

B1 – Location of scanlines, sampling sites, and virtual scan area

In this section we show the distribution of the scanlines (B1.1), sites of oriented samples (B1.2), and virtual scan-areas (B1.3) in the quarry.

B1.1 -Locations and labels of scanlines

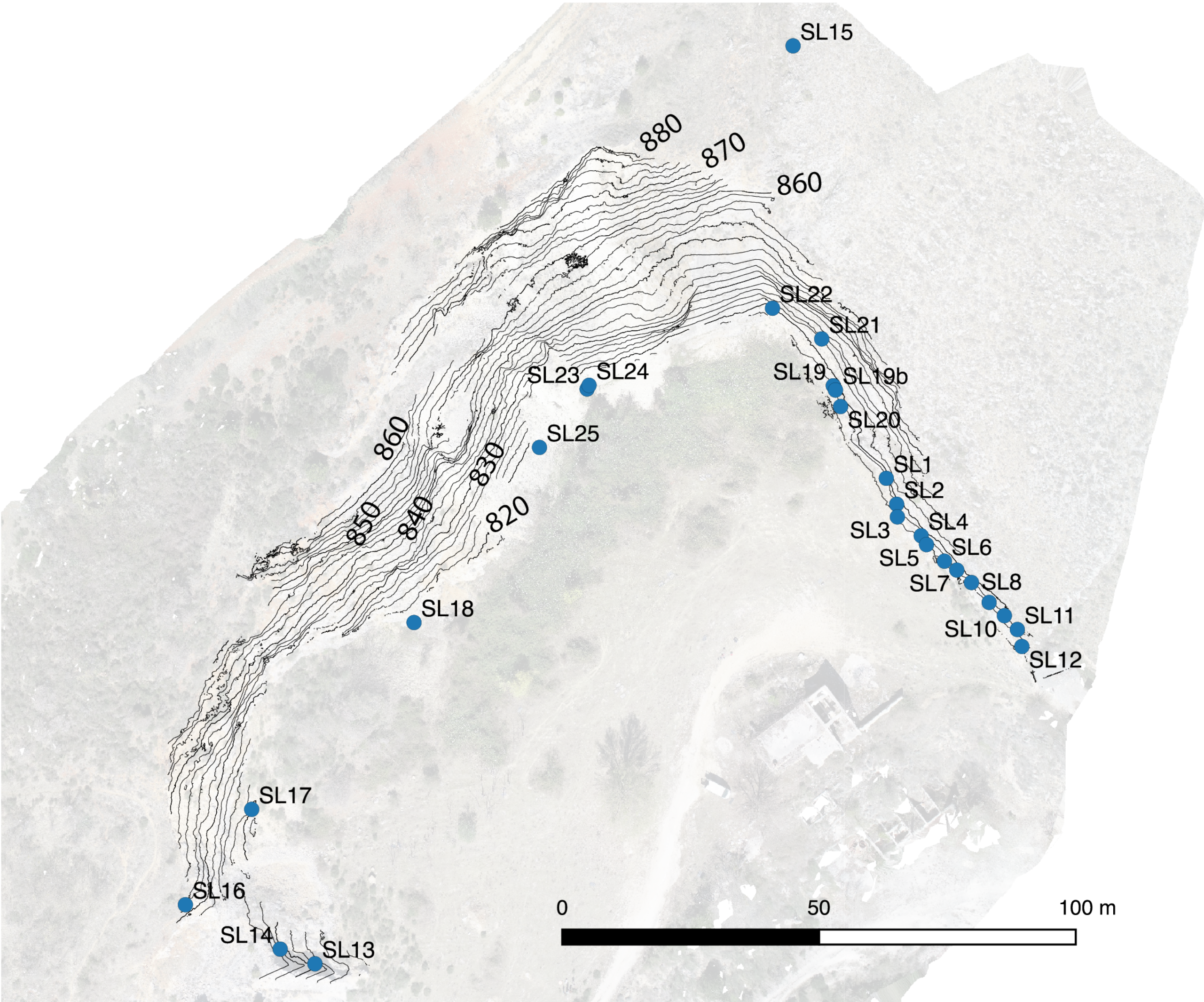

B1.2 -Locations and labels of oriented samples sites

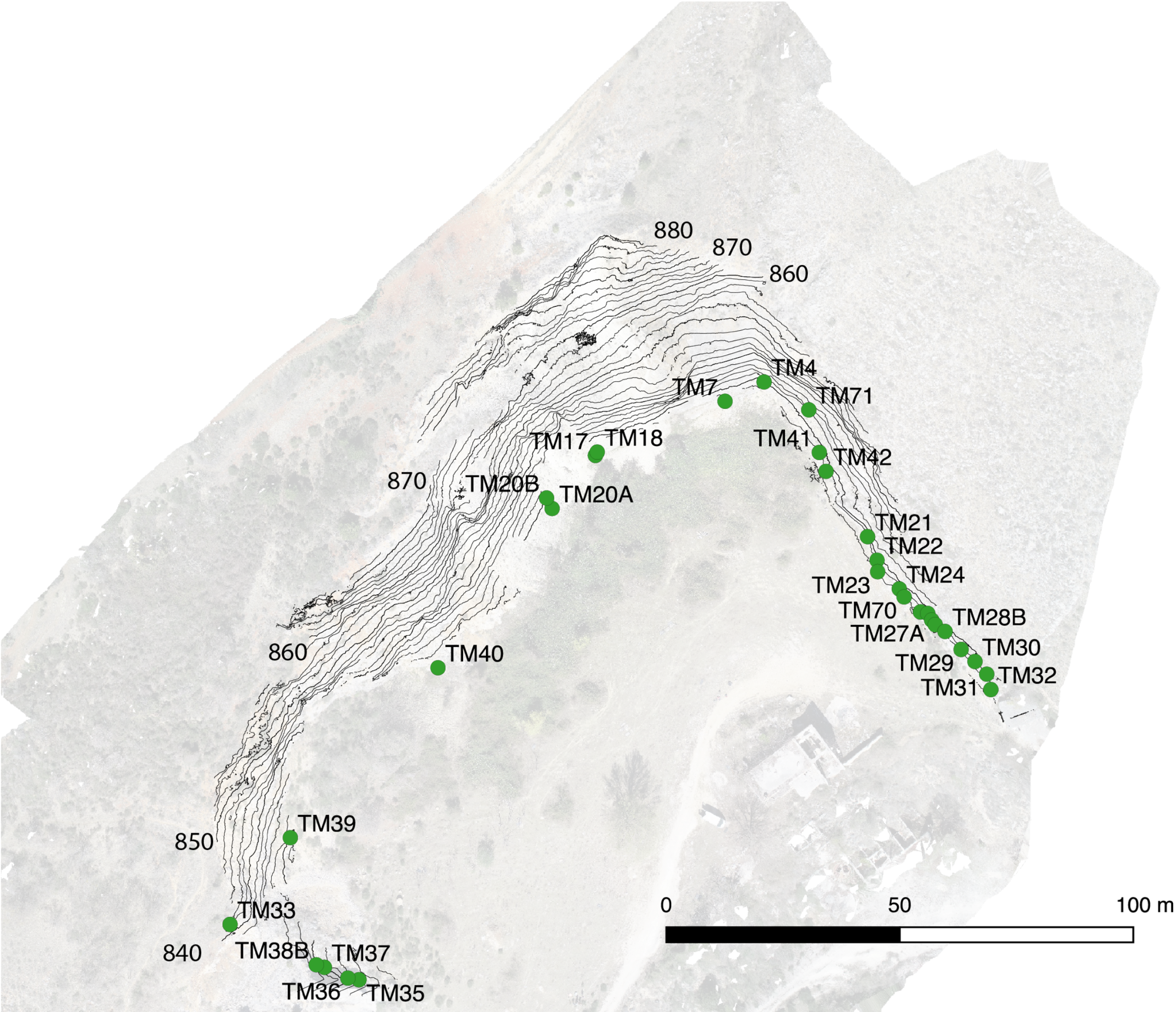

B1.3 – Locations and labels of virtual scan areas

Scan-areas locations are color-coded and labelled with different letters depending on the used orthorectified panel.

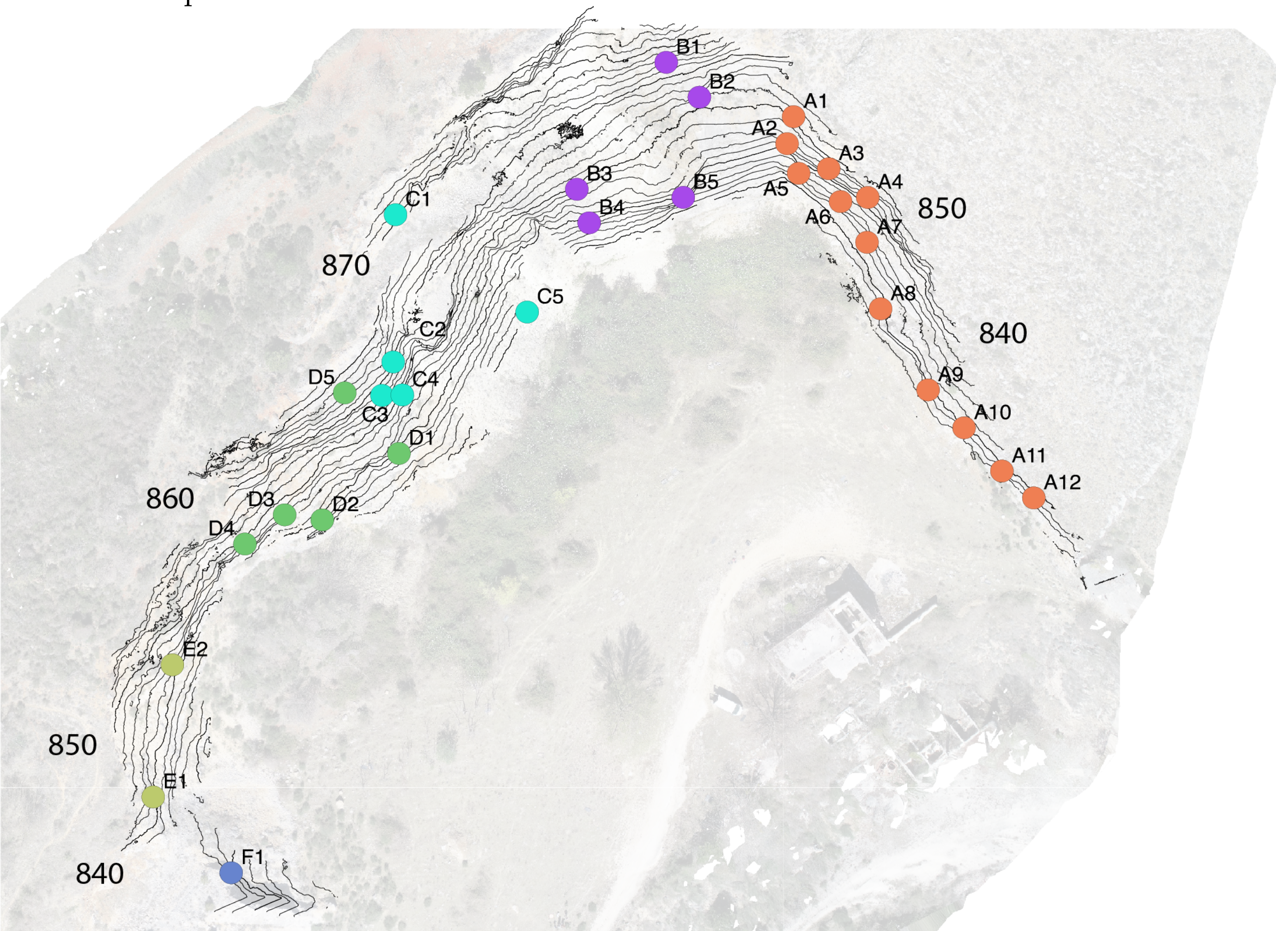

B2 – Trace length measurements

In this section we report the results of our fracture trace length analysis. The distribution of the fracture trace length values is very similar in scanlines and virtual scan-areas (B2.1). The fracture traces measured along scanlines have mostly trace lengths < 10 cm (B2.1A), whilst most of the trace lengths sampled in virtual scan areas have lengths comprised between 30 and 40 cm (B2.1B).

The mean trace length for each scanline is comprised between 10 and 25 cm and is nearly constant in the whole quarry (B2.2). The mean trace length for each virtual scan-area is comprised between 20 and 71 cm and reaches the highest values in the north-western portion of the quarry (B2.3).

B2.1 – Distribution of trace length values of fractures measured along scanlines (A) and sampled in virtual scan-areas (B)

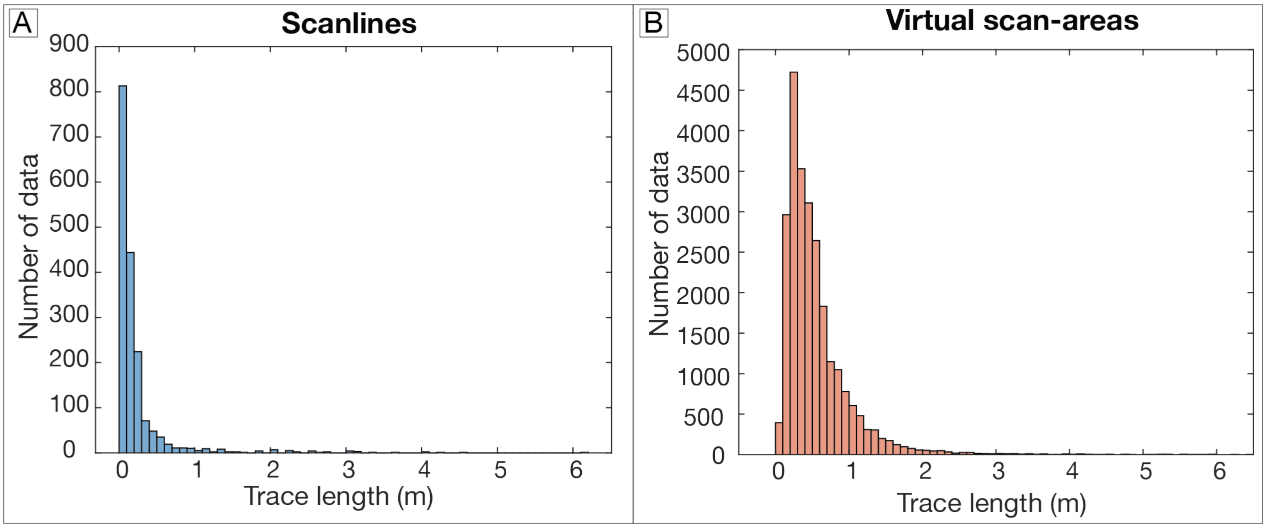

B2.2 – Distribution of the mean trace length values measured along scanlines in the quarry

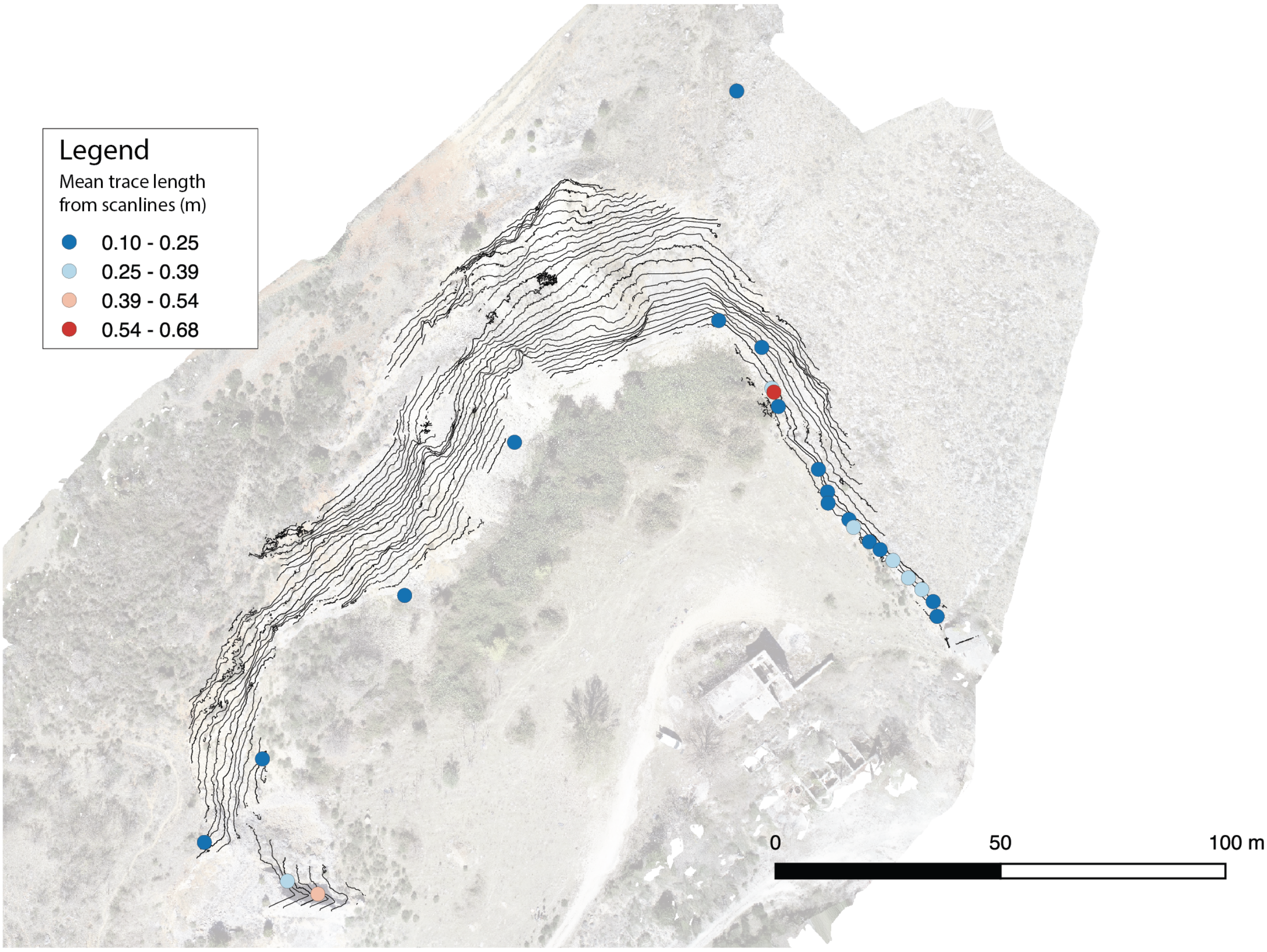

B2.3 - Distribution of the mean trace length values collected from virtual scan-areas in the quarry

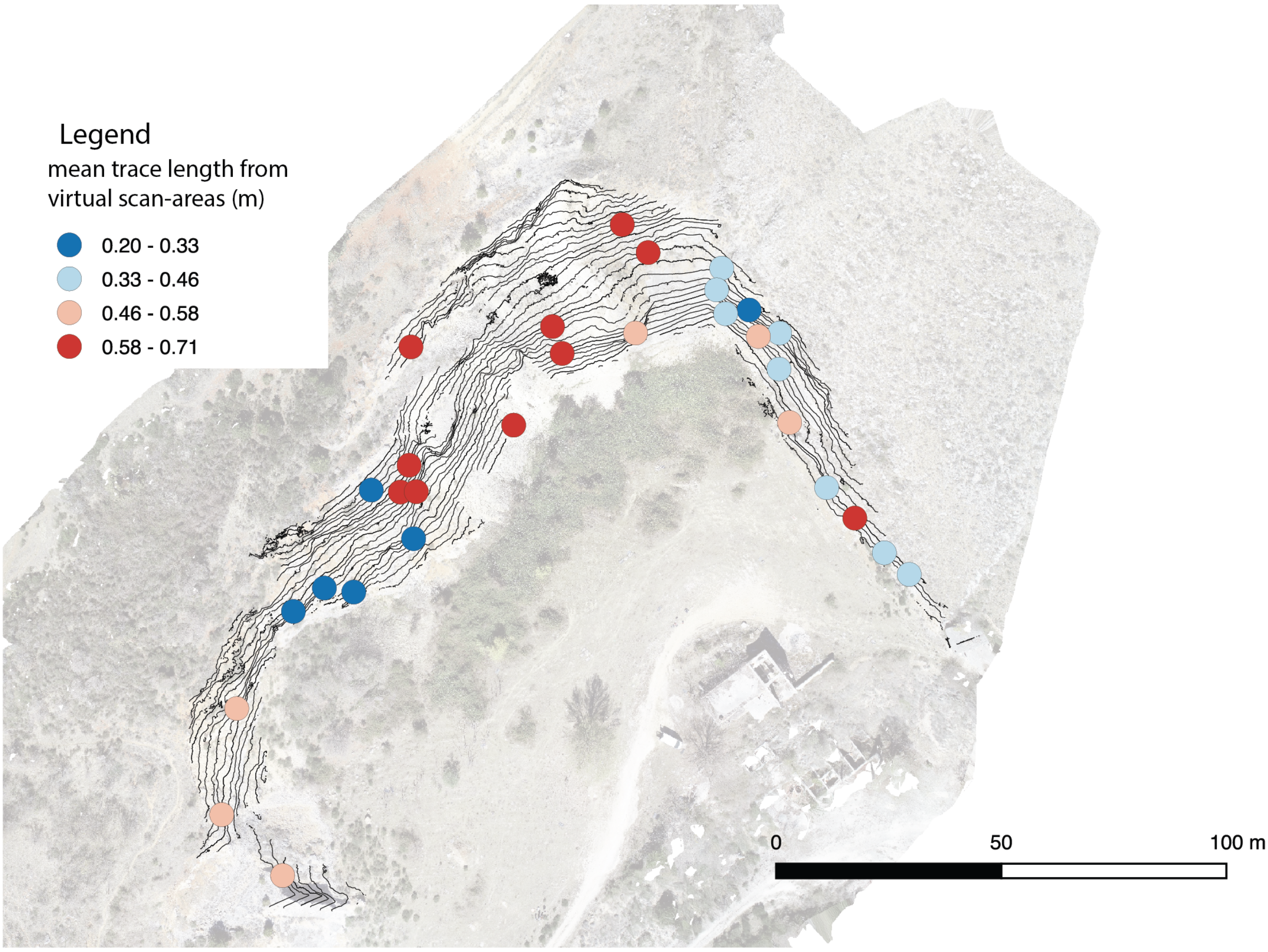

B3 – Fracture frequency and intensity

In this section we show additional plots dealing with fracture frequency and intensity resulting from fracture analysis of the samples (B3.1) and virtual scan-areas (B3.2).

B3.1. - Samples

The linear fracture frequencies measured along scanlines on the oriented samples are comprised between 41 and 344 fractures per meter and are heterogeneously distributed in the quarry (B3.1.1). The distribution of the areal fracture frequency (P20; B3.1.2) and intensity (P21; B3.1.3) values in the quarry is coherent with the linear fracture frequency (B3.1.1). We do not observe any trend of fracture frequency with the distance from the main fault (B3.1.4).

S3.1.1 – Linear fracture frequency (P10) from samples

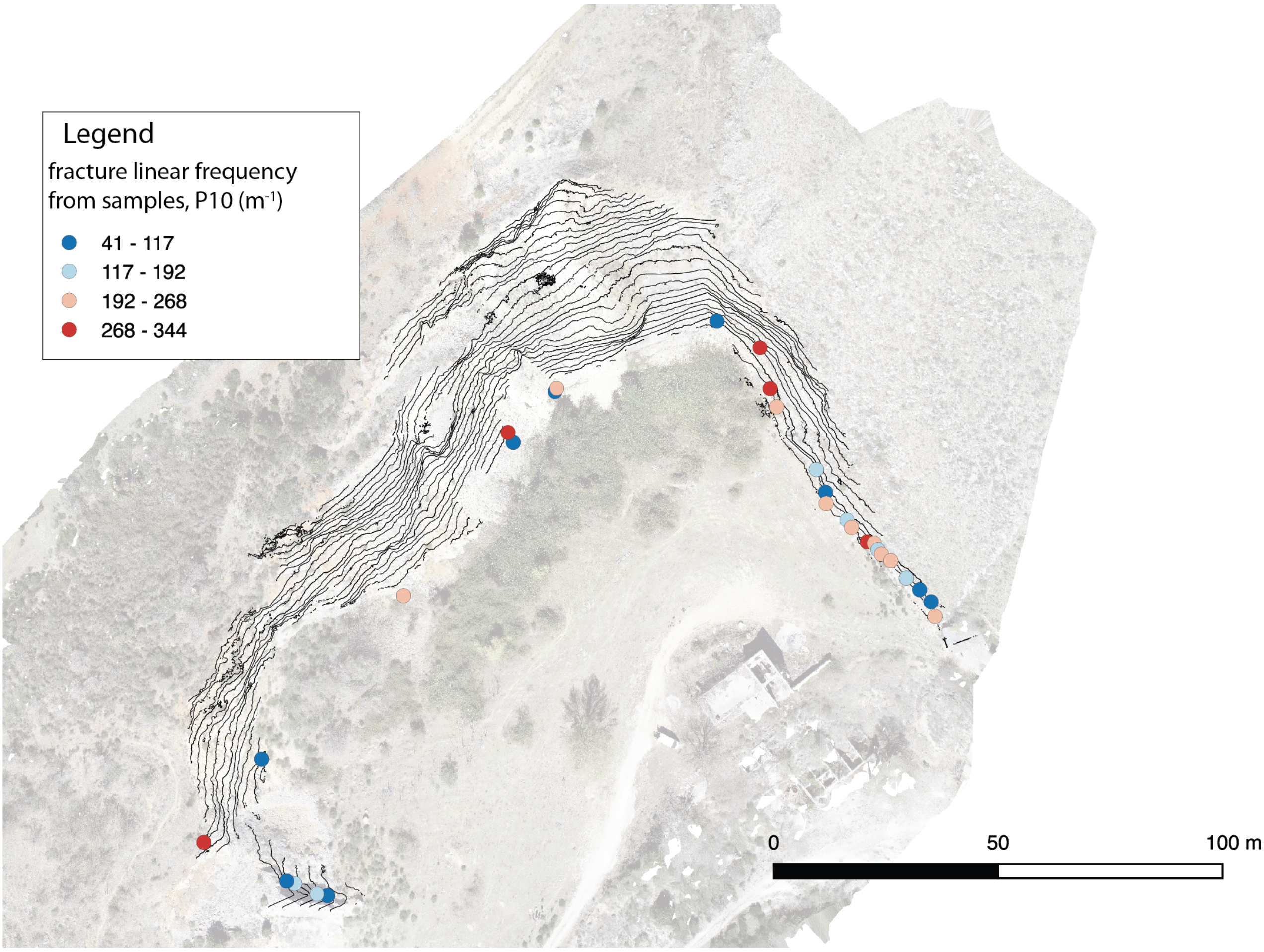

B3.1.2 – Areal fracture frequency (P20) from samples

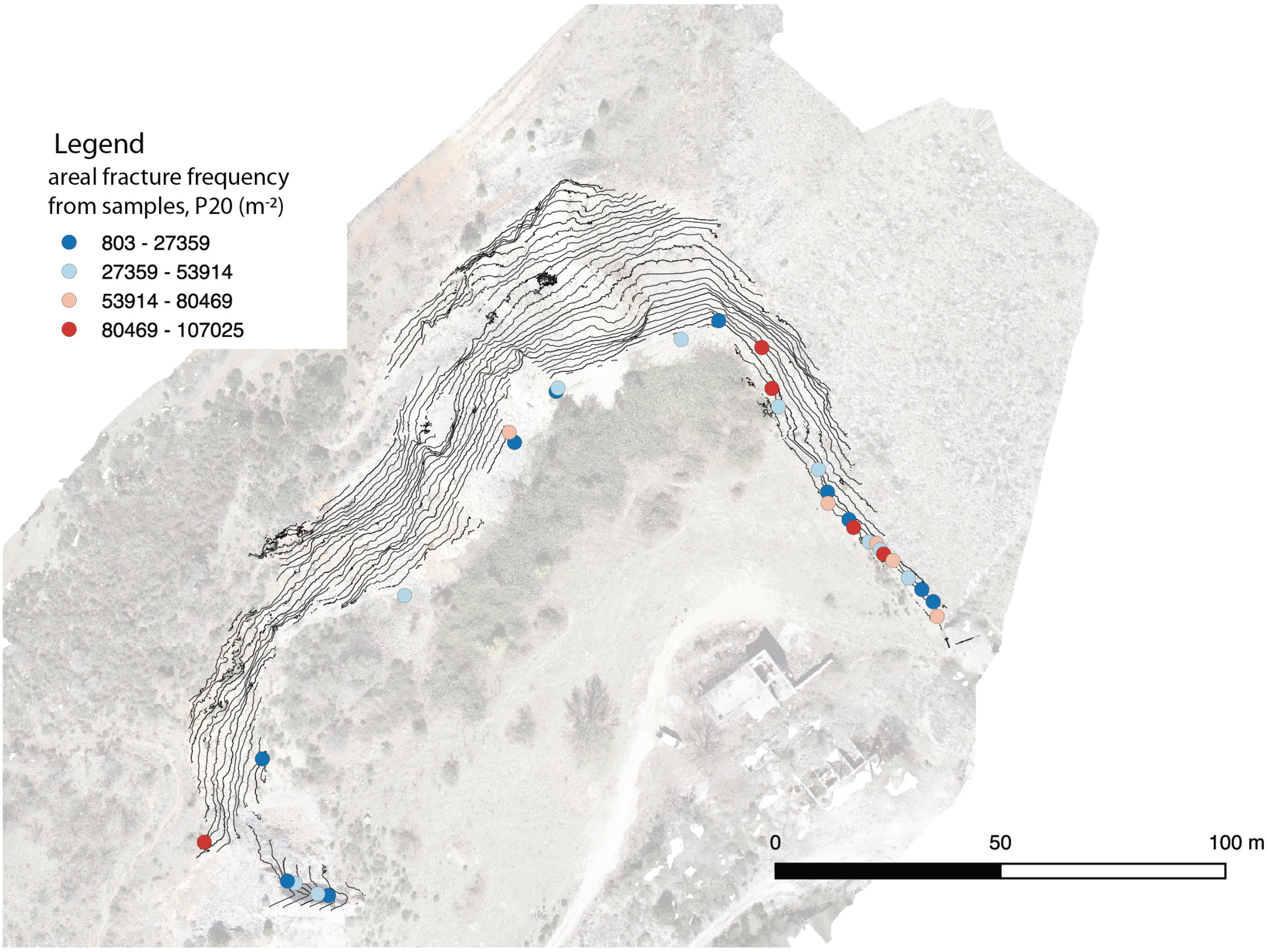

B3.1.3 – Fracture intensity (P21) from samples

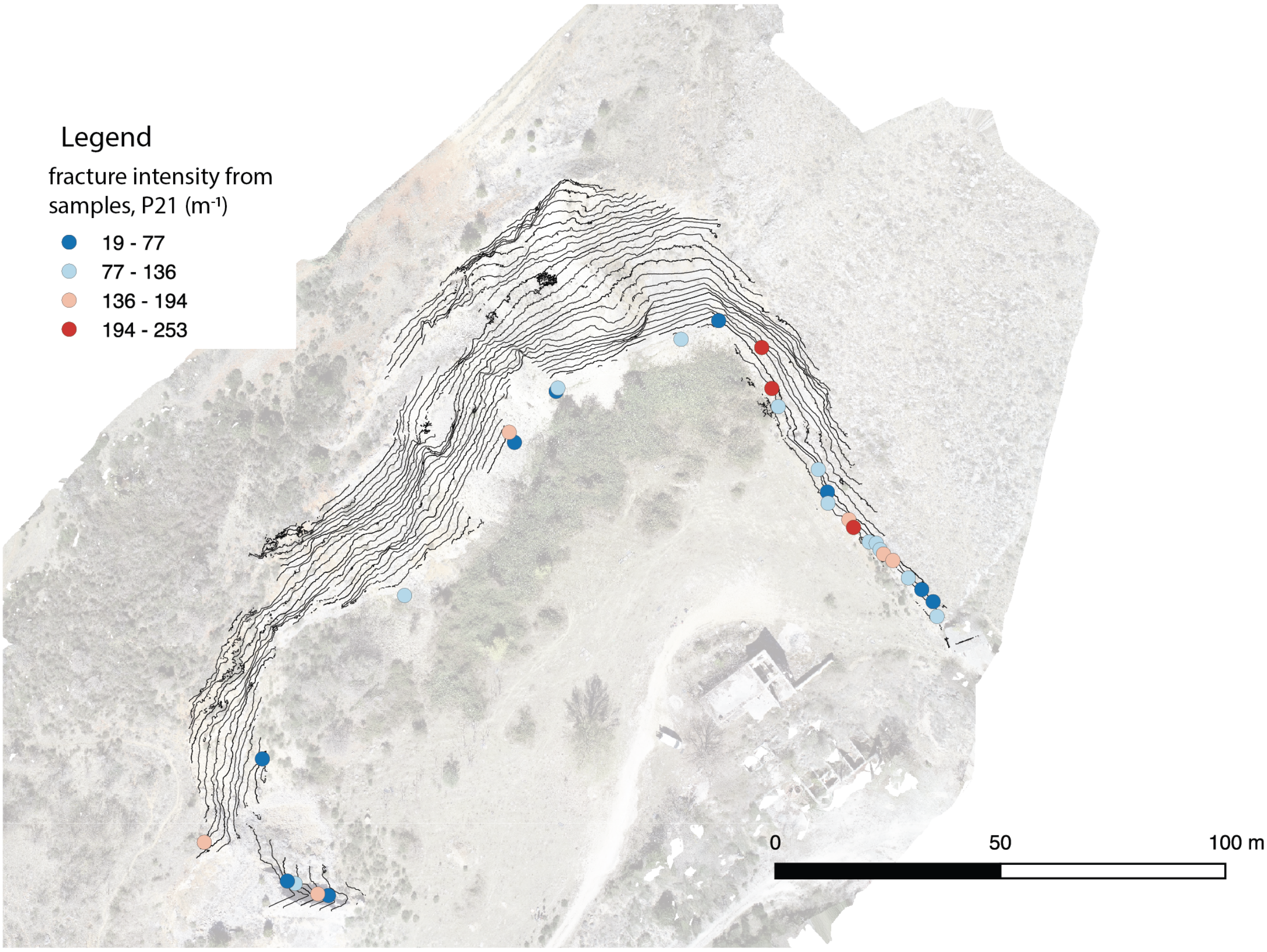

B3.1.4 – Fracture frequency (P20) from samples vs. distance from the main fault

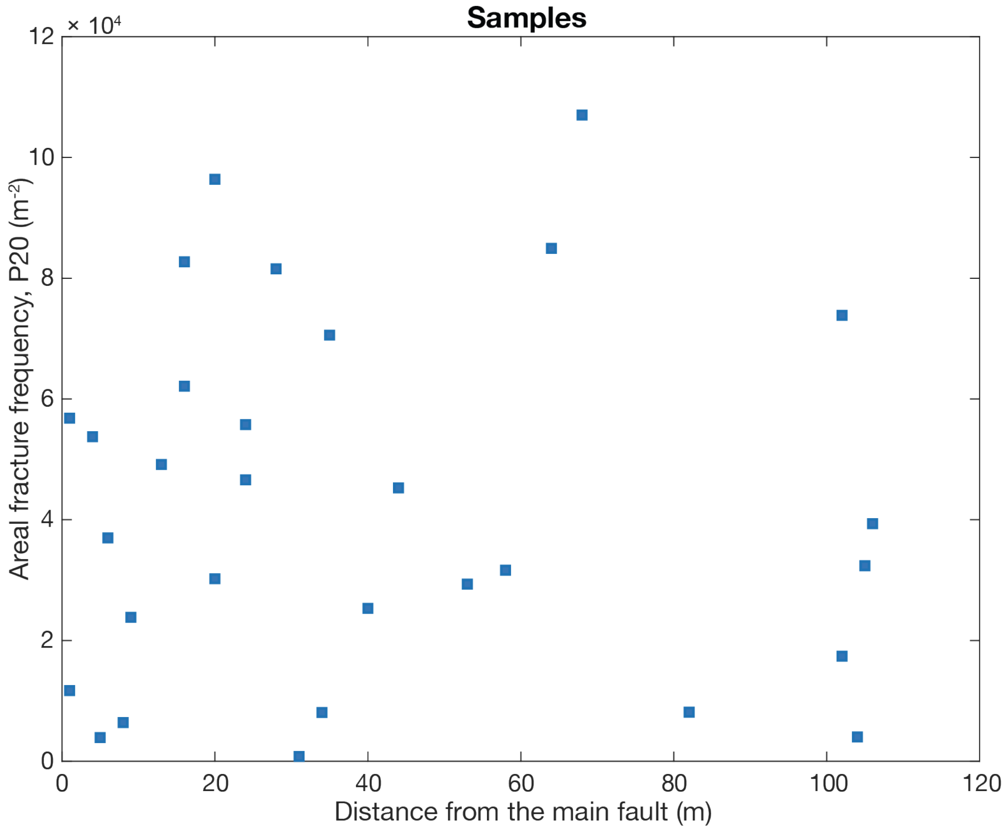

B3.2. – Fracture intensity from virtual scan-areas

The fracture intensity (P21) collected from the virtual scan-areas is comprised between 2.6 $m^{-1}$and 12.2 m^{-1}, with the highest values in the NNW and NW portion of the quarry.

B3.2.1 – Fracture intensity (P21) from virtual scan-areas

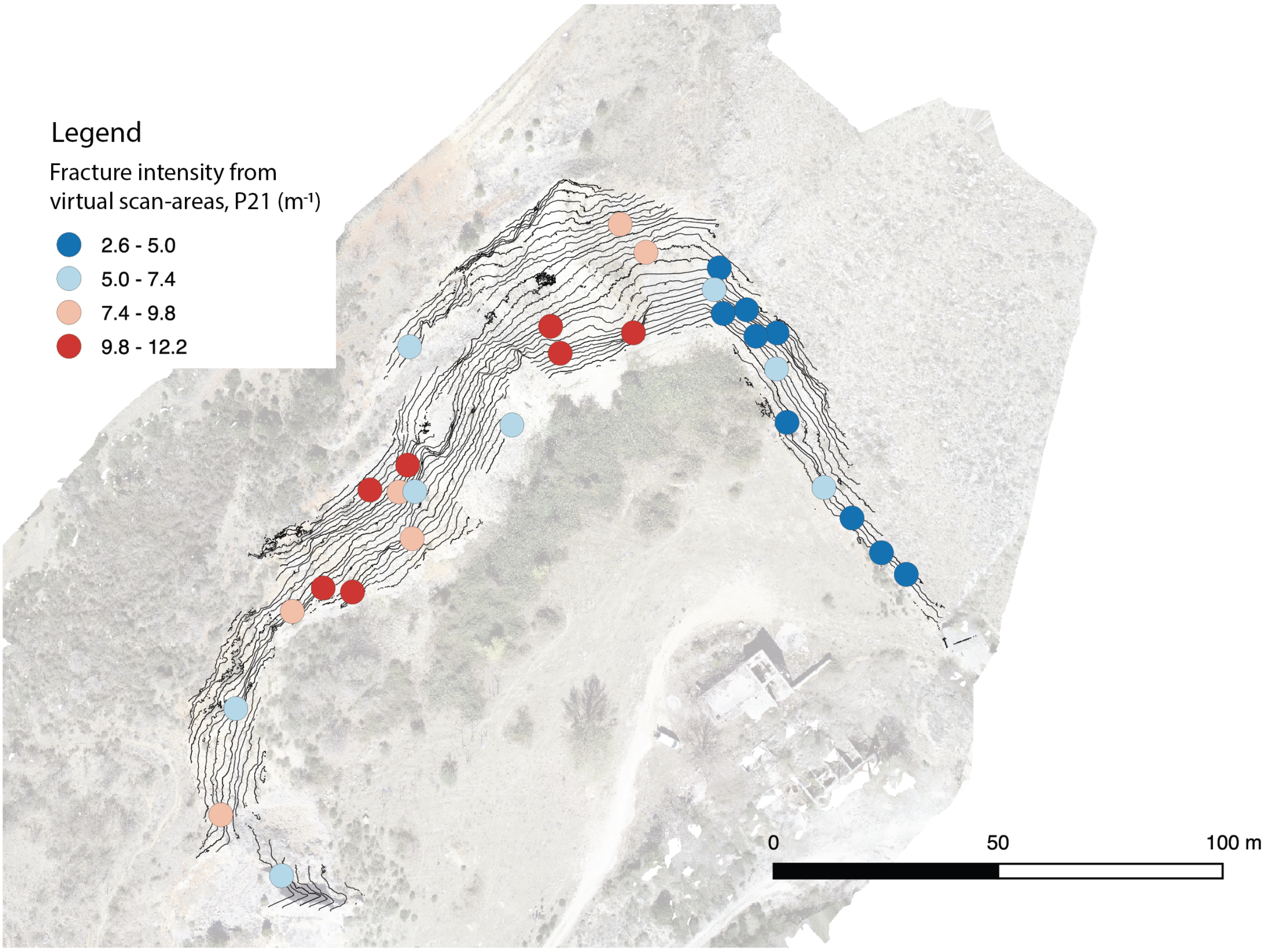

B4 – Permeability

We performed a permeability analysis on the oriented samples (B4.1) and on the virtual scan-areas (B4.2) using FracPaQ (Healy et al., 2017). FracPaQ calculates a 2D Permeability tensor (Healy et al., 2017) exploiting a 2nd-rank crack tensor (Suzuki et al., 1998). We considered the maximum permeability value (k_1) for each sample. The permeability tensor calculation depends on the areal fracture density (P21), fracture trace lengths, apertures, and orientations, and fracture connectivity (see Healy et al., 2017 for further detail). The fracture connectivity is inserted by the user by assigning a value comprised between 0 and 1 to the λ factor, which corresponds to the percentage of connected fractures (Healy et al., 2017). As a first approximation, we considered a fully connected fracture network by putting $\lambda = 1$; then we estimated the λ factor by summing the percentages of "Y" and "X" fracture nodes. The fracture aperture was assigned by FracPaQ depending on the fracture trace length using the following equation:

$A = a \times L^b$,

where A is the fracture aperture, L is the fracture trace length and a and b are constants. We assumed a linear relationship between the fracture length and the fracture aperture ($b = 1$), and $a = 6 \times 10^{-3}$. The a value chosen is the average of the values retrieved by Vermilye and Scholz (1995) for veins in limestones.

The results are discussed in section B4.3.

B4.1 – Evaluation of permeability from samples

The samples exhibit maximum permeabilities comprised between 10^{-14} and 10^{-13} that are homogeneously distributed in the quarry, although some samples show higher permeability (~10^{-12}; see section B4.1.1). The permeability values do not depend on the distance from the main fault (see section B4.1.2), and no clear dependence is observed on the carbonate facies (see section B4.1.3)

B4.1.1 – Distribution of the maximum permeability from samples (λ = 1)

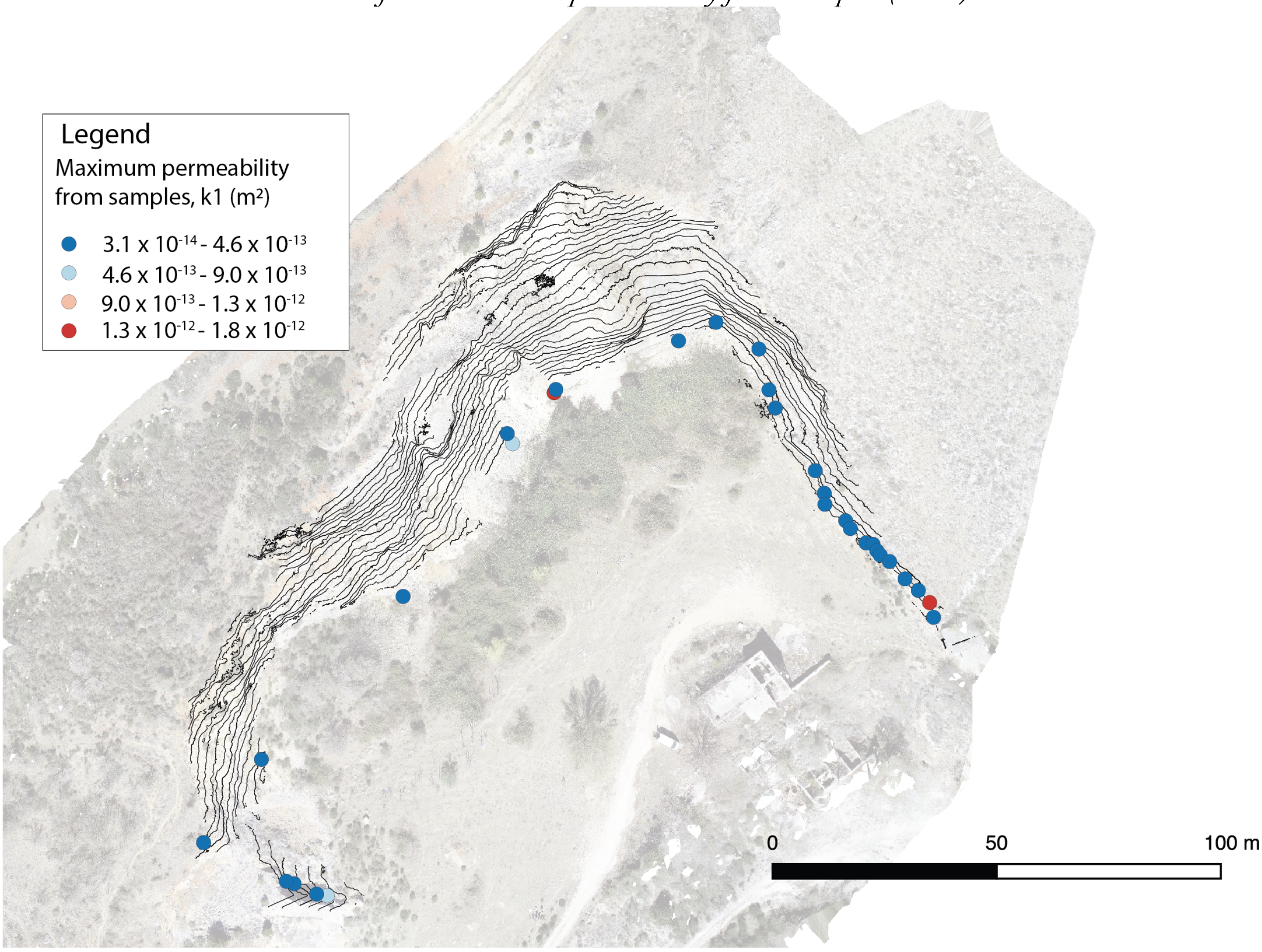

B4.1.2 - Maximum permeability and connectivity vs. distance from the main fault

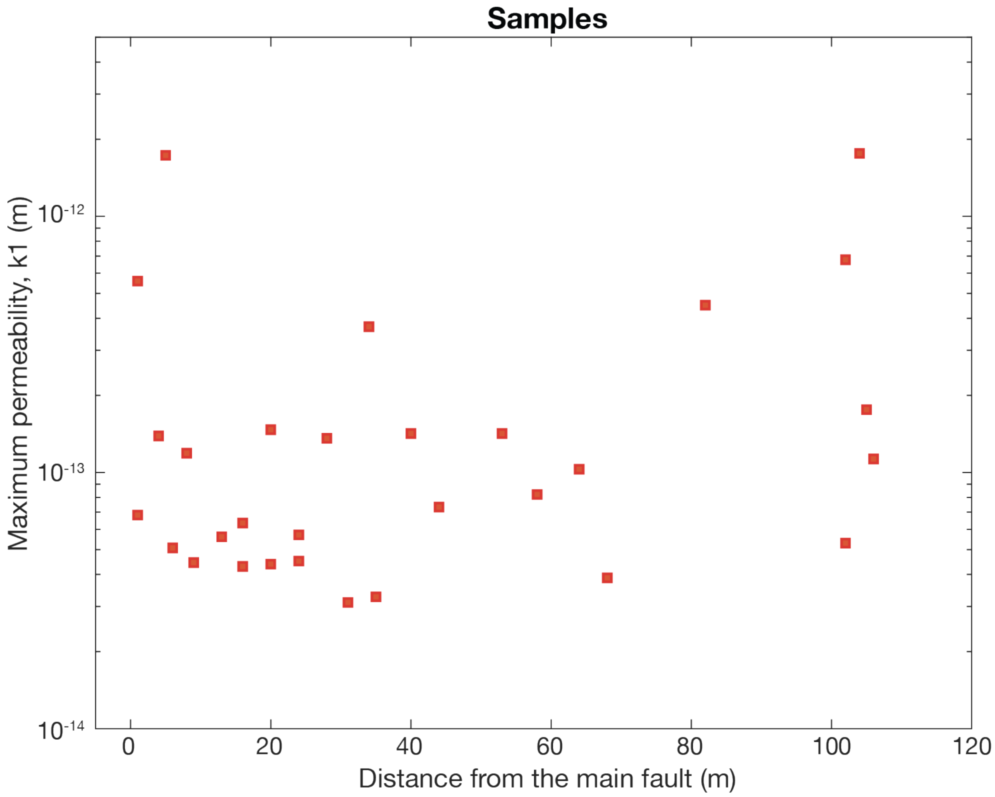

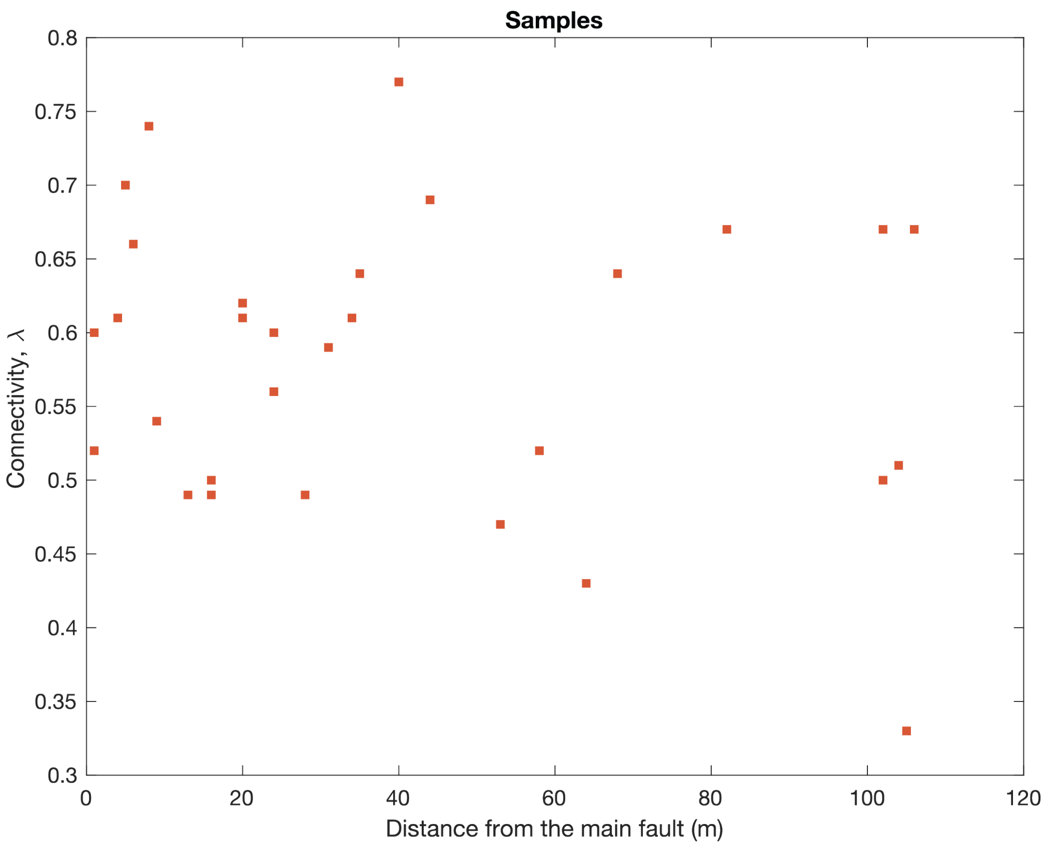

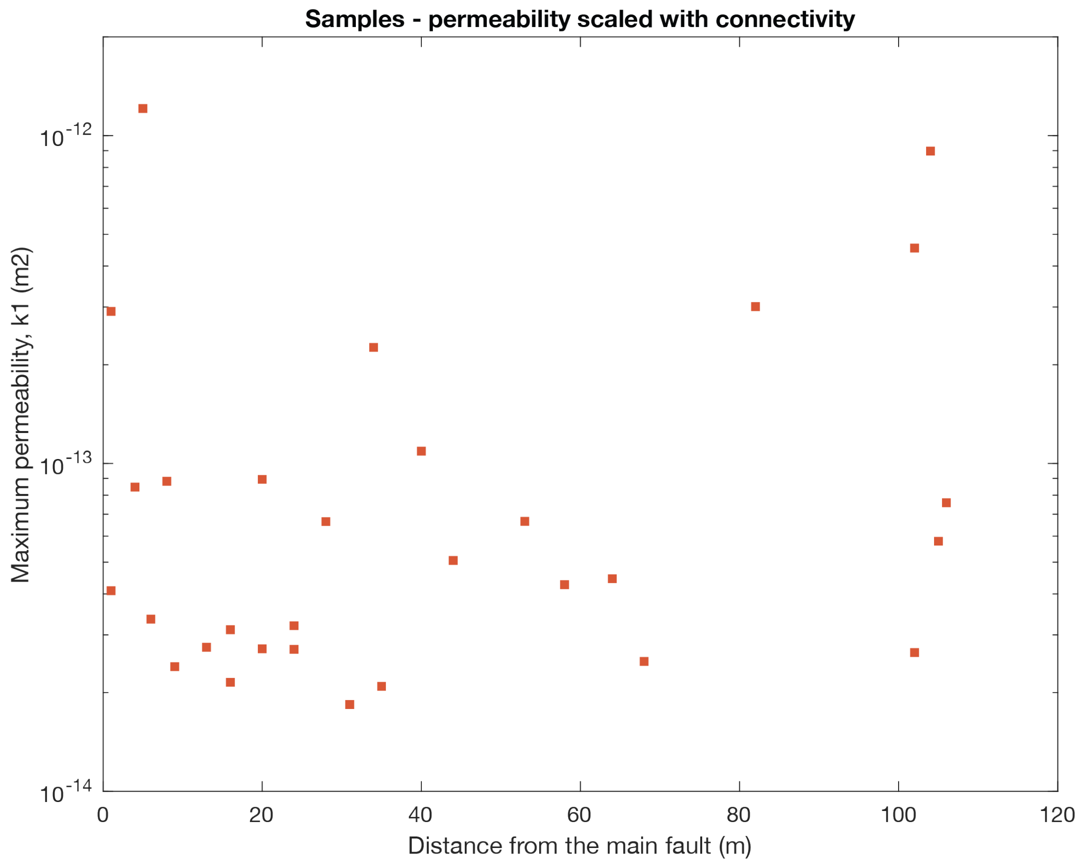

B4.1.3 – Maximum permeability vs. carbonate facies

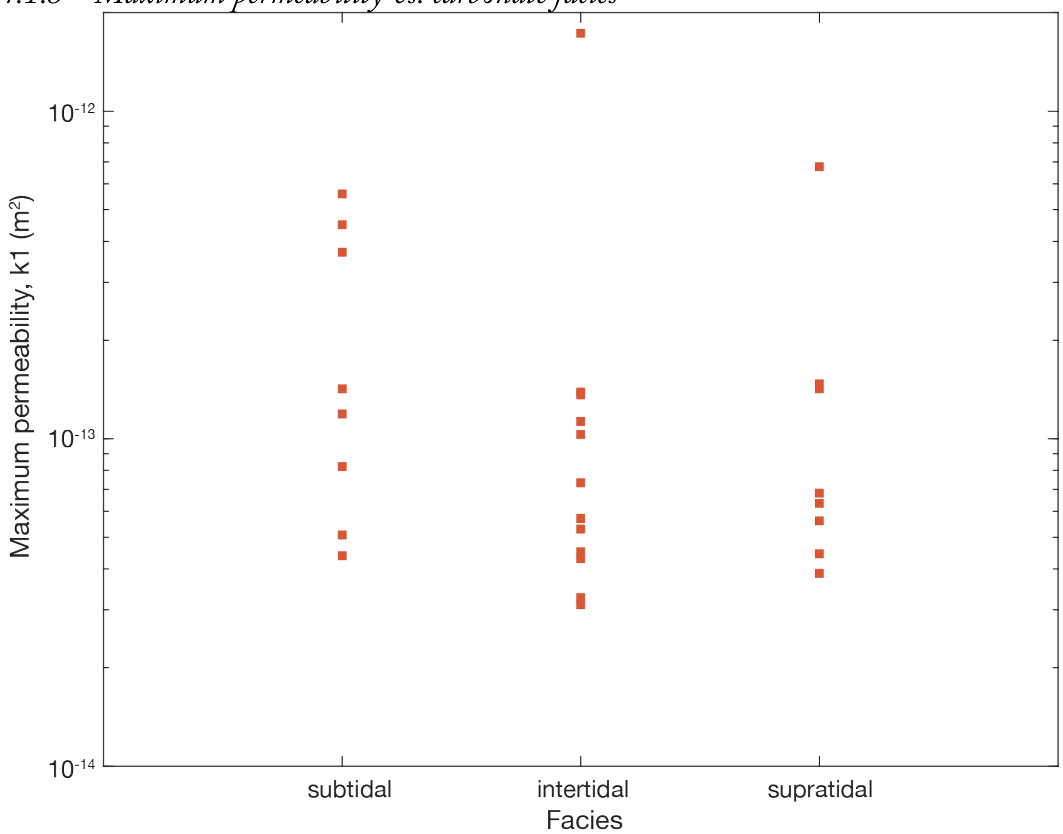

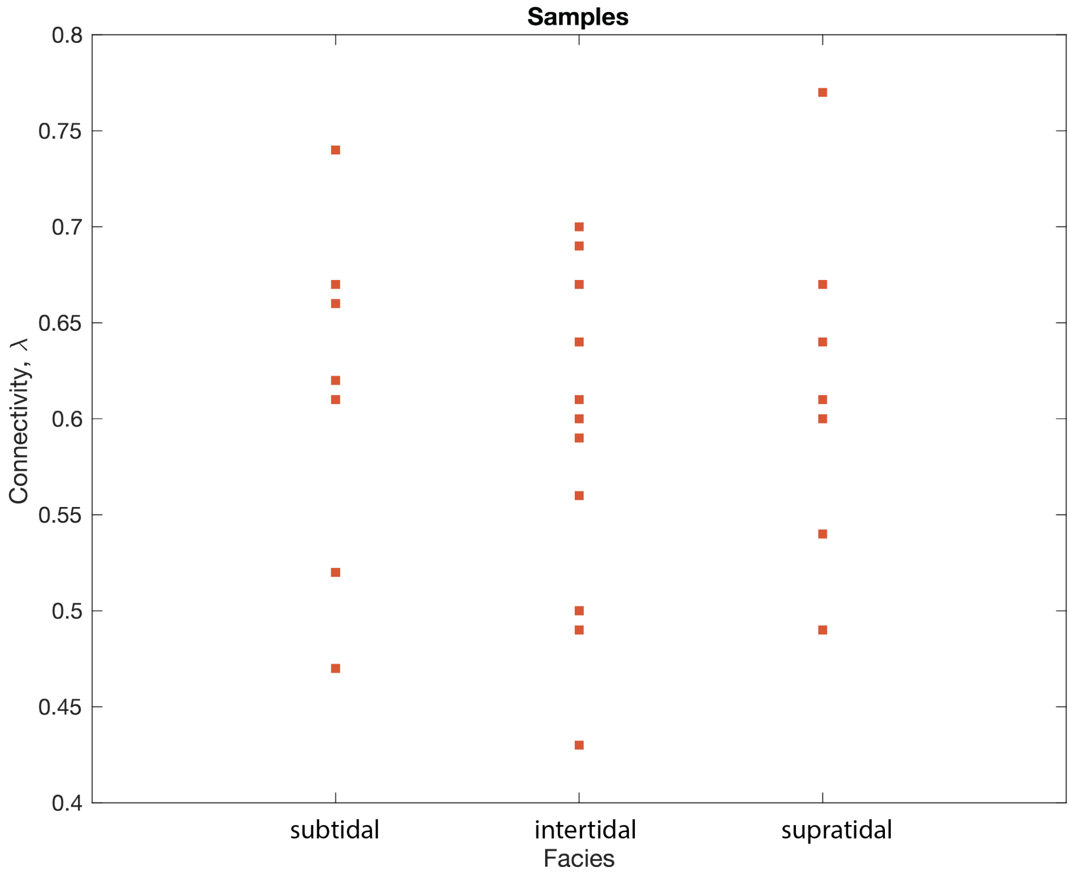
Samples
0.8
0.75
0.7
0.65
0.6
0.55
0.5
0.45
0.4
Connectivity, λ
subtidal
intertidal
supratidal
Facies

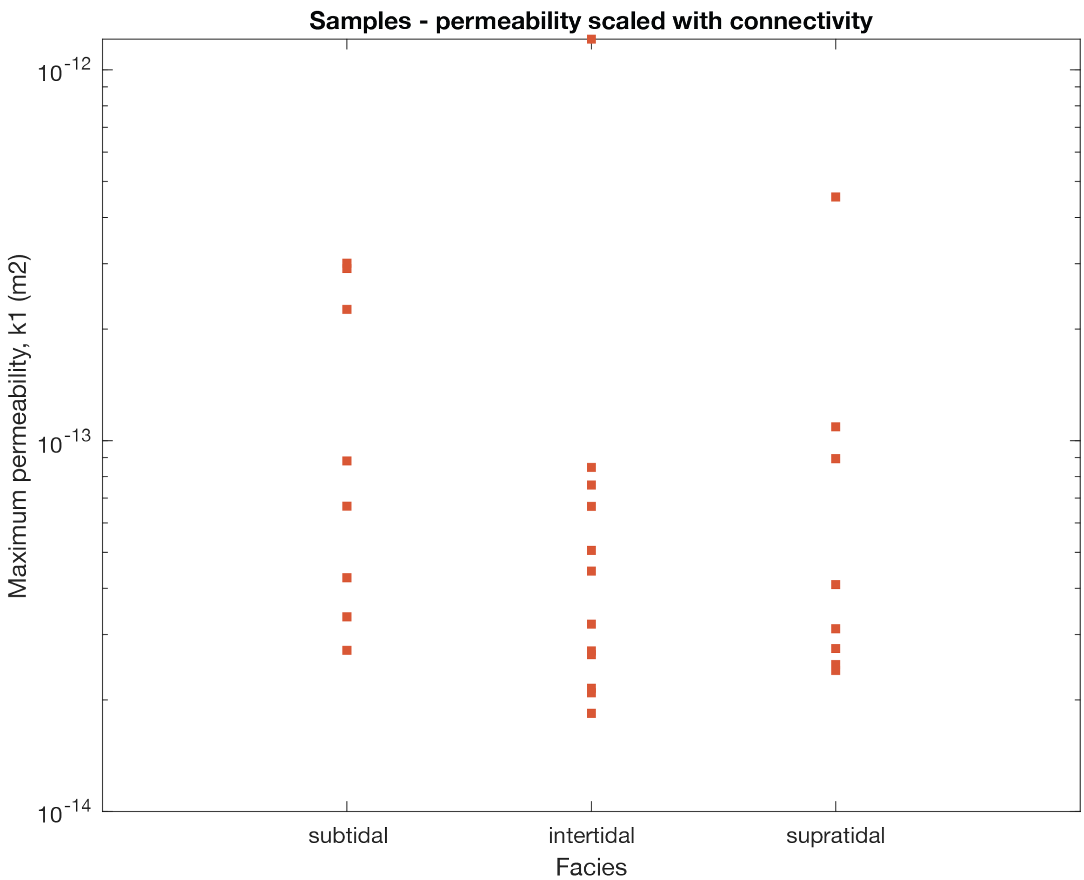
Samples - permeability scaled with connectivity
10^-12
10^-13
10^-14
Maximum permeability, k1 (m2)
subtidal
intertidal
supratidal
Facies

B4.2 – Evaluation of permeability from virtual scan-areas

The permeability is comprised between 10^{-8} and 10^{-7} considering a fully connected fracture network (λ =1), and it is slightly lower (approaching 10^{-9}) when we consider the estimated connectivity. Permeability increases moving from E to W in the quarry. The highest permeability values can be found in the western (close the main fault) and in the north-western sector of the quarry, partially reflecting the trend of fracture density (see Section 4.4). We note a slight increase in fracture density with both increasing distance from the main fault and with supratidal/intertidal facies content. Nevertheless, the permeability increases moving from ENE to WSW

B4.2.1. – Distribution of the maximum permeability from virtual scan-areas

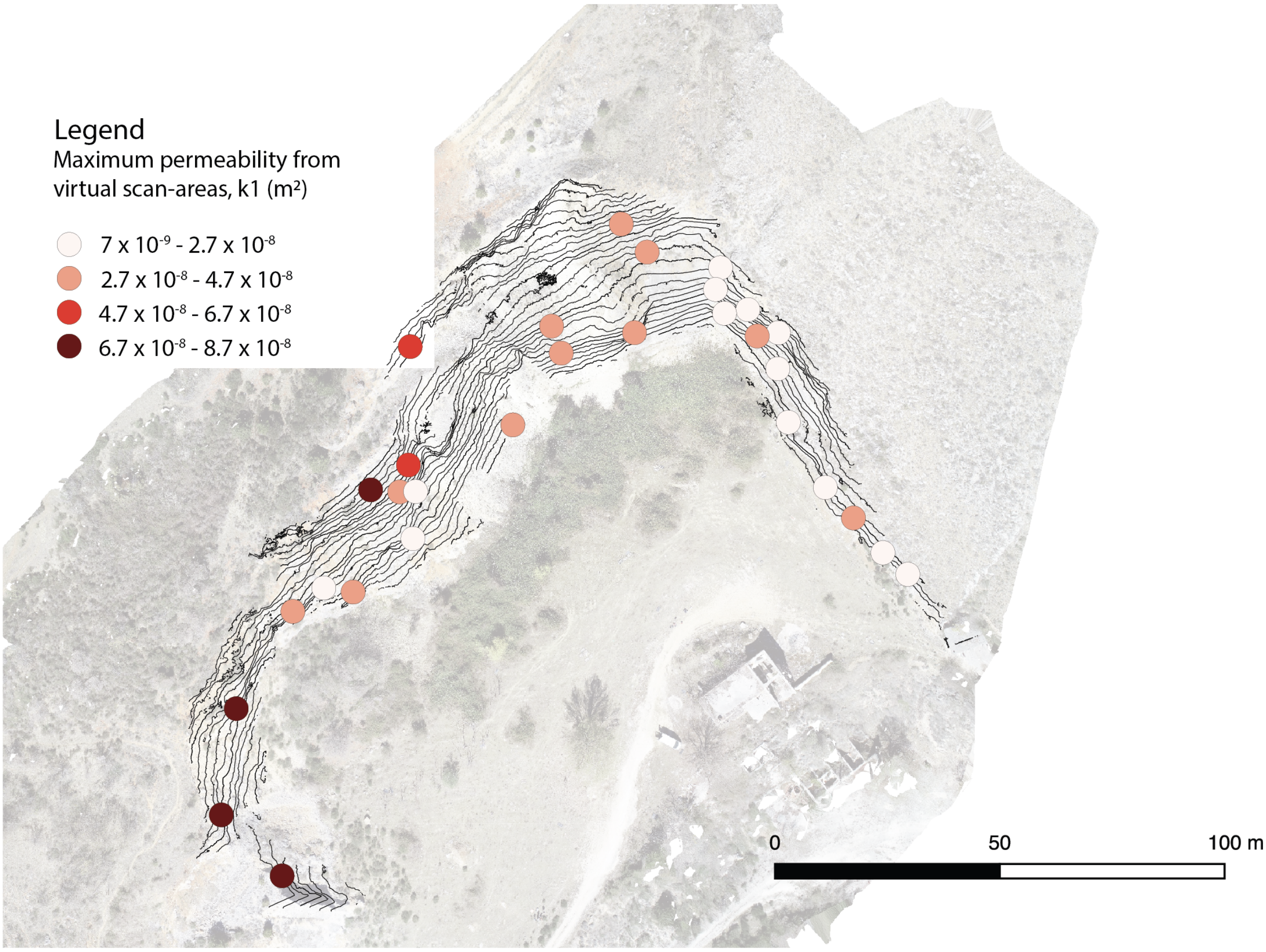

B4.2.2 - Maximum permeability and connectivity vs. distance from the main fault

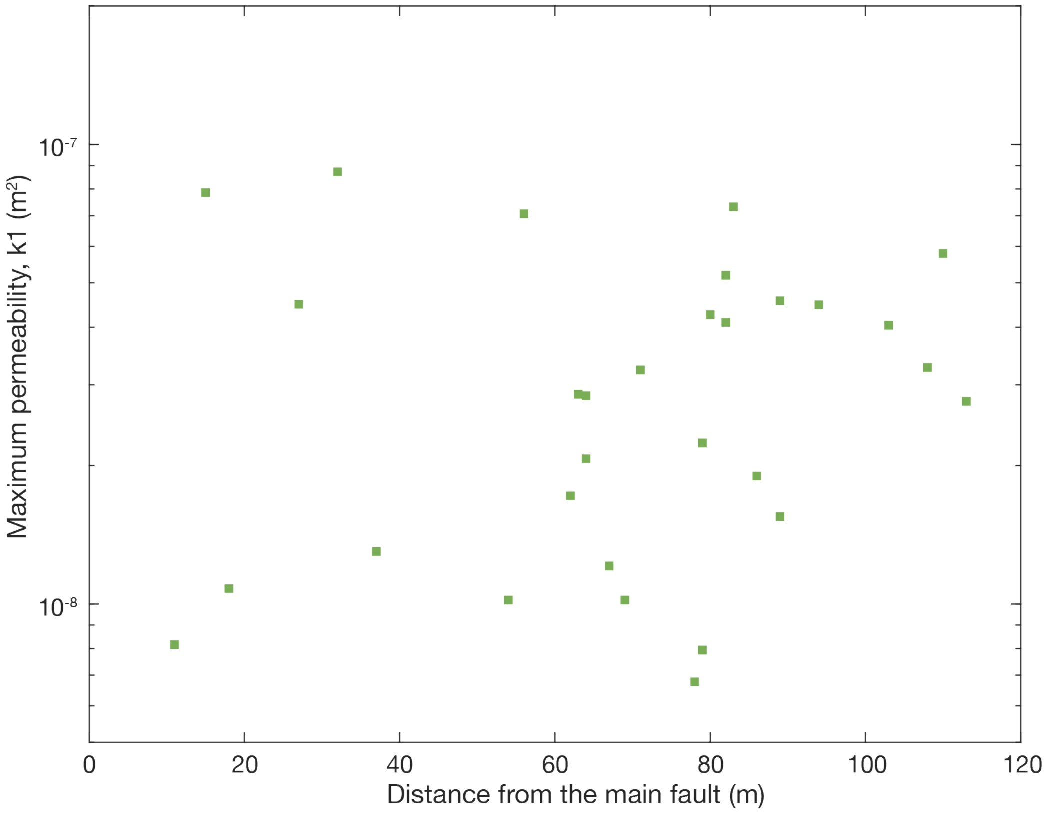

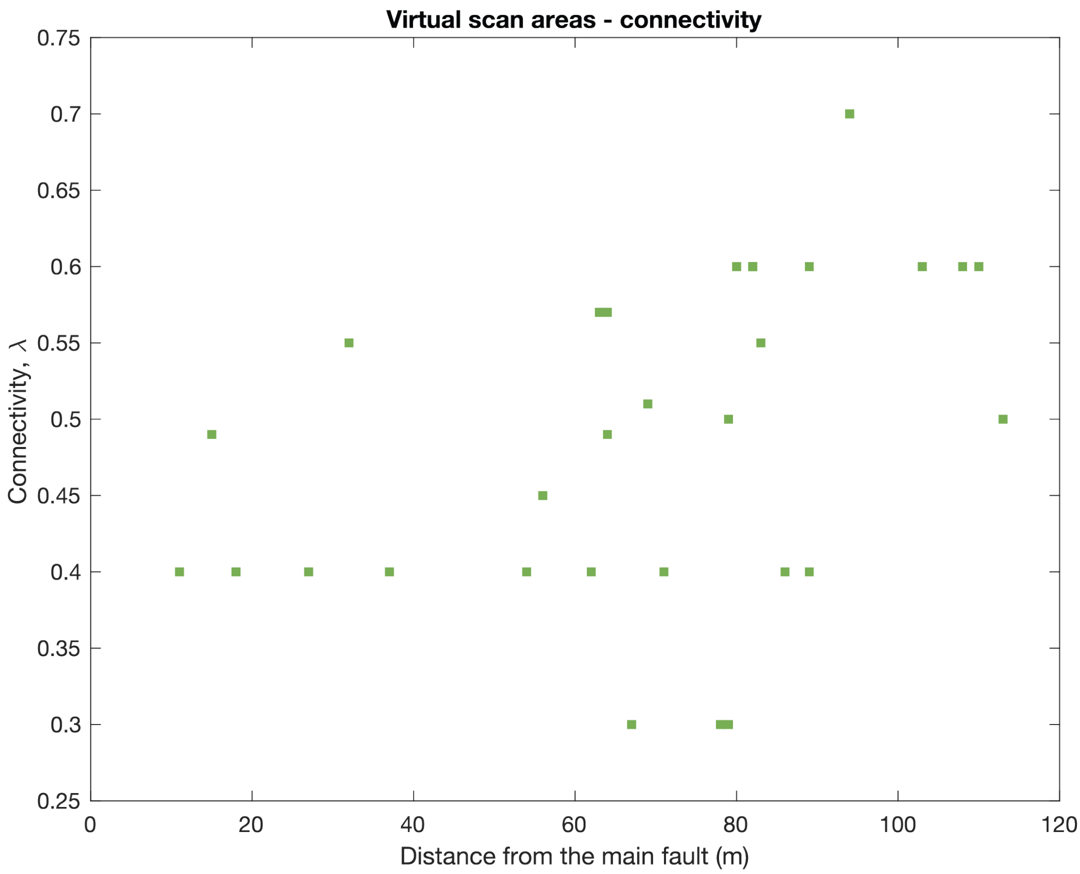

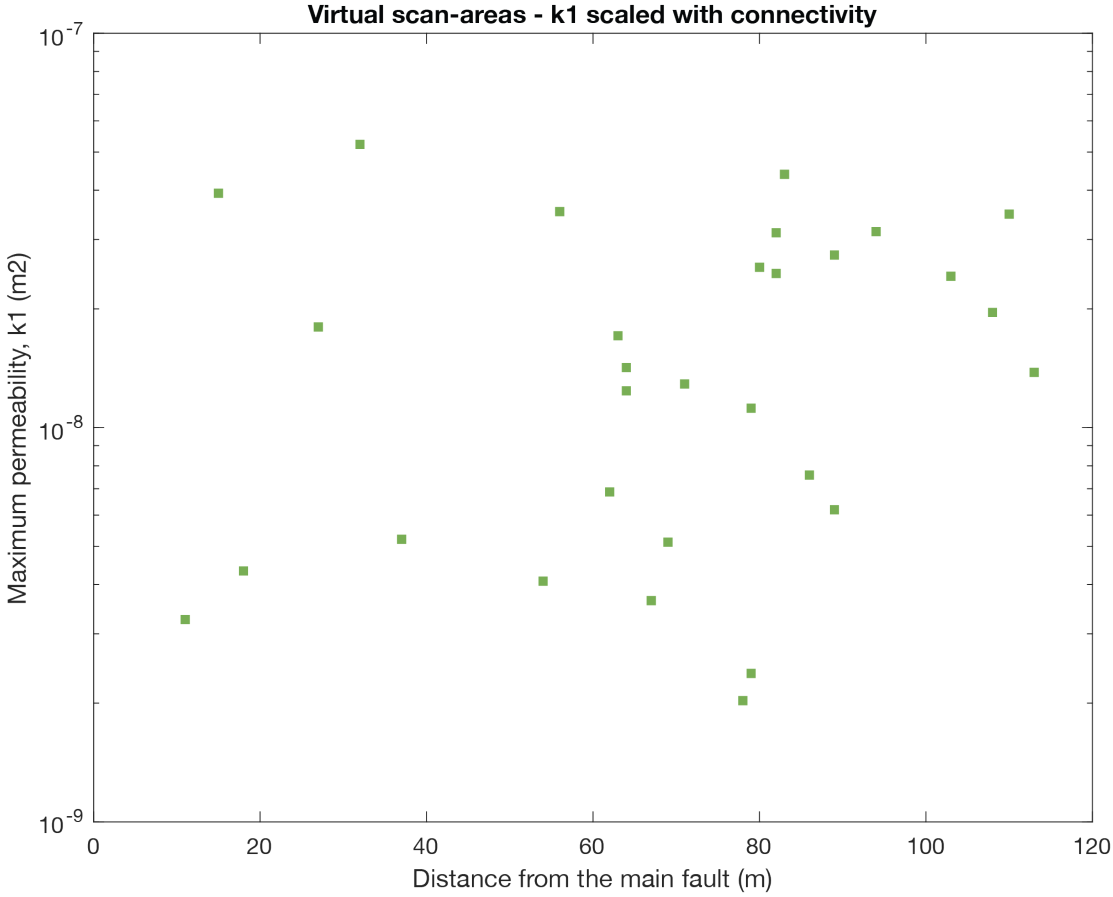

B4.2.3 – Maximum permeability vs. carbonate facies

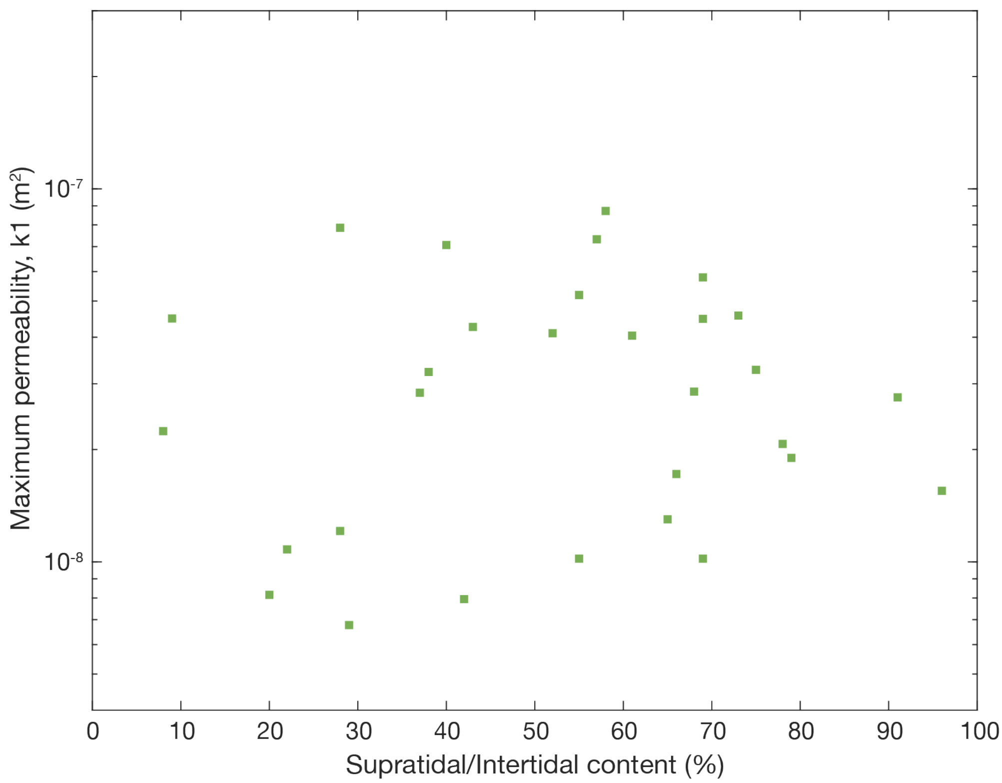

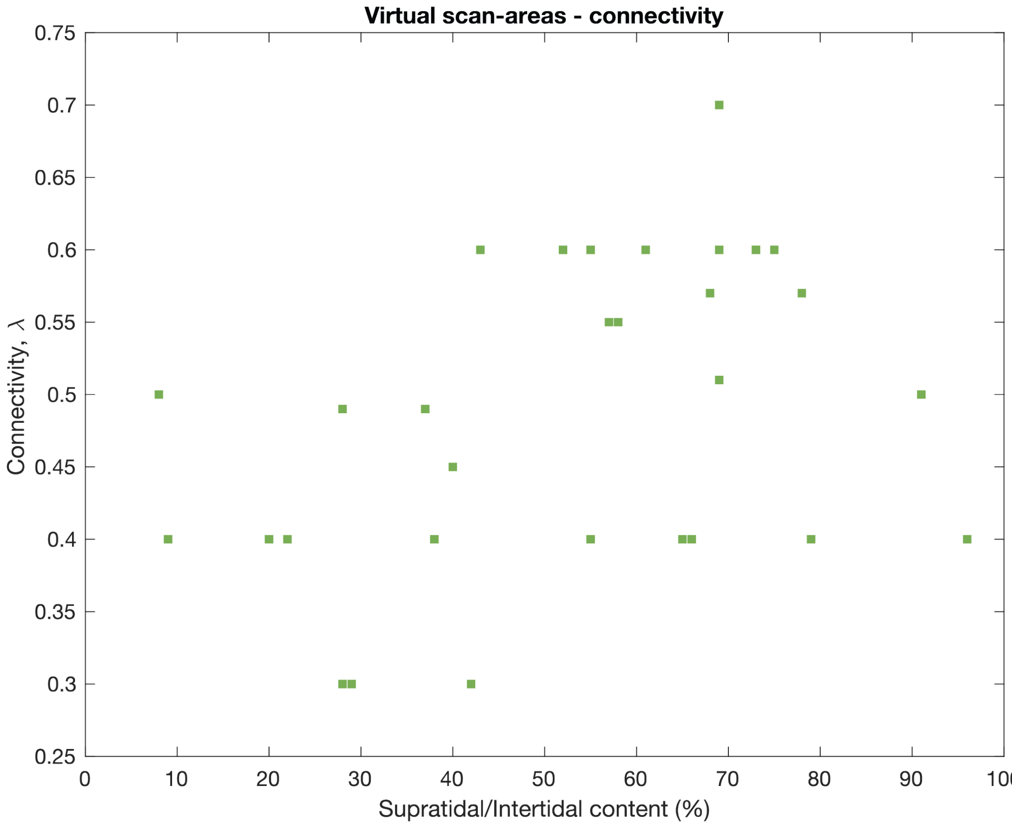
Virtual scan-areas - connectivity
Connectivity, λ
0.75
0.7
0.65
0.6
0.55
0.5
0.45
0.4
0.35
0.3
0.25
0
10
20
30
40
50
60
70
80
90
100
Supratidal/Intertidal content (%)

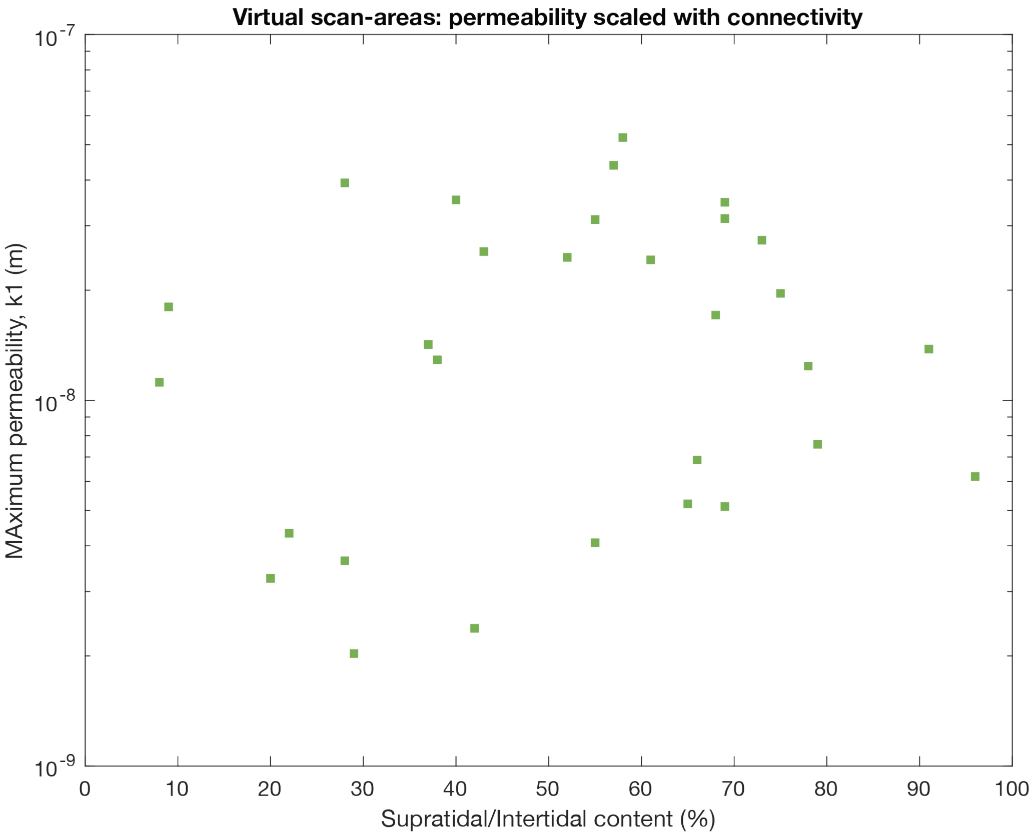
Virtual scan-areas: permeability scaled with connectivity
MAximum permeability, k1 (m)
10^-7
10^-8
10^-9
0
10
20
30
40
50
60
70
80
90
100
Supratidal/Intertidal content (%)

B4.3 Preliminary results on permeability estimation

We obtained maximum 2D permeabilities ranging between 10^{-14} m^2 and 10^{-12} m^2 for the oriented samples, and between 10^{-7} and 10^{-9} for virtual scan-areas. Although the values retrieved from rock samples are in agreement with modelled (e.g., Bisdom et al., 2016), lab (e.g., Bernabè et al., 2003), and in situ (Worthington and Ford, 1995; Cappa et al., 2005; Noushabadi et al., 2011; Medici et al., 2019a, 2019b) measurements on fractured carbonates, suggesting permeabilities comprised between 10^{-10} and 10^{-15}, the values obtained from the virtual scan-areas are very high. The different values obtained applying the two methods are not surprising: previous in-situ measurements on fractured carbonates evidenced permeability can be very variable and depends on the scale of observations (e.g., Worthington and Ford, 1995). In fact, the number of open fractures (and hence permeability) increases with the considered rock volume. In our analysis, although the fracture analysis conducted on rock samples leads to higher fracture densities than in virtual scan-areas (B3.1 vs. Fig. 4.6), the difference of permeability can be attributed to the different fracture lengths sampled in the two methods, leading to very different modelled fracture apertures. The high permeability values observed for virtual scan areas derive from the modelled fracture aperture, which we scaled with fracture length assuming a linear relationship and a scale factor a = 6×10^{-3} (see section B5). Such value of a was chosen as the mean of the values retrieved by Vermilye and Scholz (1995) for calcite veins within limestones and could not hold for open and long fractures.

Dealing with the relative trend of fracture permeability in the quarry, the fracture density distribution obviously affects the permeability within the damage zone, as suggested by the slight increase of the scan-area-derived permeability both with distance from the main fault (B4.2.2) and with supratidal/intertidal facies content (B4.2.3). Similarly, the oriented samples, according with fracture density (B3.1), do not show any permeability trend with distance from the main fault. The trends evidenced by the virtual-scan areas (B4.2.2, B4.2.3) are less evident than those observed for fracture density (Fig. 4.8), because they are masked by the opposite distribution of permeability close to the main fault between the western and the eastern sectors of the quarry (B.4.2.1). The highest permeability values in the western sector are caused by relatively longer fracture traces in the western sector (B2.3), leading to higher modelled aperture and hence permeabilities.

Therefore, although FracPaQ seems to model correctly the relative variations of permeability, the assessment of absolute values from virtual scan-areas (and scan-areas in general) demands further work. In particular, defining more accurately the relationship between fracture length and fracture aperture could improve the permeability estimation.

B5 – Tables

B5.1 - Results for scanline surveys. SUB: subtidal; SUP: supra- and inter-tidal.

Name	Effective length (m)	Trend	Plunge	Distance from the main fault (m)	Fracture spacing (cm)	Fracture frequency, P10 (m^{-1})	Mean trace length (m)	Main facies
SL1	2.09	320	0	44	5.1	20	0.18	SUB
SL2	1.91	323	3	40	3.7	27	0.18	SUP
SL3	2.01	150	9	35	4.0	25	0.11	SUB
SL4	1.70	316	14	31	8.1	12	0.10	SUB
SL5	1.64	318	14	28	6.1	16	0.29	SUB
SL6	2.23	155	21	24	4.7	21	0.23	SUB
SL7	1.50	164	18	20	3.8	27	0.15	SUP
SL8	1.40	141	18	16	8.0	13	0.28	n.d.
SL9	2.87	302	14	13	3.8	26	0.25	SUP
SL10	1.71	339	2	8	5.2	19	0.38	SUB
SL11	1.70	157	6	5	3.6	28	0.22	SUP
SL12	0.47	345	16	1	2.1	47	0.15	n.d.
SL13	6.38	130	3	4	10.1	10	0.42	SUB
SL14	7.96	142	13	9	6.4	16	0.32	SUP
SL15	3.83	357	4	146	6.6	15	0.17	n.d.
SL16	2.82	204	27	16	3.9	25	0.21	n.d.
SL17	4.14	184	29	34	3.9	25	0.16	SUB
SL18	5.29	229	1	58	4.8	21	0.20	SUP
SL19	5.66	326	5	64	6.4	16	0.32	SUB
SL19b	3.19	147	4	61	8.6	12	0.68	n.d.
SL20	3.79	334	7	53	3.1	32	0.17	SUP
SL21	4.04	312	6	68	2.6	39	0.21	SUP
SL22	3.62	127	3	82	2.4	42	0.15	SUB

SL23	1.34	46	1	104	3.3	31	n.d.	SUP
SL24	2.24	69	2	105	3.1	32	n.d.	SUP
SL25	3.35	201	6	102	2.2	46	0.21	SUP

B5.2 – Results of the fracture analysis performed on the oriented samples. SUB: subtidal carbonate facies; INT: intertidal carbonate facies; SUP: supratidal carbonate facies.

Sample	Mean spacing (mm)	Fracture frequency, P10 (m^{-1})	Fracture intensity, P21 (m^{-1})	Fracture frequency, P20 (m^{-2})	Maximum permeability, k1 (m^2)	Facies	Connectivity, λ	Revised maximum permeability, k1 (m^2)
TM21	7	156	106.3	45268	7.33E-14	INT	0.69	5.06E-14
TM22	9	107	72.9	25315	1.42E-13	SUP	0.77	1.09E-13
TM23	5	214	122.6	70576	3.27E-14	INT	0.64	2.09E-14
TM24	6	192	148.8	803	3.11E-14	INT	0.59	1.83E-14
TM26A	3	299	113.1	46612	5.71E-14	INT	0.56	3.20E-14
TM26B	4	244	122.1	55769	4.51E-14	INT	0.6	2.70E-14
TM27A	9	130	99.7	30228	1.47E-13	SUP	0.61	8.94E-14
TM27B	4	267	175.2	96384	4.39E-14	SUB	0.62	2.72E-14
TM28B	4	264	137.9	62123	6.35E-14	SUP	0.49	3.11E-14
TM29	7	137	117.3	49136	5.61E-14	SUP	0.49	2.75E-14
TM30	26	41	23.1	6409	1.19E-13	SUB	0.74	8.82E-14
TM31	23	44	29.1	3931	1.73E-12	INT	0.7	1.21E-12
TM32	5	206	125.0	56822	6.82E-14	SUP	0.6	4.09E-14
TM33	4	280	183.6	82715	4.30E-14	INT	0.5	2.15E-14
TM35	11	100	62.4	11708	5.59E-13	SUB	0.52	2.91E-13
TM36	7	162	166.1	53752	1.39E-13	INT	0.61	8.47E-14
TM37	7	181	90.7	37000	5.08E-14	SUB	0.66	3.35E-14
TM38B	10	110	69.3	23821	4.45E-14	SUP	0.54	2.40E-14
TM39	11	97	30.9	8069	3.71E-13	SUB	0.61	2.26E-13
TM40	5	201	86.1	31650	8.21E-14	SUB	0.52	4.27E-14
TM41	3	344	203.9	84940	1.03E-13	INT	0.43	4.45E-14

TM42	5	203	84.5	29333	1.42E-13	SUB	0.47	6.66E-14
TM4	16	64	31.1	8124	4.50E-13	SUB	0.67	3.01E-13
TM20A	14	81	56.3	17401	6.77E-13	SUP	0.67	4.53E-13
TM20B	4	286	163.9	73844	5.30E-14	INT	0.5	2.65E-14
TM17	22	46	18.9	4030	1.76E-12	n.d.	0.51	8.97E-13
TM18	4	249	106.3	32388	1.76E-13	n.d.	0.33	5.79E-14
TM7	n.d.	n.d.	116.7	39350	1.13E-13	INT	0.67	7.59E-14
TM70	5	238	252.8	81546	1.36E-13	INT	0.49	6.65E-14
TM71	4	271	208.6	107025	3.88E-14	SUP	0.64	2.48E-14

B5.3 – Results of the fracture analysis performed through the virtual scan-area surveys.

Virtual scan-area	Fracture intensity, P21 (m^{-1})	Fracture frequency, P20 (m^{-2})	Mean Tracelength (m)	Maximum permeability, k1 (m^2)	Distance from the main fault (m)	% supratidal	Connectivity, λ	Revised maximum permeability, k1 (m^2)
A1	4.8	23	0.36	1.55E-08	89	96	0.4	6.19E-09
A2	5.3	24	0.35	1.90E-08	86	79	0.4	7.58E-09
A3	3.3	17	0.27	7.94E-09	79	42	0.3	2.38E-09
A4	3.7	16	0.36	1.21E-08	67	28	0.3	3.64E-09
A5	3.8	18	0.33	6.77E-09	78	29	03	2.03E-09
A6	4.9	17	0.49	3.23E-08	71	38	0.4	1.29E-08
A7	6.2	30	0.4	1.72E-08	62	66	0.4	6.87E-09
A8	2.6	10	0.49	1.02E-08	54	55	0.4	4.08E-09
A9	5.9	24	0.35	1.30E-08	37	65	0.4	5.21E-09
A10	3.3	8	0.68	4.49E-08	27	9	0.4	1.80E-08
A11	3.8	16	0.35	1.08E-08	18	22	0.4	4.33E-09
A12	3.1	12	0.39	8.16E-09	11	20	0.4	3.26E-09
B1	7.4	27	0.62	2.76E-08	113	91	0.5	1.38E-08
B2	8.9	34	0.61	4.04E-08	103	61	0.6	2.42E-08
B3	11.3	51	0.62	3.27E-08	108	75	0.6	1.96E-08
B4	12.1	47	0.71	4.48E-08	94	69	0.7	3.14E-08
B5	12.0	53	0.54	4.57E-08	89	73	0.6	2.74E-08
C1	6.7	24	0.65	5.79E-08	110	69	0.6	3.48E-08
C2	10.0	36	0.64	5.19E-08	82	55	0.6	3.12E-08
C3	8.0	27	0.63	4.26E-08	80	43	0.6	2.55E-08

C4	6.4	25	0.59	2.24E-08	79	8	0.5	1.12E-08
C5	6.7	24	0.65	4.10E-08	82	51	0.6	2.46E-08
D1	7.8	39	0.2	1.02E-08	69	69	0.5	5.12E-09
D2	10.3	50	0.2	2.86E-08	63	68	0.6	1.71E-08
D3	12.2	61	0.2	2.07E-08	64	77	0.6	1.24E-08
D4	8.4	36	0.24	2.84E-08	64	36	0.5	1.42E-08
D5	10.6	35	0.31	7.32E-08	83	57	0.5	4.39E-08
E1	8.7	27	0.57	8.72E-08	32	57	0.5	5.23E-08
E2	6.6	19	0.51	7.07E-08	56	40	0.4	3.53E-08
F1	6.3	19	0.58	7.86E-08	15	28	0.5	3.93E-08

References

Bernabé, Y., Mok, U., & **Evans, B.** (2003). Permeability-porosity relationships in rocks subjected to various evolution processes. *Pure and Applied Geophysics*, *160*(5-6), 937-960.

Bisdom, K., Bertotti, G., & **Nick, H. M.** (2016). The impact of in-situ stress and outcrop-based fracture geometry on hydraulic aperture and upscaled permeability in fractured reservoirs. *Tectonophysics*, *690*, 63-75.

Cappa, F., Guglielmi, Y., Fénart, P., Merrien-Soukatchoff, V., & **Thoraval, A.** (2005). Hydromechanical interactions in a fractured carbonate reservoir inferred from hydraulic and mechanical measurements. *International Journal of Rock Mechanics and Mining Sciences*, *42*(2), 287-306.

Healy, D., Rizzo, R. E., Cornwell, D. G., Farrell, N. J., Watkins, H., Timms, N. E., ... & **Smith, M.** (2017). FracPaQ: A MATLAB™ toolbox for the quantification of fracture patterns. *Journal of Structural Geology*, *95*, 1-16.

Medici, G., West, L. J., & **Banwart, S. A.** (2019a). Groundwater flow velocities in a fractured carbonate aquifer-type: Implications for contaminant transport. *Journal of contaminant hydrology*, *222*, 1-16.

Medici, G., West, L. J., Chapman, P. J., & **Banwart, S. A.** (2019b). Prediction of contaminant transport in fractured carbonate aquifer types: a case study of the Permian Magnesian Limestone Group (NE England, UK). *Environmental Science and Pollution Research*, 1-22.

Noushabadi, M. J., Jourde, H., & **Massonnat, G.** (2011). Influence of the observation scale on permeability estimation at local and regional scales through well tests in a fractured and karstic aquifer (Lez aquifer, Southern France). *Journal of Hydrology*, *403*(3-4), 321-336.

Suzuki, K., Oda, M., Yamazaki, M., & **Kuwahara, T.** (1998). Permeability changes in granite with crack growth during immersion in hot water. *International Journal of Rock Mechanics and Mining Sciences*, *35*(7), 907-921.

Vermilye, J. M., & **Scholz, C. H.** (1998). The process zone: A microstructural view of fault growth. *Journal of Geophysical Research: Solid Earth*, *103*(B6), 12223-12237.

Worthington, S. R., & **Ford, D. C.** (1995, June). Borehole tests for megascale channeling in carbonate aquifers. In *Proceedings, XXVI Congress of the International Association of Hydrogeologists, Edmonton, Alberta*.

Ringraziamenti

Desidero ringraziare tutte le persone che mi hanno accompagnato lungo questo percorso e che hanno, ciascuno a suo modo, reso possibile raggiungere questo traguardo.

Innanzitutto, ringrazio Cristiano ed Eugenio. Grazie per la vostra pazienza, per la vostra disponibilità, per i preziosi consigli, per aver tenuto il manubrio durante le sbandate, ma soprattutto per la fiducia che avete avuto in me. Grazie poi per avermi insegnato ad essere intraprendente ed indipendente senza mai farmi mancare il sostegno nei momenti di bisogno. Grazie infine per la serenità e per la simpatia con cui mi avete accompagnato in questi anni.

Ringrazio poi tutte le persone con le quali ho collaborato durante questi tre anni. Grazie a Marco Scuderi, Telemaco, Paolo, Ken, Luca, Alessandro, Maria Chiara e Marco Brandano.

A special thanks to Ken for his guidance, kindness and hospitality during the period I spent in Durham. The time I spent there has been fundamental for my human and scientific growth.

Grazie ai ragazzi di Nhazca per il loro aiuto con gli affioramenti virtuali e per la loro disponibilità. Grazie quindi a Francesco, Angelo, Marco, Stefano e Damiano.

Spesso anche piccoli consigli, aiuti e chiacchierate sono stati fondamentali. Grazie a Carolina ed Irene per avermi aiutato e per aver dispensato preziosissimi consigli all'inizio del percorso. Grazie a Mimmo per la sua gentilezza e disponibilità nell'aiutarmi con rocce e sezioni sottili. Grazie ad Andrea Billi, Marta Della Seta, Fabio Trippetta, Sabina Bigi per preziosi consigli e aiuti.

Grazie all'aula dottorandi e ai suoi inquilini. Grazie per aver reso il tutto più leggero e grazie per le terapie di gruppo di fronte ad uno spritz.

Grazie poi a chi mi ha accompagnato durante il dottorato da spettatore (o vittima, fate voi...). Grazie alla mia famiglia per aver sopportato i miei alti e bassi emotivi in questi anni senza farmelo pesare. Grazie mamma e papà per i sacrifici fatti per potermi permettere di intraprendere questo percorso.

Grazie a Lavinia, che più di ogni altra persona ha sopportato gli sbalzi di umore di cui sopra. Grazie per non aver mai smesso di incoraggiarmi e di risollevarmi nei momenti bui di questo percorso.